

Fast post-process Bayesian inference with Variational Sparse Bayesian Quadrature

Chengkun Li[†], Grégoire Clarté[‡], Martin Jørgensen[†], Luigi Acerbi[†]

[†]Department of Computer Science, University of Helsinki,
 chengkun.li@helsinki.fi, martin.jorgensen@helsinki.fi
 luigi.acerbi@helsinki.fi

[‡] Department of Statistics, University of Edinburgh, gclarte@ed.ac.uk

Abstract

In applied Bayesian inference scenarios, users may have access to a large number of pre-existing model evaluations, for example from maximum-a-posteriori (MAP) optimization runs. However, traditional approximate inference techniques make little to no use of this available information. We propose the framework of *post-process Bayesian inference* as a means to obtain a quick posterior approximation from existing target density evaluations, with no further model calls. Within this framework, we introduce Variational Sparse Bayesian Quadrature (vsbq), a method for post-process approximate inference for models with *black-box* and potentially noisy likelihoods. vsbq reuses existing target density evaluations to build a sparse Gaussian process (GP) surrogate model of the log posterior density function. Subsequently, we leverage sparse-GP Bayesian quadrature combined with variational inference to achieve fast approximate posterior inference over the surrogate. We validate our method on challenging synthetic scenarios and real-world applications from computational neuroscience. The experiments show that vsbq builds high-quality posterior approximations by post-processing existing optimization traces, with no further model evaluations.

Keywords: approximate Bayesian inference, sparse Gaussian processes, Bayesian quadrature, post-process inference

1 Introduction

Bayesian inference is a well-founded approach to uncertainty quantification and model selection, widely adopted in data science and machine learning [Robert et al., 2007, Gelman et al., 2013, Ghahramani, 2015]. Key quantities in Bayesian inference are the *posterior distribution* of model parameters, useful for parameter estimation and uncertainty quantification, and the *marginal likelihood* or model evidence, useful for model selection. In practice, Bayesian inference is particularly challenging when dealing with models with ‘black-box’ features common in science and engineering, such as lack of gradients or mildly-to-very expensive and possibly noisy evaluations of the likelihood, *e.g.*, arising from simulator-based estimation [Wood, 2010, van Opheusden et al., 2020].

Due to the cost of inference, parameter estimation and the workflow of Bayesian analyses often start with a preliminary exploration phase via simpler and cheaper means [Gelman et al., 2020]. A popular choice consists of performing maximum likelihood estimation (MLE) or maximum a

posteriori (MAP) estimation [Gelman et al., 2013, Chapter 13], *i.e.*, finding the (global) *mode* of the posterior density,¹ often via multiple runs of black-box optimization algorithms (e.g., Hansen et al., 2003, Acerbi and Ma, 2017), which can easily require tens of thousands likelihood or posterior density evaluations over distinct optimization runs to satisfactorily explore the parameter landscape (e.g., Acerbi et al., 2018, Norton et al., 2019, Cao et al., 2019, Zhou et al., 2020, Yoo et al., 2021, Heald et al., 2021). In fact, due to prohibitive costs, many analyses stop here, with a point estimate instead of a full posterior, as advocated for example in modeling tutorials and textbooks in applied domains such as computational and cognitive neuroscience [Wilson and Collins, 2019, Ma et al., 2023].

In this paper, we propose the framework of *post-process Bayesian inference* as a solution to the waste of potentially expensive likelihood and posterior density evaluations, with the goal of making ‘black-box’ Bayesian inference cheaper and more widely applicable by modeling practitioners. Namely, we aim to build an approximation of the full Bayesian posterior by recycling *all* previous evaluations of the posterior density achieved by various means. In principle, our proposed method has no restrictions for the source of evaluations, as long as the evaluation points form a representative set of the underlying posterior. In this paper, we focus on re-utilizing evaluations obtained from MAP optimization runs of black-box optimization methods such as CMA-ES [Hansen, 2016] and BADS [Acerbi and Ma, 2017, Singh and Acerbi, 2024]. We chose these methods for their popularity among practitioners, available implementations in multiple programming languages (e.g., MATLAB and Python), as well as their capability of robustly handling both exact and noisy objective functions.

As an instantiation of our framework, we introduce Variational Sparse Bayesian Quadrature (VSBQ). VSBQ builds a Gaussian process (GP; Rasmussen and Williams, 2006) surrogate of the log density, starting from existing log-likelihood or log-density evaluations. In particular, we use a *sparse* GP to deal with a potentially large number of model evaluations [Titsias, 2009] and develop the *noise shaping* technique for efficient posterior modeling. A tractable posterior approximation is then obtained by performing variational inference over the surrogate, thus without further evaluations of the original model. Fitting the flexible variational posterior is particularly efficient by utilizing Bayesian quadrature [O’Hagan, 1991, Acerbi, 2018]. We validate our approach on synthetic targets and real datasets and models from computational neuroscience [Acerbi et al., 2012, 2018]. Overall, we find that post-process Bayesian inference via VSBQ is not only feasible but can yield high-quality approximations, providing the applied modeler with a new approximate inference tool that can easily fit in existing modeling pipelines as a refinement step. At the end of the paper, we discuss the limitations of the method and future work.

Related work. There are several works related to post-processing existing density evaluations to construct an approximate posterior. Zhang et al. [2022] find the best multivariate normal approximation along the optimization paths generated by a quasi-Newton optimization algorithm, L-BFGS [Liu and Nocedal, 1989], in terms of Kullback-Leibler (KL) divergence to the true posterior. Unlike our method, the L-BFGS algorithm requires the gradients of the log-likelihood or log-density function to build approximate estimates of the Hessian along the optimization trajectory and is brittle to noise in the target function. Moreover, the post-process estimation of the KL divergence needs additional evaluations of the log-density function. Yao et al. [2022] propose to reuse parallel – and possibly incomplete – runs of different inference algorithms such as Markov Chain Monte Carlo (MCMC; see e.g. Robert and Casella, 2004) or variational inference [Blei et al., 2017] by combining them in a weighted average via ‘Bayesian stacking’. Similar in spirit to our approach, the computation of the stacking weights only requires a post-processing step. However, Bayesian stacking requires the

¹For a fixed parameterization, MLE can be viewed as MAP estimation with (improper) uniform/flat priors.

samples to be approximately drawn from the posterior and does not make use of all available target evaluations. Finally, a related technique that merits mention is *offline* black-box optimization [Krishnamoorthy et al., 2023, Trabucco et al., 2022]. In offline black-box optimization, the objective is to identify a parameter input that maximizes a black-box function utilizing pre-existing offline function evaluations. Much like our approach, offline black-box optimization capitalizes on leveraging existing evaluations. However, a key distinction lies in our primary objective, which is to construct an approximation of the unknown posterior density, a task inherently more challenging than finding a point estimate.

Outline. We first recap the essential background methods—(sparse) Gaussian processes (GPs), variational inference, and Bayesian quadrature, in Section 2. In Section 3, we describe the details of our proposed framework for post-process inference, Variational Sparse Bayesian Quadrature (vsbq). In the process, we introduce a simple and principled heuristic to make the sparse GP representation focus on regions of interest, *noise shaping* (Section 3.3). Section 4 validates vsbq on challenging synthetic and real-world examples. Finally, Section 5 discusses the strengths and limitations of our approach. Proofs, implementation details, additional results, and extended explanations can be found in the Supplementary Material.

2 Background

In this section, we present the core concepts and techniques used in the paper. We recall that our objective is to compute a tractable approximation of the posterior density, given the evaluations (observations) of the unnormalized log-density function. We provide an overview of key techniques including the variational inference method for posterior approximation, the Gaussian process as a regression surrogate, Bayesian quadrature, Variational Bayesian Monte Carlo [Acerbi, 2018], and sparse Gaussian processes.

Notation. Throughout the paper, we denote with $f_0(\mathbf{x}) \equiv \log p(\mathcal{D}|\mathbf{x})p(\mathbf{x})$ the target (unnormalized) log posterior density or log joint, where $p(\mathcal{D}|\mathbf{x})$ is the likelihood of the model of interest under the data \mathcal{D} , $p(\mathbf{x})$ is the prior, and $\mathbf{x} \in \mathcal{X} \subseteq \mathbb{R}^D$ is a vector of model parameters. The dimension of the parameter space is denoted as $D \in \mathbb{N}$. We indicate with (\mathbf{x}_n, y_n) pairs of observed locations and values of the log-density, *i.e.*, $y_n = f_0(\mathbf{x}_n)$. For noisy evaluations of the target arising from simulator-based estimates, $\sigma_{\text{obs}}^2(\mathbf{x}_n)$ denotes the variance of the observation, assumed to be known (in practice, estimated; for example see Acerbi, 2020). $(\mathbf{X}, \mathbf{y}, \mathbf{s}) \equiv \{\mathbf{x}_n, y_n, \sigma_{\text{obs}}(\mathbf{x}_n)\}_{n=1}^N$ denote the set of observations. We denote with \mathbf{S} the diagonal matrix of observation noise variances, with $\mathbf{S} \equiv \text{diag}[\sigma_{\text{obs}}^2(\mathbf{x}_1), \dots, \sigma_{\text{obs}}^2(\mathbf{x}_N)]$.²

2.1 Variational inference

Variational inference is a popular approach to approximate the intractable posterior density $p(\mathbf{x}|\mathcal{D})$ via a simpler distribution $q(\mathbf{x}) \equiv q_\phi(\mathbf{x})$ that belongs to a parametric family indexed by ϕ [Jordan et al., 1999, Bishop, 2006, Blei et al., 2017]. The goal of variational inference is to find ϕ for which the variational posterior q_ϕ best approximates the true posterior, as quantified by the reverse Kullback-Leibler (KL) divergence,

$$D_{\text{KL}} [q_\phi(\mathbf{x})||p(\mathbf{x}|\mathcal{D})] = \mathbb{E}_\phi \left[\log \frac{q_\phi(\mathbf{x})}{p(\mathbf{x}|\mathcal{D})} \right], \quad (1)$$

²Later, this will be the total observation noise, which includes noise shaping introduced in Section 3.3.

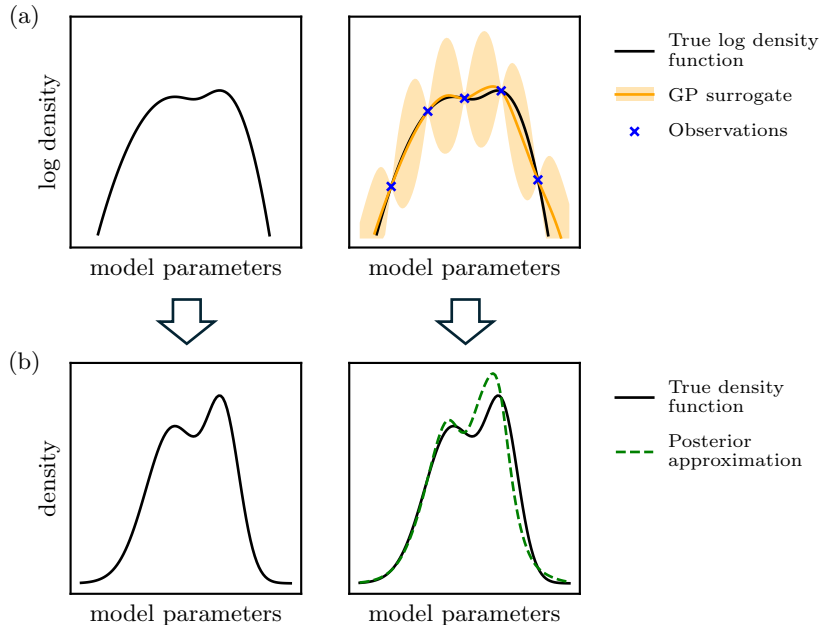


Figure 1: **Log-density function modeling and posterior approximation.** (a) The left panel depicts the ground-truth (unnormalized) posterior log-density function. The right panel illustrates the Gaussian Process (GP) approximation to the log-density function (mean and 95% credible interval), given observed log-density evaluations (blue crosses). (b) The left panel depicts the ground-truth posterior density function, corresponding to the log density in (a). The right panel illustrates the posterior density approximation corresponding to the GP surrogate mean.

where $\mathbb{E}_\phi \equiv \mathbb{E}_{q_\phi}$. Crucially, $D_{\text{KL}}(q||p) \geq 0$ and $D_{\text{KL}}(q||p) = 0$ if and only if $q = p$. Minimizing the KL divergence casts Bayesian inference as an optimization problem. This optimization consists of finding the variational parameters, ϕ , that maximize the objective:

$$\begin{aligned} \text{ELBO}[q_\phi] &= \mathbb{E}_\phi \left[\log \frac{p(\mathcal{D}|\mathbf{x})p(\mathbf{x})}{q_\phi(\mathbf{x})} \right] \\ &= \mathbb{E}_\phi [f_0(\mathbf{x})] + \mathcal{H}[q_\phi(\mathbf{x})], \end{aligned} \quad (2)$$

with $f_0(\mathbf{x}) = \log p(\mathcal{D}|\mathbf{x})p(\mathbf{x}) = \log p(\mathcal{D}, \mathbf{x})$ the log joint density, and $\mathcal{H}[q]$ the entropy of q . Eq. 2 is the *evidence lower bound* (ELBO), a lower bound to the log marginal likelihood $\log p(\mathcal{D})$ (also called model evidence), with equality holding if $q(\mathbf{x}) = p(\mathbf{x}|\mathcal{D})$.

Variational inference with a flexible variational family q_ϕ can approximate the target arbitrarily well [Miller et al., 2017], but at the cost of a large number of evaluations of the target – and its gradient – to optimize the ELBO in Eq. 2. This is particularly problematic if the target likelihood or joint density is a black-box function, such that evaluations may be limited due to computational resources and the gradient unavailable.

2.2 Gaussian processes

When a computational model of interest has an expensive black-box likelihood, a proven approach for efficient Bayesian inference consists of building a (cheaper) *surrogate model* to emulate either the

log-likelihood $\log p(\mathcal{D}|\mathbf{x})$ or directly the log joint density function $f_0(\mathbf{x})$; see Figure 1. There is a long tradition of using Gaussian processes (GPs) as surrogate models for Bayesian inference [Rasmussen, 2003, Gunter et al., 2014, Gutmann and Corander, 2016, Nemeth and Sherlock, 2018, Wang and Li, 2018, Acerbi, 2018, Järvenpää et al., 2021, De Souza et al., 2022, Gammal et al., 2022].

GPs are stochastic processes that can be thought of as distributions over functions. We refer the reader to Rasmussen and Williams [2006], Garnett [2023] for an introduction to GPs in applied machine learning contexts. GPs are determined by a prior mean function $m : \mathcal{X} \rightarrow \mathbb{R}$; a positive definite covariance function $\kappa : \mathcal{X} \times \mathcal{X} \rightarrow \mathbb{R}$ (also called a kernel); and a likelihood or observation model. The mean function represents the average behavior and trend of a GP far from observed data. In the case of log-density modeling, it is both beneficial and necessary to consider specific mean functions other than the usual constant mean function [Acerbi, 2019]. We detail the mean function design in Section 2.4.

Observation model. GPs are characterized by a likelihood or observation noise model, commonly assumed to be Gaussian to afford GP posterior computations in closed form. In this paper, we consider both noiseless and noisy observations of the target log joint. For noiseless targets, we use a Gaussian likelihood with a small variance $\sigma_{\text{obs}}^2 = 10^{-5}$, also known as *nugget*, for numerical stability [Gramacy and Lee, 2012]. Noisy observations of the target often arise from using stochastic estimators of the log-likelihood via simulation [Wood, 2010, van Opheusden et al., 2020].

GP posterior. The GP posterior given function observations $(\mathbf{X}, \mathbf{y}, \mathbf{s})$ is also a Gaussian process with the posterior mean function μ_p and posterior covariance function κ_p [Rasmussen and Williams, 2006]. For $\tilde{\mathbf{x}}, \tilde{\mathbf{x}}' \in \mathcal{X}$,

$$\begin{aligned} \mu_p(\tilde{\mathbf{x}}) &= \kappa(\tilde{\mathbf{x}}, \mathbf{X}) (\kappa(\mathbf{X}, \mathbf{X}) + \mathbf{S})^{-1} (\mathbf{y} - m(\mathbf{X})) \\ &\quad + m(\tilde{\mathbf{x}}), \end{aligned} \tag{3}$$

$$\begin{aligned} \kappa_p(\tilde{\mathbf{x}}, \tilde{\mathbf{x}}') &= \kappa(\tilde{\mathbf{x}}, \tilde{\mathbf{x}}') - \kappa(\tilde{\mathbf{x}}, \mathbf{X}) (\kappa(\mathbf{X}, \mathbf{X}) + \mathbf{S})^{-1} \\ &\quad \times \kappa(\mathbf{X}, \tilde{\mathbf{x}}'). \end{aligned} \tag{4}$$

Tractable surrogate density approximation. A key observation is that a GP surrogate of the log density (Figure 1a) does not immediately yield a usable approximate posterior. The normalization constant is unknown and we cannot directly sample from the density associated with the GP surrogate. Another layer of approximation is needed to go from the log density surrogate to posterior approximation (Figure 1). Several approximation techniques have been developed to tackle this issue, many of them involving Bayesian quadrature [Ghahramani and Rasmussen, 2002b, Osborne et al., 2012, Gunter et al., 2014, Acerbi, 2018, Adachi et al., 2022].

2.3 Bayesian quadrature

Many key computations in Bayesian inference require the estimation of intractable integrals, as for example the ELBO seen in Eq. 2. Bayesian quadrature [O’Hagan, 1991, Ghahramani and Rasmussen, 2002a] is a technique to obtain Bayesian estimates of intractable integrals of the form

$$\mathcal{J} = \int_{\mathcal{X}} f(\mathbf{x})\pi(\mathbf{x})d\mathbf{x}, \tag{5}$$

where f is a function of interest and π a known probability distribution. Here we consider the domain of integration $\mathcal{X} = \mathbb{R}^D$. When a GP prior is specified for f , since integration is a linear

operator, the integral \mathcal{J} is also a Gaussian random variable whose posterior mean and variance are [Ghahramani and Rasmussen, 2002a]

$$\mathbb{E}_f[\mathcal{J}] = \int \mu_p(\mathbf{x})\pi(\mathbf{x})d\mathbf{x}, \quad (6)$$

$$\mathbb{V}_f[\mathcal{J}] = \int \int \kappa_p(\mathbf{x}, \mathbf{x}')\pi(\mathbf{x})\pi(\mathbf{x}')d\mathbf{x}d\mathbf{x}', \quad (7)$$

where μ_p and κ_p are the GP posterior mean and covariance function. Importantly, if f has a Gaussian kernel and π is a Gaussian or mixture of Gaussians (among other functional forms), the integrals in Eqs. 6 and 7 have closed-form solutions.

2.4 Variational Bayesian Monte Carlo

Variational Bayesian Monte Carlo (VBMC; Acerbi, 2018, 2020, Huggins et al., 2023) is a framework that combines variational inference (Section 2.1), Gaussian processes (Section 2.2), and Bayesian quadrature (Section 2.3) with the goal of approximating the posterior density. VBMC employs a Gaussian process as a surrogate to the log-density function and then performs variational inference on the GP surrogate as opposed to using the original expensive target. The surrogate ELBO in variational inference is efficiently estimated via Bayesian quadrature. Moreover, VBMC introduces acquisition functions for actively sampling new evaluations of the log density to iteratively refine the posterior approximation.

Surrogate ELBO. Using the GP model f as the surrogate to the log joint density f_0 , and for a given variational posterior q_ϕ , the posterior mean of the surrogate ELBO (see Eq. 2) can be estimated as

$$\mathbb{E}_f[\text{ELBO}(\phi)] = \mathbb{E}_f[\mathbb{E}_\phi[f]] + \mathcal{H}[q_\phi], \quad (8)$$

where $\mathbb{E}_f[\mathbb{E}_\phi[f]]$ is the posterior mean of the expected log joint under the GP model, and $\mathcal{H}[q_\phi]$ is the entropy of the variational posterior [Acerbi, 2018]. In particular, the expected log joint takes the form

$$\mathbb{E}_\phi[f] = \int q_\phi(\mathbf{x})f(\mathbf{x})d\mathbf{x}. \quad (9)$$

Specific choices of variational family and GP representation afford *closed-form* solutions for the posterior mean and variance of Eq. 9 (and of their gradients) by means of Bayesian quadrature (see Section 2.3). The entropy of q_ϕ and its gradient can be estimated via simple Monte Carlo and the reparameterization trick [Kingma and Welling, 2013, Miller et al., 2017], such that Eq. 8 can be optimized via stochastic gradient ascent [Kingma and Ba, 2014]. In Figure 1b, we depict the variational posterior obtained by maximizing the surrogate ELBO in Eq. 8, based on the GP surrogate of the log-density depicted in Figure 1a.

Variational posterior. VBMC takes the variational posterior family to be a flexible mixture of multivariate Gaussians. When coupled with a Gaussian process with the exponentiated quadratic kernel and a negative quadratic mean function (see Section 3.1 for the detailed form), this choice of variational posterior enables closed-form computation of the expected log joint in Eq. 9 via Bayesian quadrature. Consequently, it affords efficient and robust optimization of the variational objective.³

³Note that the entropy of a Gaussian mixture does not admit a closed form, requiring the surrogate ELBO to be optimized using stochastic gradient descent.

2.5 Sparse Variational Gaussian Processes

A major limitation of the framework described so far is that standard “exact” GPs scale badly to large numbers of training points N , due to the cubic complexity of the matrix inversion used to evaluate the GP posterior or marginal likelihood, when fitting the GP to observations [Rasmussen and Williams, 2006]. Therefore, fast GP surrogate modeling of the log-density function (or the log-likelihood function) is restricted to regimes with $N \approx 10^3$ log-density evaluations. To address the issue of GP scalability, *sparse* GPs have been proposed to reduce the computational burden of exact full GPs [Snelson and Ghahramani, 2005, Titsias, 2009, Hensman et al., 2013]. In this paper, we adopt *sparse variational GP regression* (SGPR; Titsias, 2009).

Sparse Gaussian process regression. In a nutshell, many sparse GP methods can be interpreted as approximating the full GP via a “smaller” GP defined on a set of *inducing points* $\mathbf{Z} \equiv (\mathbf{z}_1, \dots, \mathbf{z}_M)$ with $M \ll N$, and *inducing variables* \mathbf{u} representing the values of the sparse GP at the inducing points \mathbf{Z} [Snelson and Ghahramani, 2005, Titsias, 2009]. The key difference between sparse GP methods is in how the (smaller) sparse GP posterior is constructed to best approximate the full GP posterior.

To start with the construction of a sparse GP, let \mathbf{f} denote the latent function values corresponding to the observations \mathbf{y} . By first assuming that the inducing values \mathbf{u} are the result of the same Gaussian process as \mathbf{f} , we can write their joint distribution as a multivariate Gaussian distribution (for simplicity, here in the *zero-mean* case):

$$p(\mathbf{f}, \mathbf{u}) = \mathcal{N} \left(\cdot \mid \mathbf{0}, \begin{bmatrix} \mathbf{K}_{\mathbf{X},\mathbf{X}} & \mathbf{K}_{\mathbf{X},\mathbf{Z}} \\ \mathbf{K}_{\mathbf{Z},\mathbf{X}} & \mathbf{K}_{\mathbf{Z},\mathbf{Z}} \end{bmatrix} \right), \quad (10)$$

where $\mathbf{K}_{\mathbf{Z},\mathbf{X}}$ and $\mathbf{K}_{\mathbf{X},\mathbf{Z}}$ are the cross-covariance matrices for the GP prior evaluated at the points in \mathbf{X} and \mathbf{Z} .

In turn, we can write the full joint distribution $p(\mathbf{y}, \mathbf{f}, \mathbf{u})$ as [Titsias, 2009, Hensman et al., 2015]:

$$p(\mathbf{y}, \mathbf{f}, \mathbf{u}) = p(\mathbf{y} \mid \mathbf{f})p(\mathbf{f} \mid \mathbf{u})p(\mathbf{u}), \quad (11)$$

and find the best approximate distribution $q(\mathbf{f}, \mathbf{u})$ in the KL-divergence sense for the posterior $p(\mathbf{f}, \mathbf{u} \mid \mathbf{y})$. The form of the approximate distribution $q(\mathbf{f}, \mathbf{u})$ is chosen to be $p(\mathbf{f} \mid \mathbf{u})\tilde{p}(\mathbf{u})$, where $\tilde{p}(\mathbf{u})$ is the variational distribution for inducing variables \mathbf{u} . The target ELBO for the sparse GP can be written as:

$$\text{GP-ELBO} = \mathbb{E}_{q(\mathbf{f})}[\log p(\mathbf{y} \mid \mathbf{f})] - \text{KL}[\tilde{p}(\mathbf{u}) \parallel p(\mathbf{u})], \quad (12)$$

where $q(\mathbf{f}) \equiv \int p(\mathbf{f} \mid \mathbf{u})\tilde{p}(\mathbf{u})d\mathbf{u}$. Note that Eq. 12 is the ELBO of the variational sparse GP approximation to the full GP. We refer to it as GP-ELBO to differentiate it from the ELBO of the variational approximation in Sections 2.1 and 2.4, which is the (surrogate) ELBO of the approximate posterior over model parameters.

For the case of sparse GP regression with Gaussian likelihood, Titsias [2009] proved that the optimal variational distribution that maximizes Eq. 12 for fixed GP hyperparameters and inducing point locations \mathbf{Z} is given by $\tilde{p}(\mathbf{u}) = \mathcal{N}(\mathbf{m}_{\mathbf{u}}, \mathbf{R}_{\mathbf{uu}})$, defined below. Furthermore, equality between the sparse and full GP posterior is obtained for $\mathbf{Z} = \mathbf{X}$. The optimal variational parameters $\mathbf{m}_{\mathbf{u}}, \mathbf{R}_{\mathbf{uu}}$ of the sparse GP are:

$$\mathbf{m}_{\mathbf{u}} = \mathbf{K}_{\mathbf{Z},\mathbf{Z}}\Sigma\mathbf{K}_{\mathbf{Z},\mathbf{X}}\mathbf{S}^{-1}\mathbf{y}, \quad (13)$$

$$\mathbf{R}_{\mathbf{uu}} = \mathbf{K}_{\mathbf{Z},\mathbf{Z}}\Sigma\mathbf{K}_{\mathbf{Z},\mathbf{Z}}, \quad (14)$$

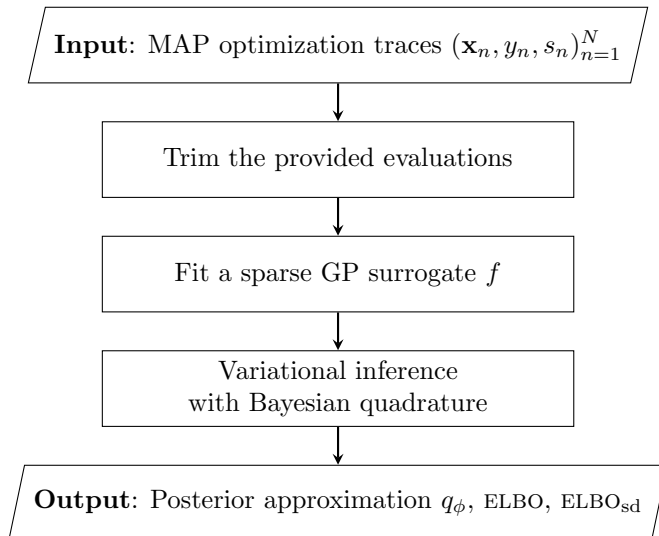


Figure 2: **Overview of VSBQ algorithm.** See text for details.

where $\Sigma \equiv (\mathbf{K}_{\mathbf{z}, \mathbf{x}} \mathbf{S}^{-1} \mathbf{K}_{\mathbf{x}, \mathbf{z}} + \mathbf{K}_{\mathbf{z}, \mathbf{z}})^{-1}$.

Detailed derivations and numerical implementation details are provided in Supplementary Material A.1-A.3.

3 Variational Sparse Bayesian Quadrature

In this section, we present our method for *post-process Bayesian inference*, named Variational Sparse Bayesian Quadrature (VSBQ). As mentioned, statistical analysis in computational modeling studies often relies on *maximum a posteriori* (MAP) estimation,⁴ typically involving multiple runs of a numerical optimization algorithm to identify the MAP estimate from the highest log-density value. Crucially, the evaluation traces from MAP optimization, which hold valuable information about the posterior density, are usually discarded. The *post-process* inference framework we propose aims to reuse these many existing evaluations to efficiently construct a good approximation of the posterior distribution, which is particularly beneficial in scenarios with computationally expensive or noisy model evaluations. Our approach recycles valuable information, effectively converting a point estimate into a posterior approximation with minimal computational expense.

3.1 Overview of the algorithm

Our proposed algorithm consists of three main steps summarized in Figure 2.

- a. We first collect and “trim” the target evaluations $(\mathbf{x}_n, y_n, s_n)_{n=1}^N$ from MAP optimization or other sources.
- b. We fit a sparse GP surrogate to the remaining log-density evaluations.
- c. We perform efficient variational inference over the surrogate via Bayesian quadrature.

⁴Often with a uniform, noninformative prior, effectively reducing to maximum-likelihood estimation.

The output of the procedure is an approximate posterior q_ϕ , the estimated surrogate ELBO (see Section 2.4), and the surrogate ELBO’s standard deviation ELBO_{sd} . We briefly describe each step below and discuss additional details in the following sections.

Trimming of the provided evaluations. We remove from the provided log-density evaluations all points with *extremely* low log-density values relative to the maximum observed value. Such points are at best weakly informative (indication of near-zero density value) for approximating the posterior and at worst induce instabilities in the GP surrogate [Acerbi et al., 2018, Järvenpää et al., 2021, Gammal et al., 2022]. Note that we keep points with low density values, as those are useful for anchoring the GP surrogate [De Souza et al., 2022] – we just remove the *extremely* low ones, as explained below. The remaining points after removal are typically still of the order of many thousands, too many to be handled efficiently by exact GPs. We call this preprocessing step *trimming*.

Trimming works as follows. Consider an evaluation (\mathbf{x}_n, y_n, s_n) , for $n \in [1, N]$, where $s_n \equiv \sigma_{\text{obs}}(\mathbf{x}_n)$ is the estimated standard deviation of the observation noise. For each evaluation, we define the lower/upper confidence bounds of the log-density value as, respectively, $\text{LCB}(\mathbf{x}_n) \equiv y_n - \beta s_n$, $\text{UCB}(\mathbf{x}_n) \equiv y_n + \beta s_n$, where $\beta > 0$ is a confidence interval parameter. We remove from our evaluation set all points \mathbf{x}_n for which

$$\max_{n'}(\text{LCB}(\mathbf{x}_{n'})) - \text{UCB}(\mathbf{x}_n) > \eta_{\text{trim}}. \quad (15)$$

In other words, we trim all points whose difference in underlying log-density value compared to the highest log-density value is larger than a threshold with high probability, accounting for the observation noise. A detailed discussion on how to set β and η_{trim} is provided in Supplementary Material C.1.

Sparse GP fitting. The sparse GP surrogate model uses an exponentiated quadratic kernel,

$$\begin{aligned} \kappa(\mathbf{x}, \mathbf{x}'; \sigma_f^2, \boldsymbol{\ell}) \\ = \sigma_f^2 \exp \left[-\frac{1}{2} (\mathbf{x} - \mathbf{x}')^\top \boldsymbol{\Sigma}_\ell^{-1} (\mathbf{x} - \mathbf{x}') \right], \end{aligned} \quad (16)$$

where σ_f is the output scale, $\boldsymbol{\ell} \equiv (\ell_1, \dots, \ell_D)$ is the vector of input length scales, and $\boldsymbol{\Sigma}_\ell = \text{diag}[\ell_1^2, \dots, \ell_D^2]$. This choice of kernel imposes a smoothness prior on the functions and affords closed-form expressions for Bayesian quadrature (see Section 2.3). As depicted in Figure 1a, a GP with this covariance kernel smoothly interpolates between observations of the log-density function while providing estimates of uncertainty.

The mean function is chosen to be a negative quadratic mean function (Eq. 17) to ensure compatibility with Bayesian quadrature and integrability of the exponentiated surrogate, same as Acerbi [2018],

$$m(\mathbf{x}; m_0, \boldsymbol{\mu}, \boldsymbol{\omega}) = m_0 - \frac{1}{2} \sum_{i=1}^D \frac{(x_i - \mu_i)^2}{\omega_i^2}, \quad (17)$$

where m_0 denotes the maximum, $\boldsymbol{\mu} \equiv (\mu_1, \dots, \mu_D)$ is the location vector, and $\boldsymbol{\omega} \equiv (\omega_1, \dots, \omega_D)$ is a vector of scale parameters. Concretely, since the GP falls back to the prior mean function when far from observed data, a negative quadratic mean function ensures that $\int_{\mathcal{X}} \exp(\mu_p(\mathbf{x})) d\mathbf{x}$ is finite, where μ_p is the posterior mean function of the GP. A negative quadratic mean function can also be interpreted as a prior assumption that the target density is a multivariate normal. However, note

that the GP can model deviations from this assumption and represent multimodal and non-Gaussian distributions as well.

The sparse GP posterior given function observations $(\mathbf{X}, \mathbf{y}, \mathbf{s})$ and inducing point locations \mathbf{Z} is also a Gaussian process with mean and covariance:

$$\mu_{q_\psi}(\tilde{\mathbf{x}}) = \kappa(\tilde{\mathbf{x}}, \mathbf{Z}) \boldsymbol{\Sigma} \mathbf{K}_{\mathbf{Z}, \mathbf{X}} \mathbf{S}^{-1} \mathbf{y}, \quad (18)$$

$$\kappa_{q_\psi}(\tilde{\mathbf{x}}, \tilde{\mathbf{x}}') = \kappa(\tilde{\mathbf{x}}, \tilde{\mathbf{x}}') - \kappa(\tilde{\mathbf{x}}, \mathbf{Z}) (\mathbf{K}_{\mathbf{Z}, \mathbf{Z}}^{-1} - \boldsymbol{\Sigma}) \kappa(\mathbf{Z}, \tilde{\mathbf{x}}'), \quad (19)$$

where $\boldsymbol{\Sigma}$ is defined in Eq. 14.

Fitting a sparse GP to the log-density observations involves two critical components: the selection of inducing points and the sparse GP hyperparameters. Our chosen approach is detailed in Section 3.2.

Variational posterior. As per the VBMC method described in Section 2.4, we take the variational posterior q_ϕ to be a mixture of K multivariate Gaussians,

$$q_\phi(\mathbf{x}) = \sum_{k=1}^K w_k \mathcal{N}(\mathbf{x}; \boldsymbol{\mu}_k, \sigma_k^2 \boldsymbol{\Sigma}_\lambda) \quad (20)$$

where $\boldsymbol{\Sigma}_\lambda \equiv \text{diag}[\lambda^{(1)2}, \dots, \lambda^{(D)2}]$ and $\boldsymbol{\lambda} = (\lambda^{(1)}, \dots, \lambda^{(D)})$ is a vector of parameter scales shared across mixture components; w_k , $\boldsymbol{\mu}_k$, and σ_k are, respectively, the mixture weight, mean, and global scale of the k -th component. This choice of variational posterior is both flexible and conducive to enabling (sparse) Bayesian quadrature in the subsequent steps.

Sparse Bayesian quadrature. Bayesian quadrature is used in VBMC to efficiently optimize the variational objective (ELBO) when fitting the variational posterior q_ϕ using the exact GP surrogate (see Section 2.4). In this work, we are interested in Bayesian quadrature formulae for the *sparse* GP f integrated over a mixture of Gaussians q_ϕ . We call it *sparse Bayesian quadrature*.⁵ For multivariate normal distributions of the form $\mathcal{N}(\cdot; \boldsymbol{\mu}_k, \boldsymbol{\Sigma}_k)$, with $1 \leq k \leq K$, the integrals of interest are Gaussian random variables $\{\mathcal{I}_k\}_{k=1}^K$ that depend on the inducing variables \mathbf{u} and take the form:

$$\mathcal{I}_k[\mathbf{u}] = \int \mathcal{N}(\tilde{\mathbf{x}}; \boldsymbol{\mu}_k, \boldsymbol{\Sigma}_k) f(\tilde{\mathbf{x}} | \mathbf{u}) d\tilde{\mathbf{x}}. \quad (21)$$

Denoting with $\psi(\mathbf{u})$ the optimal variational distribution of \mathbf{u} in SGPR, the posterior mean of each integral is:

$$\begin{aligned} \mathbb{E}[\mathcal{I}_k] &= \int \mathcal{N}(\tilde{\mathbf{x}}; \boldsymbol{\mu}_k, \boldsymbol{\Sigma}_k) f(\tilde{\mathbf{x}} | \mathbf{u}) \psi(\mathbf{u}) d\tilde{\mathbf{x}} d\mathbf{u} \\ &= \int \mathcal{N}(\tilde{\mathbf{x}}; \boldsymbol{\mu}_k, \boldsymbol{\Sigma}_k) \mu_\psi(\tilde{\mathbf{x}}) d\tilde{\mathbf{x}}, \end{aligned} \quad (22)$$

⁵Sparse Bayesian quadrature was introduced in an earlier preprint version of this paper [Li et al., 2023], and more recently by Warren and Ramos [2024] under the name of *low-rank Bayesian quadrature*.

where μ_ψ is the sparse GP posterior mean function as in Eq. 18. Similarly, the posterior covariance between integrals \mathcal{I}_i and \mathcal{I}_j is:

$$\begin{aligned} \text{Cov}(\mathcal{I}_i, \mathcal{I}_j) &= \int \int \mathcal{N}(\tilde{\mathbf{x}}; \mu_i, \Sigma_i) \mathcal{N}(\tilde{\mathbf{x}}'; \mu_j, \Sigma_j) \\ &\quad \times \text{Cov}(f(\tilde{\mathbf{x}}), f(\tilde{\mathbf{x}}')) d\tilde{\mathbf{x}} d\tilde{\mathbf{x}}' \\ &= \int \int \mathcal{N}(\tilde{\mathbf{x}}; \mu_i, \Sigma_i) \mathcal{N}(\tilde{\mathbf{x}}'; \mu_j, \Sigma_j) \\ &\quad \times \kappa_\psi(\tilde{\mathbf{x}}, \tilde{\mathbf{x}}') d\tilde{\mathbf{x}} d\tilde{\mathbf{x}}', \end{aligned} \tag{23}$$

where κ_ψ is the sparse GP posterior covariance function as in Eq. 19. Both the posterior mean and variance of the integral can be obtained in closed form as integrals for the product of Gaussians. Therefore, we can compute the ELBO and its standard deviation ELBO_{sd} efficiently. Thus, once the sparse GP fitting is done, obtaining a tractable posterior approximation is computationally cheap and robust. Derivations are provided in Supplementary Material A.4.

3.2 Inducing points and hyperparameter selection

The selection of hyperparameters $\boldsymbol{\xi}$ for the GP kernel and mean functions, as well as the placement of M inducing points \mathbf{Z} , is critical for the approximation quality of a sparse GP. While in principle we could jointly optimize $\boldsymbol{\xi}$ and \mathbf{Z} , this optimization can be extremely expensive and inefficient and is not recommended by modern practice [Burt et al., 2020]. Therefore, we follow Burt et al. [2020], Maddox et al. [2021] and adaptively select inducing points that minimize an empirical error term, namely the trace of the error of a rank- M Nyström approximation.

Inducing point location. The ELBO in SGPR [Titsias, 2009], extended in this paper to the heteroskedastic case (observation-dependent noise), takes the closed form:

$$\begin{aligned} \text{GP-ELBO}(\mathbf{Z}, \boldsymbol{\xi}) &= \log \mathcal{N}(\mathbf{y}; \mathbf{m}(\mathbf{X}), \mathbf{Q}_{\mathbf{X}, \mathbf{X}} + \mathbf{S}) \\ &\quad - \frac{1}{2} \text{Tr}((\mathbf{K}_{\mathbf{X}, \mathbf{X}} - \mathbf{Q}_{\mathbf{X}, \mathbf{X}}) \mathbf{S}^{-1}), \end{aligned} \tag{24}$$

where $\mathbf{Q}_{\mathbf{X}, \mathbf{X}} \equiv \mathbf{K}_{\mathbf{X}, \mathbf{Z}} \mathbf{K}_{\mathbf{Z}, \mathbf{Z}}^{-1} \mathbf{K}_{\mathbf{Z}, \mathbf{X}}$. Note that the GP-ELBO depends on the location of inducing points \mathbf{Z} and GP hyperparameters $\boldsymbol{\xi}$, and consists of the log probability density function of a multivariate normal term, minus the trace of an error term.

For known GP hyperparameters, Burt et al. [2020] show that sampling from a M -determinantal point process (M -DPP) to select inducing points $\mathbf{Z} \subset \mathbf{X}$ will make the trace error term of the GP-ELBO (Eq. 24) close to its optimal value. Since the DPP approach is intractable, we follow Burt et al. [2020] and Maddox et al. [2021] who recommend instead to sequentially select inducing points that greedily maximize the diagonal of the error term,

$$\mathbf{z}^* = \arg \max_{\mathbf{z}} \text{diag}[(\mathbf{K}_{\mathbf{X}, \mathbf{X}} - \mathbf{Q}_{\mathbf{X}, \mathbf{X}}) \mathbf{S}^{-1}]. \tag{25}$$

In turn, this reduces the trace error in Eq. 24 and aims to maximize the GP-ELBO under the current (fixed) GP hyperparameters. Eq. 25 can be interpreted as weighted *greedy variance selection* [Burt et al., 2020], in that it selects points with maximum prior conditional marginal variance at each point in \mathbf{X} (conditioned on the inducing points selected so far), weighted by the precision (inverse variance) of the observation at that location. Overall, this selection procedure can be achieved with complexity $\mathcal{O}(NM^2)$ by Algorithm 1 in Chen et al. [2018].

GP hyperparameters. The procedure for the selection of inducing points mentioned above requires known GP hyperparameters ξ . In practice, it is often enough to start with a reasonable estimate for ξ and then iterate the process multiple times [Burt et al., 2020]. To obtain an initial estimate for the GP hyperparameters, we fit an exact GP on a small subset of the data, and use the exact GP hyperparameters for initial inducing point selection. The subset is chosen via stratified K -means, where we ensure that the chosen subset is representative of the full set in terms of both location and log-density values. After the above initialization, we iterate sparse GP hyperparameter optimization and inducing points selection using the current sparse GP hyperparameters, until no improvement on the GP-ELBO is found. Similarly to other block-optimization procedures, this process is not guaranteed to find the global optimum of the GP-ELBO, but it often works well in practice [Burt et al., 2020].

3.3 Noise shaping

We recall that while we use a surrogate of the *log density* (Figure 1a), our end goal is to accurately estimate the Bayesian posterior *density* (Figure 1b). This goal can be formalized from a decision-theoretical perspective as minimizing the integrated L^p error between our approximate posterior density and the true posterior;⁶ a formulation which is however generally intractable. In practice, this means that, given a limited-resource surrogate model, we want the surrogate to spend resources to accurately represent high log-density regions and allocate fewer resources to low log-density regions, since the latter areas will map close to zero density regardless of the exact log-density value, with near-zero influence on the reconstruction error of the density.

This scenario is exemplified in our case in Figure 3. Here, the surrogate model is a sparse GP whose main resource is the inducing points and their location, as discussed in Section 2.5. Given a target density (Figure 3a), if we naively use a sparse GP to model the target log density, the inducing points are allocated equally over the region (Figure 3b), yielding an inaccurate approximation of the density (Figure 3c). Our proposed solution consists of *noise shaping* (Figure 3d), a simple motivated heuristic that increases the likelihood noise of lower log-density observations, effectively downweighing the contribution of these points to the sparse GP objective (details below). With noise shaping in place, the sparse GP automatically favors the allocation of inducing points (Eq. 25) to better capture higher-density regions (Figure 3e), yielding a highly accurate representation of the posterior density (Figure 3f).

Noise shaping consists of adding an artificial ‘shaping’ noise term, $\sigma_{\text{shape}}(y)$, to the Gaussian likelihood of each observation in the model, without changing the actual observation y . We assume shaping noise to be Gaussian and independent, such that the total likelihood variance for observation $(\mathbf{x}_n, y_n, \sigma_{\text{obs}}(\mathbf{x}_n))$ becomes:

$$\sigma_{\text{tot}}^2(\mathbf{x}_n, y_n) = \sigma_{\text{obs}}^2(\mathbf{x}_n) + \sigma_{\text{shape}}^2(\Delta y_n), \quad (26)$$

where $\sigma_{\text{obs}}^2(\mathbf{x}_n)$ is the estimated measurement variance at \mathbf{x}_n , and $\Delta y_n \equiv y_{\text{max}} - y_n$, with y_{max} the maximum observed log density.

Note that the added variance depends on y_n , the *observation* at \mathbf{x}_n . We design $\sigma_{\text{shape}}^2(\Delta y)$ to add minimal noise to relatively high-valued observations of the log-density, and increasingly larger noise to lower-density points. Specifically, we define

$$\begin{aligned} \sigma_{\text{shape}}(\Delta y) = & \exp((1 - \rho) \log \sigma_{\text{min}} + \rho \log \sigma_{\text{med}}) \\ & + \mathbf{1}_{\Delta y \geq \theta_\sigma} \lambda_\sigma (\Delta y - \theta_\sigma), \end{aligned} \quad (27)$$

⁶See Järvenpää et al. [2021] for a similar analysis.

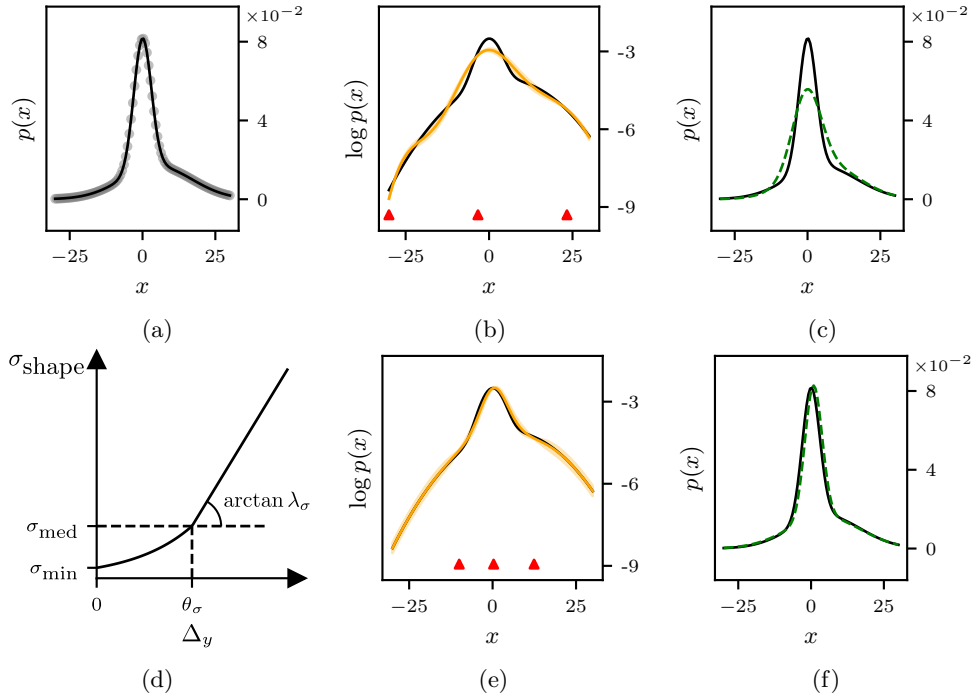


Figure 3: **Illustration of noise shaping effect.** Noise shaping improves the selection of inducing points and the approximation of a sparse GP in the high posterior density region. A better sparse GP consequently leads to an improved variational posterior. The red triangles are locations of inducing points selected via Eq. 25. The orange line represents the sparse GP prediction. The green dashed line represents the variational posterior. (a) True density function (black line) and the observations (black circles). (b) Sparse GP approximation to the log-density function *without* noise shaping. The black curve is the ground truth log-density function. (c) Variational posterior *without* noise shaping. (d) Noise shaping curve corresponding to Eq. 27. (e) Sparse GP approximation *with* noise shaping. (f) Variational posterior *with* noise shaping.

where $\rho = \min(1, \Delta y / \theta_\sigma)$; θ_σ is a threshold for ‘very low density’ points, at which we start the linear increase; λ_σ is the slope of the increase; and σ_{\min}^2 and σ_{med}^2 are two shape parameters. σ_{med} is the added noise at the low density threshold θ_σ . Noise shaping is designed to be small for $\Delta y < \theta_\sigma$ (below σ_{med}^2) and only then it starts taking substantial values. Figure 3d shows an example of how the added shaping noise σ_{shape} increases with Δy . The design principles for noise shaping and specific values of these parameters are provided in Supplementary Material C.1.

As a further motivation for noise shaping, we show that noise shaping is mathematically equivalent to downweighing observations in the sparse GP objective of SGPR. With noise shaping, the GP observation likelihood $p(\mathbf{y} | \mathbf{f})$ becomes $\tilde{p}(\mathbf{y} | \mathbf{f})$, with

$$\begin{aligned} \log \tilde{p}(\mathbf{y} | \mathbf{f}) &= \sum_{n=1}^N \log \tilde{p}(y_n | f_n) \\ &= C - \sum_{n=1}^N \frac{(y_n - f(\mathbf{x}_n))^2}{2\sigma_{\text{tot}}^2(\mathbf{x}_n, y_n)}, \end{aligned} \quad (28)$$

where $C = -\sum_n \log \sqrt{2\pi\sigma_{\text{tot}}^2(\mathbf{x}_n, y_n)}$ is a constant that does not depend on the GP \mathbf{f} . According to Hensman et al. [2015], the expected log-likelihood part of the sparse GP objective (Eq. 12) can be equivalently written as a sum over individual data points,

$$\mathbb{E}_{q(\mathbf{f})}[\log \tilde{p}(\mathbf{y} | \mathbf{f})] = \sum_{n=1}^N \mathbb{E}_{q(f_n)}[\log \tilde{p}(y_n | f_n)], \quad (29)$$

where $q(\mathbf{f})$ is the variational GP posterior. Thus, with noise shaping the expected log-likelihood term of the GP-ELBO becomes,

$$\begin{aligned} & \mathbb{E}_{q(\mathbf{f})}[\log \tilde{p}(\mathbf{y} | \mathbf{f})] \\ &= \text{const} + \sum_{n=1}^N w_n \mathbb{E}_{q(f_n)}[\log p(y_n | f_n)], \end{aligned} \quad (30)$$

where $w_n \equiv \frac{\sigma_{\text{obs}}^2(\mathbf{x}_n)}{\sigma_{\text{tot}}^2(\mathbf{x}_n, y_n)} \leq 1$. That is, by assigning larger ‘shaping’ noise to low-density observations we are downweighing their role in the sparse GP representation, guiding the sparse GP to better represent higher-density regions. Noise shaping also helps during inducing point selection (Eq. 25), as shown in Figure 3.

3.4 Approximation error

In this paper, we use a sparse GP as a surrogate model for the log-density function, which significantly reduces the complexity of the algorithm and makes it possible to post-process a large number of evaluations. At the same time, a sparse GP introduces new approximation errors compared to an exact GP. The approximation error in representing the log-density function via the sparse GP surrogate further leads to errors in the variational posterior. In this section, we present a theoretical result that bounds the (additional) approximation error induced by using a sparse GP in vSBQ.

We introduce Lemma 3.1 and 3.2 first, whose proofs are provided in Supplementary Material B. Recall that \mathbf{f} denotes the latent function values corresponding to the observations \mathbf{y} , \mathbf{u} represents values at the inducing points \mathbf{Z} , and $\boldsymbol{\psi}$ denotes the optimal variational parameters of the sparse GP. Denote with f and f_e the posterior predictive functions of the sparse GP and exact GP, respectively. The posterior mean functions of the sparse GP and exact GP are represented as \bar{f} and \bar{f}_e . Finally, $\|\cdot\|_{TV}$ denotes the total variation distance.

Lemma 3.1. *Assume that $D_{KL}(p(\mathbf{f}, \mathbf{u} | \mathbf{y}) \| p(\mathbf{f}, \mathbf{u} | \boldsymbol{\psi})) \leq \gamma$. Then, for any $\ell > 0$ there exists K_ℓ such that, for any \mathbf{x}^* , $\|\mathbb{E}[f(\mathbf{x}^*)^\ell] - \mathbb{E}[f_e(\mathbf{x}^*)^\ell]\| < K_\ell \sqrt{\gamma/2}$. There also exists K_e such that, for any \mathbf{x}^* , $\|\mathbb{E}[\exp(f(\mathbf{x}^*))] - \mathbb{E}[\exp(f_e(\mathbf{x}^*))]\| < K_e \sqrt{\gamma/2}$.*

Lemma 3.2. *Let a and b be two functions associated with two distributions defined on \mathcal{X} , $\pi_a \propto \exp(a(\cdot))$ and $\pi_b \propto \exp(b(\cdot))$. If $\forall x, |a(x) - b(x)| < K$, then:*

$$\|\pi_a - \pi_b\|_{TV} \leq 1 - \exp(-K). \quad (31)$$

Given the two lemmas above, we can now state a theorem that bounds the distance between the variational posterior q_ϕ constructed from the sparse GP and the variational posterior q_{ϕ_e} from the exact GP.

Theorem 3.3. *Let f and f_e be the sparse GP and exact GP approximation of the target log-density function f_0 , respectively. Let q_ϕ and q_{ϕ_e} be the variational posteriors obtained from the exact GP and*

sparse GP. Let π be the normalized posterior density associated with $\exp(\bar{f})$ (resp., π_e and $\exp(\bar{f}_e)$). Assume that $D_{KL}(q_\phi\|\pi) < \gamma_1$ and $D_{KL}(q_{\phi_e}\|\pi_e) < \gamma_2$, then there exist constants K_l and γ , such that:

$$\begin{aligned} \|q_\phi - q_{\phi_e}\|_{TV} &< \sqrt{\gamma_1/2} + \sqrt{\gamma_2/2} \\ &+ (1 - \exp(-K_l\sqrt{\gamma/2})). \end{aligned} \quad (32)$$

Proof. By the triangle inequality, with π and π_e the distributions associated with \bar{f} and \bar{f}_e : $\|q_\phi - q_{\phi_e}\|_{TV} \leq \|q_\phi - \pi\|_{TV} + \|\pi_e - q_{\phi_e}\|_{TV} + \|\pi_e - \pi\|_{TV}$. The first two terms are bounded by the assumptions and Pinsker’s inequality, the last one by Lemma 3.1 and 3.2. \square

4 Experiments

We empirically investigate the performance of VSBQ with both synthetic and real-world benchmark problems. Each problem is represented by a target posterior density assumed to be a *black box*: gradients are unavailable and evaluations of the log-density function may be (mildly) expensive and noisy. We measured the quality of the posterior approximation by comparing (1) the variational posterior with the ground-truth posterior and (2) the estimated log normalizing constant (via the ELBO) with the ground-truth log marginal likelihood. The ground-truth posterior is represented by samples from well-tuned and extensive MCMC sampling [Foreman-Mackey et al., 2013] or rejection sampling for the 2D synthetic problem.

4.1 Baseline methods

We recall that with black-box inference we mean that the target lacks gradients and may be expensive to evaluate and possibly noisy. As few other methods afford post-process and black-box inference of the posterior, we compare VSBQ again three baselines: black-box variational inference (BBVI), neural network regression (NNR) and the popular Laplace approximation (LAPLACE). Of these, only NNR is also a post-process method. Further implementation details of VSBQ are provided in Supplementary Material C.1.

Black-box variational inference. When the target posterior density is a black-box, the reparametrization trick [Kingma and Welling, 2013] cannot be applied to estimate the ELBO gradient for stochastic variational inference. Instead, one needs to resort to other techniques for computing the gradient of the ELBO, such as the score function estimator, also known as the REINFORCE estimator [Ranganath et al., 2014], which often has higher variance compared to the reparametrization trick [Gal, 2016, Xu et al., 2019]. Specifically, by differentiating Eq. 2, the ELBO gradient $\nabla_\phi \text{ELBO}[q_\phi]$ can be written as,

$$\begin{aligned} \nabla_\phi \mathbb{E}_\phi \left[\log \frac{p(\mathcal{D}|\mathbf{x})p(\mathbf{x})}{q_\phi(\mathbf{x})} \right] \\ = \mathbb{E}_\phi [\nabla_\phi \log q_\phi(\mathbf{x}) (\log p(\mathcal{D}|\mathbf{x})p(\mathbf{x}) - \log q_\phi(\mathbf{x}))]. \end{aligned} \quad (33)$$

In addition, we leverage the control variates technique to reduce the gradient variance (see the supplement for details). We experiment with the following variational distributions for BBVI: a Gaussian with *diagonal* covariance matrix, a Gaussian with *full-rank* covariance matrix, and a mixture of Gaussians with $K = 5$ and $K = 50$ components, respectively, where the mixture of Gaussians (MoG) admits the same form as the variational posterior in VSBQ. The Adam optimizer [Kingma

and Ba, 2014] is used for optimizing the ELBO with stochastic gradients. For each variational distribution choice, we applied grid search on the learning rate hyperparameter in $\{0.01, 0.001\}$ and the number of Monte Carlo samples for gradient estimation in $\{1, 10, 100\}$ and reported the best result, according to the estimated ELBO value. Since BBVI typically requires a large number of target density evaluations for convergence, in all the experiments we assign *ten times more* evaluation budget to BBVI than VSBQ to make it a stronger baseline for reference. Moreover, note that this is not a post-process method, but we include it as a reasonable performance reference. For more details, see Supplementary Material C.3.

Neural network regression. For a direct comparison with our method, we develop a post-process inference algorithm based on a deep neural network regression surrogate (NNR) instead of a sparse GP surrogate, otherwise leaving the post-process procedure (Figure 2) as much as possible the same. This is a competitive baseline since deep neural networks exhibit strong regression performance in the presence of a large number of data points [Goodfellow et al., 2016]. For the network architecture, we use a multilayer perceptron (MLP) with an input layer of dimension D , four hidden layers of 1024 units, and an output layer for predicting the log-density value. The activation function is chosen to be the rectified linear units (ReLU; Goodfellow et al., 2016, Chapter 6). In addition, we add a negative quadratic mean function to the neural network output to ensure that it represents a valid log-density surrogate function.⁷ The negative quadratic mean function is the same as the one used for the (sparse) GP (see Eq. 17). In total, the surrogate function g is:

$$g(\mathbf{x}; \mathbf{w}) = m_0 - \frac{1}{2} \sum_{i=1}^D \frac{(x_i - \mu_i)^2}{\omega_i^2} + \text{MLP}(\mathbf{x}), \quad (34)$$

where \mathbf{w} denotes the neural network parameters (weights and biases), including additional surrogate model parameters (*i.e.*, for the quadratic mean).

We adopt the observation noise model delineated in Section 3.3, yielding the loss:

$$\mathcal{L}(\mathbf{w}) = \sum_{n=1}^N \frac{(g(\mathbf{x}_n) - y_n)^2}{\sigma_{\text{tot}}^2(\mathbf{x}_n, y_n)}, \quad (35)$$

where $\sigma_{\text{tot}}^2(\mathbf{x}_n, y_n) = \sigma_{\text{obs}}^2(\mathbf{x}_n) + \sigma_{\text{shape}}^2(\Delta y_n)$, as per noise shaping.⁸ We optimize the neural network parameters by minimizing the objective in Eq. 35 with the AdamW optimizer [Loshchilov and Hutter, 2019]. For regularization, we considered the ‘weight decay’ hyperparameter $\alpha \in \{0, 0.01, 0.1\}$, selecting the best neural network surrogate based on the loss on a split validation dataset. Finally, we use stochastic variational inference with the reparametrization trick [Kingma and Welling, 2013] to compute the approximate posterior. This part is the same as VSBQ except that the expected log joint of the surrogate in Eq. 2 is approximated via Monte Carlo samples rather than calculated exactly via sparse Bayesian quadrature. For more details, see Supplementary Material C.4.

Laplace approximation. The Laplace approximation method (LAPLACE) computes a multivariate normal approximation of the posterior centered at the MAP location in the unbounded parameter space (see ‘Inference space’ in Section 4.2 below), providing both a posterior approximation and

⁷An MLP with ReLU activations is a *continuous piecewise affine* function [Mukherjee et al., 2018], and therefore adding a trainable negative quadratic mean function ensures the integrability of the exponentiated surrogate.

⁸We found that noise shaping empirically helped stabilize the neural network training.

an estimate of the marginal likelihood [MacKay, 2003]. Despite its simplicity, the Laplace approximation is often used in practice for its efficiency and can yield reasonable posterior approximations [Piray et al., 2019, Daxberger et al., 2021]. Note that LAPLACE requires additional log-density evaluations for numerically estimating the Hessian and is not easily applicable to noisy evaluations, so this is not a fully post-process inference method, but we also include it as a popular baseline and performance reference.

4.2 Procedure and metrics

In this section, we describe the procedure and metrics for the experiments.

MAP estimation. It is worth noting that the MAP estimate (the mode of the posterior density) is not parameterization invariant. To closely align with real-world scenarios, we find the MAP estimate in the space in which the target model parameters are originally defined, as this is the approach practitioners would typically use. If the parameter space is bounded, we let the optimization algorithm handle the bound constraints. For each problem, we allocate a total budget of $3000D$ target evaluations across multiple MAP optimization runs, where D is the dimension of the problem. In the main text, we report results obtained using the CMA-ES optimization algorithm for MAP estimation. Covariance matrix adaptation evolution strategy (CMA-ES) is a stochastic, derivative-free evolutionary algorithm for continuous optimization, widely adopted and very effective in black-box and potentially noisy objective settings [Hansen, 2016]. Further analysis with another black-box optimization algorithm, based on a hybrid Bayesian optimization technique (BADS; Acerbi and Ma, 2017, Singh and Acerbi, 2024), is provided in Supplementary Material C.5.

Inference space. VSBQ, NNR, LAPLACE and BBVI all operate in an *unbounded* parameter space also known as *inference space*. The unbounded inference space is necessary to define and manipulate the multivariate normals (and mixtures thereof) used by all our algorithms. Parameters that are originally subject to bound constraints are mapped to the inference space via a shifted and rescaled probit transform, with an appropriate Jacobian correction to the log-density values. A similar approach is common in probabilistic inference software [Carpenter et al., 2017, Acerbi, 2018]. The approximate posteriors are transformed back to the original space via the corresponding inverse transform, for computing the metrics against the ground truth posterior.

Procedure. The optimization trace points and corresponding log-density values are collected as the training dataset for VSBQ and NNR. For each problem, we repeated the entire optimization procedure – each with *multiple* MAP estimation runs, as explained above – ten times with different random seeds. This yielded ten different training sets per problem, used to assess the robustness and reliability of the methods. The number of inducing points for the sparse GP is set to $100D$. For BBVI, as mentioned in Section 4.1, a budget of $10 \times 3000D = 30000D$ target density evaluations per random seed is allocated for stochastic optimization. In the case of a noisy target, we further vary the observation noise level to study the noise sensitivity of the methods. For the Laplace approximation, we first find the MAP point by transforming the parameter space to unbounded if needed, via a nonlinear mapping.⁹ We subsequently compute the Hessian matrix via adaptive numerical differentiation [Brodtkorb and D’Errico, 2022]. Finally, we compute the performance metrics as detailed below.

⁹For the Laplace approximation to be valid, it is necessary to find the MAP estimate in the unbounded space subsequently used to compute the multivariate normal approximation; this is particularly important if the mode is close to the bounds.

Metrics. We use multiple metrics for assessing the quality of different aspects of the posterior approximation: the absolute difference between the true and estimated log marginal likelihood (ΔLML), the mean marginal total variation distance (MMTV), and the ‘‘Gaussianized’’ symmetrized KL divergence (GsKL) between the approximate and the true posterior [Acerbi, 2020]. For all metrics, lower is better. We describe the three metrics below:

- ΔLML is the absolute difference between true and estimated log marginal likelihood. The true log marginal likelihood is computed analytically, via numerical quadrature methods, or estimated from extensive MCMC sampling via Geyer’s reverse logistic regression [Geyer, 1994], depending on the structure of each specific problem. Differences in log model evidence $\ll 1$ are considered negligible for model selection [Burnham and Anderson, 2003], and therefore for practical usability of a method we aim for an LML loss < 1 .
- The MMTV quantifies the (lack of) overlap between true and approximate posterior marginals, defined as

$$\text{MMTV}(p, q) = \sum_{d=1}^D \int_{-\infty}^{\infty} \frac{|p_d^M(x_d) - q_d^M(x_d)|}{2D} dx_d, \quad (36)$$

where p_d^M and q_d^M denote the marginal densities of p and q along the d -th dimension. Eq. 36 has a direct interpretation in that, for example, an MMTV metric of 0.5 implies that the posterior marginals overlap by 50% (on average across dimensions). As a rule of thumb, we consider a threshold for a reasonable posterior approximation to be $\text{MMTV} < 0.2$, which is more than 80% overlap.

- The GsKL metric is sensitive to differences in means and covariances, being defined as

$$\text{GsKL}(p, q) = \frac{D_{\text{KL}}(\mathcal{N}[p]||\mathcal{N}[q])}{2D} + \frac{D_{\text{KL}}(\mathcal{N}[q]||\mathcal{N}[p])}{2D}, \quad (37)$$

where $D_{\text{KL}}(p||q)$ is the Kullback-Leibler divergence between distributions p and q and $\mathcal{N}[p]$ is a multivariate normal distribution with mean equal to the mean of p and covariance matrix equal to the covariance of p (and same for q). Eq. 37 can be expressed in closed form in terms of the means and covariance matrices of p and q . For reference, two Gaussians with unit variance and whose means differ by $\sqrt{2}$ (resp., $\frac{1}{2}$) have a GsKL of 1 (resp., $\frac{1}{8}$). As a rule of thumb, we consider a desirable target to have GsKL less than $\frac{1}{8}$.

For each metric, we report the median and bootstrapped 95% confidence interval (CI) of the median over the ten different training datasets and random seeds. Further details for performance evaluation can be found in Supplementary Material C.2.

4.3 Synthetic problems

We begin our analysis with two synthetic problems with known log-density functions.

Two Moons bimodal posterior. To evaluate how our method deals with multimodality, we first consider a synthetic bimodal posterior consisting of two ‘moons’ with different weights in $D = 2$.

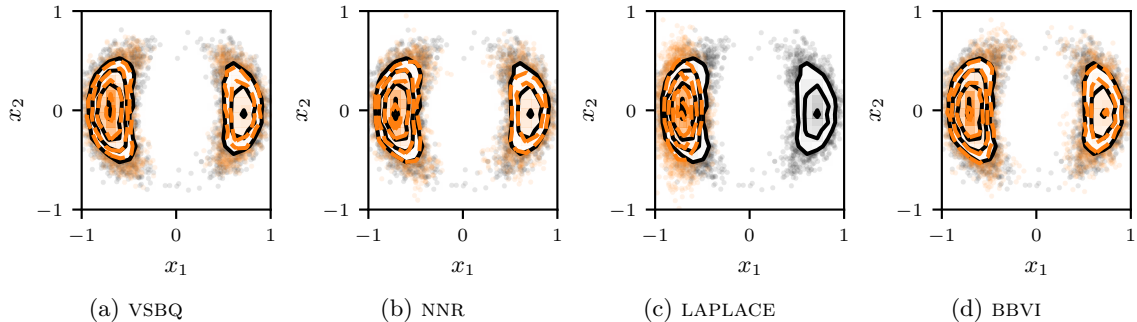


Figure 4: **Two Moons**. The black density contours and points denote ground truth samples. The orange density contours and points represent the posterior samples from (a) VSBQ; (b) NNR; (c) LAPLACE; (d) BBVI with MoG ($K = 50$). VSBQ, NNR and BBVI with MoG ($K = 50$) perfectly recover the bimodal density.

Table 1: **Two Moons posterior** ($D = 2$). The method performance is measured using the metrics ΔLML , MMTV , and GsKL . For all metrics, lower values indicate better performance. We bold the best results based on the 95% confidence interval (CI) of the median. If there are overlaps between CIs, we bold all overlapping values. Note that LAPLACE is deterministic, hence its CI has zero length and is not displayed.

	ΔLML (\downarrow)	MMTV (\downarrow)	GsKL (\downarrow)
Gaussian (diagonal)	0.56 [0.50,1.2]	0.22 [0.21,0.37]	7.6 [6.6,15.]
Gaussian (full-rank)	1.1 [0.57,1.2]	0.36 [0.21,0.37]	14. [7.3,16.]
MoG ($K = 5$)	0.44 [0.28,0.79]	0.21 [0.13,0.28]	5.7 [0.16,8.7]
MoG ($K = 50$)	0.0061 [0.0021,0.015]	0.022 [0.018,0.031]	0.00033 [0.00012,0.00088]
LAPLACE	0.43	0.19	8.1
NNR	0.0085 [0.0038,0.015]	0.021 [0.020,0.023]	0.00033 [0.00016,0.00050]
VSBQ	0.0017 [0.00057,0.0026]	0.020 [0.018,0.021]	8.5e-05 [$4.4e-05$,0.00019]

The bimodal posterior admits an analytic log-density function:

$$p(\mathbf{x}) = \log(\exp(\kappa x_1/r)/3 + 2 \exp(-\kappa x_1/r)/3) - \frac{1}{2} \left(\frac{r - 1/\sqrt{2}}{0.1} \right)^2, \quad (38)$$

where $r = \|\mathbf{x}\|_2$ with $\mathbf{x} = (x_1, x_2)$, $\kappa = 8$. The posterior corresponds to an angle following a von Mises distribution and a normal radius in the polar coordinate system. This density is not defined for $\mathbf{x} = 0$, but remains defined for almost all \mathbf{x} with respect to the Lebesgue measure.

As shown in Figure 4 and Table 1, VSBQ, NNR and BBVI with MoG($K = 50$) reconstruct the bimodal target almost perfectly. By contrast, the Laplace approximation can only cope with unimodal posteriors and thus unsurprisingly fails in this case, despite its otherwise relative simplicity. BBVI with a diagonal Gaussian, a full-rank Gaussian, and a MoG($K = 5$) also reveal inferior performance compared to the other methods.

Table 2: **Multivariate Rosenbrock-Gaussian** ($D = 6$). See Table 1 for a detailed description of metrics and bolding criteria.

	ΔLML (\downarrow)	MMTV (\downarrow)	GsKL (\downarrow)
Gaussian (diagonal)	1.2 [1.1,1.3]	0.23 [0.23,0.23]	0.55 [0.54,0.57]
Gaussian (full-rank)	1.1e+03 [3.8e+02,2.2e+03]	0.66 [0.64,0.75]	3.2e+05 [1.6e+04,1.4e+06]
MoG ($K = 5$)	0.91 [0.83,0.98]	0.16 [0.16,0.17]	0.32 [0.29,0.35]
MoG ($K = 50$)	0.30 [0.21,0.36]	0.058 [0.057,0.060]	0.049 [0.046,0.051]
LAPLACE	1.3	0.24	0.91
NNR	0.20 [0.12,0.28]	0.062 [0.054,0.073]	0.047 [0.037,0.066]
VSQB	0.20 [0.20,0.20]	0.037 [0.035,0.038]	0.018 [0.017,0.018]

Multivariate Rosenbrock-Gaussian. We now experiment with a complex synthetic target of known shape to demonstrate the flexibility of our algorithm. Here we consider a target likelihood in $D = 6$ which consists of the direct product of two exponentiated Rosenbrock (‘banana’) functions $\mathcal{R}(x, y)$ and a two-dimensional normal density. We apply a Gaussian prior to all dimensions. The target density is thus:

$$p(\mathbf{x}) \propto e^{\mathcal{R}(x_1, x_2)} e^{\mathcal{R}(x_3, x_4)} \mathcal{N}([x_5, x_6]; \mathbf{0}, \mathbb{I}) \cdot \mathcal{N}(\mathbf{x}; \mathbf{0}, 3^2 \mathbb{I}), \quad (39)$$

where $\mathcal{R}(x_1, x_2) = -(x_1^2 - x_2)^2 - \frac{(x_2 - 1)^2}{100}$.

As shown in Table 2, both VSQB and NNR approximate this complex posterior well, with VSQB performing slightly better than NNR in terms of metrics. LAPLACE does not give a satisfactory approximation either, due to the heavily non-Gaussian nature of the underlying posterior. Among the BBVI methods, BBVI with MoG ($K = 50$) achieves the best results. However, it still underperforms compared to VSQB, even when allocated a tenfold higher density evaluation budget. The poor metrics further indicate challenges in fitting a full-rank Gaussian using BBVI. A visualization of the approximate posteriors and the ground-truth posterior is provided in Supplementary Material C.6.

4.4 Real-world models

In this section, we perform experiments on two real-world problems from computational neuroscience, focusing on both noiseless and noisy likelihood evaluations.

Noisy likelihood evaluations. In many computational models, the likelihood may not be available in closed form, but an estimate of the (log) likelihood may still be obtained via stochastic estimators, yielding a ‘noisy’ likelihood – or log-likelihood – evaluation [Wood, 2010, van Opheusden et al., 2020]. These estimators work by drawing multiple synthetic data samples from the model, and the number of samples or ‘repetitions’ amounts to a hyperparameter governing the precision of the estimate, which trades off with computational complexity [van Opheusden et al., 2020]. Moreover, these estimates are often approximately normally distributed and approximately – or exactly – unbiased [van Opheusden et al., 2020, Järvenpää et al., 2021]. VSQB is particularly useful when dealing with noisy log-likelihood evaluations, since the sparse GP can effectively compress a large number of noisy evaluations into a more precise estimate. Notably, many common alternative inference methods are unable to handle noisy evaluations.

In this section, we study the performance and robustness of post-process inference methods (VSBQ and NNR) by varying the noise in the log-likelihood evaluations (or observations) in two benchmark problems. A noise standard deviation $\sigma_{\text{obs}} = 0$ corresponds to noiseless target evaluations, obtained through a closed-form or numerical solution of the likelihood. A standard deviation σ_{obs} from 1 to 7 amounts to mild-to-substantial estimation noise in log-likelihood space [Acerbi, 2020], corresponding to cheaper estimates (fewer model samples). Note that LAPLACE only supports noiseless log-density evaluations ($\sigma_{\text{obs}} = 0$), and its results are reported for reference.

Bayesian timing model. We consider a popular Bayesian observer model of time perception from cognitive neuroscience [Jazayeri and Shadlen, 2010, Acerbi et al., 2012, Acerbi, 2020]. The key premise of Bayesian observer modeling in perception is that the participant of a psychophysical experiment – the participant being the system being modeled – is herself performing Bayesian inference over the sensory stimuli, and employs Bayesian decision theory to report their perception [Pouget et al., 2013, Ma et al., 2023].

In this specific sensorimotor timing experiment, in each trial human participants had to reproduce the time interval τ between a mouse click and a screen flash, with $\tau \sim \text{Uniform}[0.6, 0.975]$ s [Acerbi et al., 2012]. We assume participants had only access to a noisy sensory measurement $t_s \sim \mathcal{N}(\tau, w_s^2 \tau^2)$, and their reproduced time t_m was affected by motor noise, $t_m \sim \mathcal{N}(\tau_*, w_m^2 \tau_*^2)$, where w_s and w_m are *Weber’s fractions*, a psychophysical measure of perceptual and motor variability. We assume participants estimated τ_* by combining their sensory likelihood with an approximate Gaussian prior over time intervals, $\mathcal{N}(\tau; \mu_p, \sigma_p^2)$, and took the mean of the resulting Bayesian posterior. For each trial we also consider a probability λ of a ‘lapse’ (*e.g.*, a misclick) producing a response $t_m \sim \text{Uniform}[0, 2]$ s. Model parameters are $\theta = (w_s, w_m, \mu_p, \sigma_p, \lambda)$, so $D = 5$. We infer the posterior of a representative participant using published data from Acerbi et al. [2012].

As shown in Figure 5, VSBQ consistently gives a good posterior approximation across different levels of log-likelihood evaluation noise. In this case, even with a large noise $\sigma_{\text{obs}} = 7$, VSBQ surpasses the performance of LAPLACE. Note that LAPLACE is computed based on *noiseless* target evaluations since it does not support noisy evaluations. In this problem, NNR is considerably less robust, with several failed runs, and performs generally worse compared to VSBQ. Since the target posterior is close to a Gaussian, the BBVI methods exhibit similar performance to each other (as well as across noise levels), all fairly unsatisfactorily hovering above the desired metric thresholds. The insensitivity of BBVI performance to log-likelihood noise suggests that the variance of the score function estimator is the dominating factor behind the suboptimal results. BBVI with a Gaussian with full-rank covariance is excluded from the figure, as it yields poor results due to fitting challenges.

Plots of approximate posteriors and the ground-truth posteriors are visualized in Supplementary Material C.6.

Multisensory causal inference. Perceptual causal inference – inferring whether two sensory cues have the same common source – comprises a variety of models and tasks of major interest in computational and cognitive neuroscience [Körding et al., 2007, Cao et al., 2019, Shams and Beierholm, 2022]. Here we consider a visuo-vestibular causal inference experiment representative of this class of models [Acerbi et al., 2018, Acerbi, 2020]. In this experiment, participants were seated in a moving chair and asked to determine whether the direction of their movement (s_{vest}) corresponded to the direction of a looming visual field (s_{vis}) on a trial by trial basis. It is assumed that the participants can only access noisy sensory measurements, denoted as $z_{\text{vest}} \sim \mathcal{N}(s_{\text{vest}}, \sigma_{\text{vest}}^2)$ for vestibular information and $z_{\text{vis}} \sim \mathcal{N}(s_{\text{vis}}, \sigma_{\text{vis}}^2(c))$ for visual information. Here, σ_{vest} represents the vestibular noise, while $\sigma_{\text{vis}}(c)$ represents the visual noise, with c being one of three distinct levels of visual coherence ($c_{\text{low}}, c_{\text{med}}, c_{\text{high}}$) used in the experiment. To model the participants’ responses,

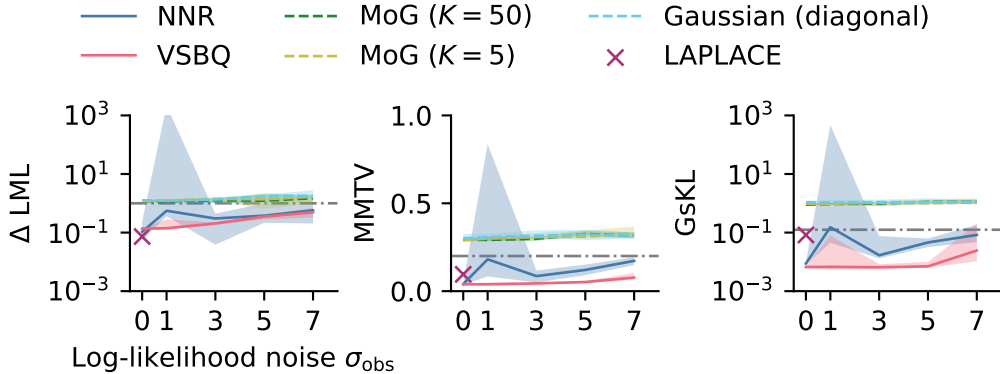


Figure 5: **Bayesian timing model.** Median ΔLML loss (left), MMTV (middle), and GsKL (right) as a function of the log-likelihood noise σ_{obs} for the Bayesian Timing model. Shaded areas are 95% CI of the median and grey dash-dotted horizontal lines are the rule-of-thumb thresholds for good performance ($\Delta\text{LML}=1$, $\text{MMTV}=0.2$, $\text{GsKL}=1/8$). VSBQ performs well across all noise levels and can outperform (noiseless) LAPLACE even under high log-likelihood noise, whereas NNR demonstrates less robustness with several failed runs. BBVI methods exhibit similar performance above the metric thresholds.

we use a heuristic ‘Fixed’ rule, which determines the source to be the same if the absolute difference between the visual and vestibular measurements is less than a threshold κ , i.e., $|z_{\text{vis}} - z_{\text{vest}}| < \kappa$. Additionally, the model incorporates a probability λ of the participant providing a random response [Acerbi et al., 2018]. The model parameters are $\theta = (\sigma_{\text{vis}}(c_{\text{low}}), \sigma_{\text{vis}}(c_{\text{med}}), \sigma_{\text{vis}}(c_{\text{high}}), \sigma_{\text{vest}}, \lambda, \kappa)$, with a total of $D = 6$ parameters. Here we fit data from participant S0 of Acerbi et al. [2018].

The performance metrics of all tested methods are plotted in Figure 6, as a function of log-likelihood observation noise. VSBQ consistently outputs a good posterior approximation and only exceeds the desirable metrics thresholds at large observation noise. LAPLACE works reasonably for the noiseless case, still worse than VSBQ, and slightly above the thresholds for MMTV and GsKL. In this problem, NNR performs well, slightly outperforming VSBQ in some metrics in a higher observation noise regime. BBVI with MoG ($K = 50$) performs well for low noise cases and becomes similar to BBVI with a diagonal Gaussian or MoG ($K = 5$) for high noise levels. BBVI with a full-rank Gaussian is excluded from the figure, as it yields poor results due to optimization challenges also in this case. We visualize the approximate and ground-truth posteriors in Supplementary Material C.6.

4.5 Additional analyses

We summarize here the results of a number of additional analyses reported in the Supplementary Material.

MAP estimation with Bayesian Adaptive Direct Search (BADs). We ran again all our experiments using optimization traces from a different optimization algorithm based on a hybrid Bayesian optimization approach [Garnett, 2023], namely Bayesian Adaptive Direct Search (BADs; Acerbi and Ma, 2017). BADs is a state-of-the-art optimization algorithm with wide application in computational neuroscience and other fields. We found the performance of VSBQ with BADs is almost identical to CMA-ES for three out of four benchmark problems (Two Moons, multivariate

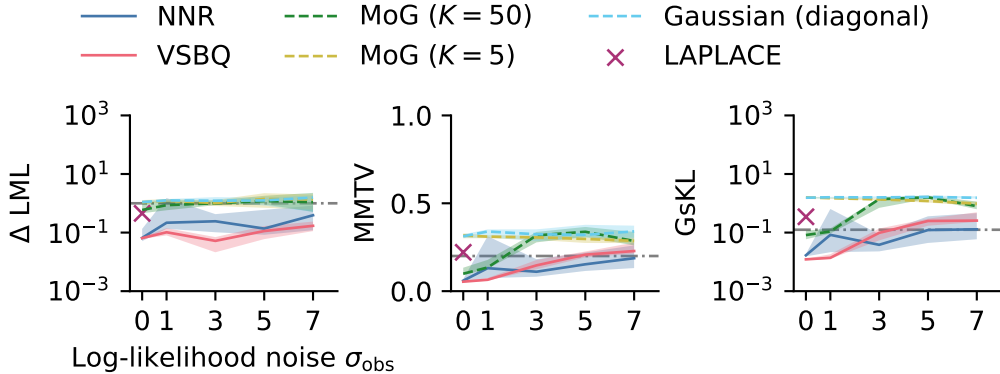


Figure 6: **Multisensory causal inference model.** Median ΔLML loss (left), MMTV (middle), and GsKL (right) as a function of the log-likelihood noise σ_{obs} for the Bayesian Timing model. Shaded areas are 95% CI of the median and grey dash-dotted horizontal lines are the rule-of-thumb thresholds for good performance ($\Delta\text{LML}=1$, $\text{MMTV}=0.2$, $\text{GsKL}=1/8$). VSBQ performs well across low to moderate noise levels and outperforms (noiseless) LAPLACE even at high noise levels. NNR also demonstrates strong performance across all noise levels. BBVI methods perform similarly and are above the thresholds, except for the MoG($K=50$) at low noise levels.

Rosenbrock-Gaussian, and Bayesian timing model), and slightly worse for the multisensory causal inference problem. See Supplementary Material C.5 for the full results and their discussion.

Runtime analysis. Ideally, running a post-process inference method should only take a relatively short time (*e.g.*, a few minutes), so we performed a detailed comparison of the runtimes of different algorithms on different computational architectures (CPU and GPU). Overall, we found that VSBQ takes several minutes on CPU and 1-3 minutes on GPU across the various problems we considered, meeting the speed desiderata of a post-process technique. NNR can take considerably longer, mainly due to multiple training runs required for hyperparameter selection. BBVI methods are not intended as post-processing approaches, making their runtime less directly relevant. The runtime of BBVI and Laplace approximation methods depends on the cost and the number of target density evaluations. Full results are reported in Supplementary Material C.7.

Posterior estimation: MCMC or variational inference? In the earlier paragraphs, we presented results obtained by approximating the target posterior density from the surrogate of the log density (Figure 1) via variational inference. A natural alternative is to instead run MCMC on the surrogate log-density [Rasmussen, 2003, Nemeth and Sherlock, 2018, Järvenpää et al., 2021, Gammal et al., 2022]. In Supplementary Material C.8, we provide experimental results showing that MCMC can underperform in this setting and discuss the reasons.

5 Discussion

In this paper, we introduced the framework of post-process, black-box Bayesian inference, and proposed a specific post-process algorithm, Variational Sparse Bayesian Quadrature (VSBQ). By recycling evaluations from previous MAP optimization runs, VSBQ enables full Bayesian inference at

a limited additional cost. In this section, we first discuss why surrogate-based approaches like VSBQ can be more effective than BBVI, followed by an exploration of the limitations of our method and potential directions for future work.

5.1 Why are surrogate-based approaches more effective than direct variational inference?

As demonstrated across a series of benchmarks, in our black-box setting surrogate-based methods like VSBQ and NNR produce high-quality solutions, whereas BBVI— which performs black-box variational inference directly on the target – struggles to effectively fit the target posterior, even when given $10\times$ target density evaluations. This disparity arises primarily from the high variance associated with the score function estimator in BBVI. While gradient-based variational inference using the reparameterization trick (such as automatic differentiation variational inference, or ADVI) empirically reduces variance and is more widely adopted [Titsias and Lázaro-Gredilla, 2014, Kucukelbir et al., 2017, Xu et al., 2019], it requires the target density to be differentiable with respect to the parameters. The black-box nature of the target model makes ADVI inapplicable in our considered scenarios. Surrogate-based methods address these challenges effectively. Fitting a surrogate model (e.g., a sparse Gaussian process for VSBQ or a neural network for NNR) to the target density offers two key advantages:

- a. These methods can fully leverage all existing target density evaluations from various sources, effectively interpolating and smoothing across (noisy) observations.
- b. The surrogate model resolves the non-differentiability issue, allowing gradient-based variational inference to be applied to the surrogate density, which is differentiable (e.g., via automatic differentiation) by construction.

5.2 Limitations and future work

Arguably, post-process inference via VSBQ is constrained to low-dimensional problems for several reasons: as the dimension increases, pre-existing evaluations from MAP optimizations become less likely to cover the majority of the posterior mass [Vershynin, 2018, Chapter 3.3.3]. Moreover, the MAP estimate may become not meaningful or even ill-defined in certain settings, *e.g.*, when the likelihood is unbounded [Gelman et al., 2013]. While a larger number of evaluations might expand the range of tractable dimensions, the curse of dimensionality poses challenges in approximating a function without additional structural assumptions. A potential solution to address the issue of lack of coverage is active sampling, that is the ability to acquire new log-density evaluations where needed [Osborne et al., 2012, Acerbi, 2020, Järvenpää et al., 2021, De Souza et al., 2022]. Active sampling would need one or multiple rounds of ad-hoc function evaluations and subsequent surrogate model updates, which would substantially increase the post-processing time [De Souza et al., 2022]. Finding efficient methods for active learning for post-process inference is left for future research. Despite the above limitations, the relatively cheap cost of our method makes it still valuable for quickly constructing a tractable initial approximation of the posterior, potentially useful to inform subsequent runs of MCMC or other inference methods [Zhang et al., 2022].

An important feature of approximate inference methods is the availability of diagnostics to assess the reliability of inference [Vehtari et al., 2021, Yao et al., 2018]. A general-purpose inference diagnostic consists of posterior-predictive checks, *i.e.*, testing that synthetic data generated from parameters sampled from the posterior are compatible with the actual data [Gelman et al., 2013]. As an additional diagnostic, VSBQ provides the standard deviation of the ELBO, ELBO_{sd} , which can be calculated via sparse Bayesian quadrature (Eq. 23). ELBO_{sd} reflects the uncertainty of the sparse GP

prediction in regions where the variational posterior has non-negligible mass. Therefore, it can serve as a useful diagnostic in that solutions with $\text{ELBO}_{\text{sd}} \gg 1$ should not be trusted. However, as is often the case with inference diagnostics, a small ELBO_{sd} does *not* guarantee the validity of the approximate variational posterior [Acerbi, 2018]. As a practical validation approach, we recommend running VSBQ multiple times by dropping for example 20% of the training set and checking the consistency of the approximate posteriors via a form of cross-validation. Visualization of the posterior together with the locations of the evaluated points is also helpful for validating that the approximate posterior is supported by actual evaluations, as opposed to escaping from the training points region, leading to ‘hallucinated’ posterior regions [De Souza et al., 2022]. We further discuss this ‘hallucination’ problem in Supplementary Material C.8. Finally, if additional exact log-density evaluations are possible, one can leverage Pareto smoothed importance sampling [Vehtari et al., 2015] for correcting and validating the approximate posterior [Yao et al., 2018].

Noise shaping, a principled heuristic introduced in Section 3.3, is an important component of VSBQ. Noise shaping effectively downweights the low-density observations, providing a straightforward probabilistic explanation. This approach is closely related to, but distinct from, the weighted KL divergence method in McIntire et al. [2016] and the inducing points allocation strategy in Moss et al. [2023]. We chose the noise shaping function out of theoretical and empirical considerations (see Supplementary Material C.1), and further work is needed to make it a general tool for surrogate modeling, *e.g.*, via adaptive techniques, and to provide a sounder theoretical grounding.

Finally, in this work we explored sparse GP surrogates via SGPR due to its numerical convenience (*i.e.*, closed-form solutions for the sparse GP posterior), but SGPR is also somewhat limited in scalability and restricted to Gaussian observations. A natural extension of our work would consist of extending VSBQ to *stochastic* variational GPs (SVGP; Hensman et al., 2013, 2015), which are able to handle nearly arbitrarily large datasets and non-Gaussian observations of the target density. Additionally, as our experiments with neural network regression (NNR) suggested, deep neural networks can be competitive surrogates for log-density function modeling in the regime of large datasets. Exploring better regularization and uncertainty quantification for neural networks [Daxberger et al., 2021, Immer et al., 2023] is a promising future direction with the potential to enhance the effectiveness of deep learning within the framework of post-process inference.

5.3 Conclusions

In this paper, we showed the application of post-process approximate Bayesian inference and VSBQ as a valuable tool for quickly constructing a posterior approximation at a low cost by recycling existing log-density evaluations. With further developments in diagnostics, theoretical analysis, and scalability, the framework of post-process inference has the potential to make Bayesian inference more accessible and efficient for a wide range of applications.

Acknowledgments

This work was supported by the Research Council of Finland Flagship programme: Finnish Center for Artificial Intelligence FCAI. The authors wish to thank the Finnish Computing Competence Infrastructure (FCCI) for supporting this project with computational and data storage resources.

Grégoire Clarté completed part of the work when he was at the Department of Computer Science, University of Helsinki, Finland, where he was supported by the Research Council of Finland Flagship programme: Finnish Center for Artificial Intelligence FCAI.

Chengkun Li, Martin Jørgensen and Luigi Acerbi were supported by the Research Council of Finland (grants number 356498 and 358980 to Luigi Acerbi).

References

- Luigi Acerbi. Variational Bayesian Monte Carlo. *Advances in Neural Information Processing Systems*, 31:8222–8232, 2018. [2](#), [3](#), [5](#), [6](#), [9](#), [17](#), [25](#), [41](#), [62](#)
- Luigi Acerbi. An exploration of acquisition and mean functions in Variational Bayesian Monte Carlo. *Proceedings of The 1st Symposium on Advances in Approximate Bayesian Inference (PMLR)*, 96: 1–10, 2019. [5](#)
- Luigi Acerbi. Variational Bayesian Monte Carlo with noisy likelihoods. *Advances in Neural Information Processing Systems*, 33:8211–8222, 2020. [3](#), [6](#), [18](#), [21](#), [24](#), [41](#)
- Luigi Acerbi and Wei Ji Ma. Practical Bayesian optimization for model fitting with Bayesian adaptive direct search. *Advances in Neural Information Processing Systems*, 30:1834–1844, 2017. [2](#), [17](#), [22](#), [44](#)
- Luigi Acerbi, Daniel M Wolpert, and Sethu Vijayakumar. Internal representations of temporal statistics and feedback calibrate motor-sensory interval timing. *PLoS Computational Biology*, 8(11):e1002771, 2012. [2](#), [21](#)
- Luigi Acerbi, Kalpana Dokka, Dora E Angelaki, and Wei Ji Ma. Bayesian comparison of explicit and implicit causal inference strategies in multisensory heading perception. *PLoS Computational Biology*, 14(7):e1006110, 2018. [2](#), [9](#), [21](#), [22](#)
- Masaki Adachi, Satoshi Hayakawa, Martin Jørgensen, Harald Oberhauser, and Michael A Osborne. Fast Bayesian inference with batch Bayesian quadrature via kernel recombination. *Advances in Neural Information Processing Systems*, 35:16533–16547, 2022. [5](#)
- Eli Bingham, Jonathan P. Chen, Martin Jankowiak, Fritz Obermeyer, Neeraj Pradhan, Theofanis Karaletsos, Rohit Singh, Paul Szerlip, Paul Horsfall, and Noah D. Goodman. Pyro: Deep Universal Probabilistic Programming, October 2018. [43](#)
- Christopher M Bishop. *Pattern Recognition and Machine Learning*. Springer, 2006. [3](#)
- David M Blei, Alp Kucukelbir, and Jon D McAuliffe. Variational inference: A review for statisticians. *Journal of the American Statistical Association*, 112(518):859–877, 2017. [2](#), [3](#)
- James Bradbury, Roy Frostig, Peter Hawkins, Matthew James Johnson, Chris Leary, Dougal Maclaurin, George Necula, Adam Paszke, Jake VanderPlas, Skye Wanderman-Milne, and Qiao Zhang. JAX: composable transformations of Python+NumPy programs. <https://github.com/google/jax>, 2018. [63](#)
- Per A Brodtkorb and John D’Errico. numdifftools 0.9.41. <https://github.com/pbrod/numdifftools>, 2022. [17](#)
- Thang Bui and Richard Turner. On the paper: Variational learning of inducing variables in Sparse Gaussian Processes (Titsias, 2009). <https://citeseerx.ist.psu.edu/document?repid=rep1&type=pdf&doi=a154c66f945184384bb5056204421c242419a286>, 2014. Accessed: 2022-10-19. [33](#)
- Kenneth P Burnham and David R Anderson. *Model selection and multimodel inference: a practical information-theoretic approach*. Springer Science & Business Media, 2003. [18](#)

- David R. Burt, Carl Edward Rasmussen, and Mark van der Wilk. Convergence of sparse variational inference in Gaussian processes regression. *Journal of Machine Learning Research*, 21(131):1–63, 2020. [11](#), [12](#)
- Yinan Cao, Christopher Summerfield, Hame Park, Bruno Lucio Giordano, and Christoph Kayser. Causal inference in the multisensory brain. *Neuron*, 102(5):1076–1087, 2019. [2](#), [21](#)
- Bob Carpenter, Andrew Gelman, Matthew D Hoffman, Daniel Lee, Ben Goodrich, Michael Betancourt, Marcus Brubaker, Jiqiang Guo, Peter Li, and Allen Riddell. Stan: A probabilistic programming language. *Journal of Statistical Software*, 76(1), 2017. [17](#)
- Laming Chen, Guoxin Zhang, and Eric Zhou. Fast greedy map inference for determinantal point process to improve recommendation diversity. *Advances in Neural Information Processing Systems*, 31, 2018. [11](#)
- Erik Daxberger, Agustinus Kristiadi, Alexander Immer, Runa Eschenhagen, Matthias Bauer, and Philipp Hennig. Laplace Redux - Effortless Bayesian Deep Learning. In *Advances in Neural Information Processing Systems*, volume 34, pages 20089–20103. Curran Associates, Inc., 2021. [17](#), [25](#)
- Daniel A De Souza, Diego Mesquita, Samuel Kaski, and Luigi Acerbi. Parallel MCMC without embarrassing failures. *International Conference on Artificial Intelligence and Statistics*, pages 1786–1804, 2022. [5](#), [9](#), [24](#), [25](#), [62](#)
- D. Foreman-Mackey, D. W. Hogg, D. Lang, and J. Goodman. emcee: The mcmc hammer. *PASP*, 125:306–312, 2013. doi: 10.1086/670067. [15](#)
- Yarin Gal. *Uncertainty in Deep Learning*. Phd thesis, University of Cambridge, 2016. [15](#)
- Jonas El Gammal, Nils Schöneberg, Jesús Torrado, and Christian Fidler. Fast and robust Bayesian Inference using Gaussian Processes with GPry, November 2022. [5](#), [9](#), [23](#), [40](#)
- Roman Garnett. *Bayesian Optimization*. Cambridge University Press, 2023. [5](#), [22](#), [44](#)
- Andrew Gelman, John B Carlin, Hal S Stern, David B Dunson, Aki Vehtari, and Donald B Rubin. *Bayesian Data Analysis (3rd edition)*. CRC Press, 2013. [1](#), [2](#), [24](#)
- Andrew Gelman, Aki Vehtari, Daniel Simpson, Charles C Margossian, Bob Carpenter, Yuling Yao, Lauren Kennedy, Jonah Gabry, Paul-Christian Bürkner, and Martin Modrák. Bayesian workflow. *arXiv preprint arXiv:2011.01808*, 2020. [1](#)
- Charles J Geyer. Estimating normalizing constants and reweighting mixtures. Technical Report 568, School of Statistics, University of Minnesota, 1994. [18](#), [42](#)
- Zoubin Ghahramani. Probabilistic machine learning and artificial intelligence. *Nature*, 521(7553): 452–459, 2015. [1](#)
- Zoubin Ghahramani and Carl Rasmussen. Bayesian Monte Carlo. In S. Becker, S. Thrun, and K. Obermayer, editors, *Advances in Neural Information Processing Systems*, volume 15. MIT Press, 2002a. [5](#), [6](#), [36](#)
- Zoubin Ghahramani and Carl E Rasmussen. Bayesian Monte Carlo. *Advances in Neural Information Processing Systems*, 15:505–512, 2002b. [5](#)

- Ian Goodfellow, Yoshua Bengio, and Aaron Courville. *Deep Learning*. MIT Press, 2016. <http://www.deeplearningbook.org>. 16
- Robert B Gramacy and Herbert KH Lee. Cases for the nugget in modeling computer experiments. *Statistics and Computing*, 22(3):713–722, 2012. 5
- Tom Gunter, Michael A Osborne, Roman Garnett, Philipp Hennig, and Stephen J Roberts. Sampling for inference in probabilistic models with fast Bayesian quadrature. *Advances in Neural Information Processing Systems*, 27:2789–2797, 2014. 5
- Michael U Gutmann and Jukka Corander. Bayesian optimization for likelihood-free inference of simulator-based statistical models. *The Journal of Machine Learning Research*, 17(1):4256–4302, 2016. 5
- Nikolaus Hansen. The CMA Evolution Strategy: A Tutorial. *arXiv preprint arXiv:1604.00772*, April 2016. 2, 17
- Nikolaus Hansen, Sibylle D Müller, and Petros Koumoutsakos. Reducing the time complexity of the derandomized evolution strategy with covariance matrix adaptation (CMA-ES). *Evolutionary Computation*, 11(1):1–18, 2003. 2
- James B Heald, Máté Lengyel, and Daniel M Wolpert. Contextual inference underlies the learning of sensorimotor repertoires. *Nature*, 600(7889):489–493, 2021. 2
- James Hensman, Nicolò Fusi, and Neil D. Lawrence. Gaussian processes for big data. In Ann Nicholson and Padhraic Smyth, editors, *Uncertainty in Artificial Intelligence*, volume 29. AUAI Press, 2013. 7, 25
- James Hensman, Alexander Matthews, and Zoubin Ghahramani. Scalable variational Gaussian process classification. In *Artificial Intelligence and Statistics*, pages 351–360. PMLR, 2015. 7, 14, 25
- Bobby Huggins, Chengkun Li, Marlon Tobaben, Mikko J Aarnos, and Luigi Acerbi. PyVBMC: Efficient Bayesian inference in Python. *Journal of Open Source Software*, 8(86):5428, 2023. doi: 10.21105/joss.05428. 6
- Alexander Immer, Emanuele Palumbo, Alexander Marx, and Julia Vogt. Effective Bayesian Heteroscedastic Regression with Deep Neural Networks. *Advances in Neural Information Processing Systems*, 36:53996–54019, December 2023. 25
- Marko Järvenpää, Michael U Gutmann, Aki Vehtari, and Pekka Marttinen. Parallel Gaussian process surrogate Bayesian inference with noisy likelihood evaluations. *Bayesian Analysis*, 16(1):147–178, 2021. 5, 9, 12, 20, 23, 24, 62
- Mehrdad Jazayeri and Michael N Shadlen. Temporal context calibrates interval timing. *Nature Neuroscience*, 13(8):1020–1026, 2010. 21
- Michael I Jordan, Zoubin Ghahramani, Tommi S Jaakkola, and Lawrence K Saul. An introduction to variational methods for graphical models. *Machine Learning*, 37(2):183–233, 1999. 3
- Diederik P Kingma and Jimmy Ba. Adam: A method for stochastic optimization. *Proceedings of the 3rd International Conference on Learning Representations*, 2014. 6, 15

- Diederik P Kingma and Max Welling. Auto-encoding variational Bayes. *Proceedings of the 2nd International Conference on Learning Representations*, 2013. 6, 15, 16, 44
- Konrad P Kording, Ulrik Beierholm, Wei Ji Ma, Steven Quartz, Joshua B Tenenbaum, and Ladan Shams. Causal inference in multisensory perception. *PLoS One*, 2(9):e943, 2007. 21
- Siddarth Krishnamoorthy, Satvik Mehul Mashkaria, and Aditya Grover. Diffusion Models for Black-Box Optimization. In *Proceedings of the 40th International Conference on Machine Learning*, pages 17842–17857. PMLR, July 2023. 3
- Alp Kucukelbir, Dustin Tran, Rajesh Ranganath, Andrew Gelman, and David M. Blei. Automatic differentiation variational inference. *Journal of Machine Learning Research*, 18(1):430–474, January 2017. ISSN 1532-4435. 24, 44
- Chengkun Li, Grégoire Clarté, and Luigi Acerbi. Fast post-process Bayesian inference with Sparse Variational Bayesian Monte Carlo. *arXiv preprint arXiv:2303.05263v1*, 2023. 10
- Dong C. Liu and Jorge Nocedal. On the limited memory BFGS method for large scale optimization. *Mathematical Programming*, 45(1):503–528, August 1989. ISSN 1436-4646. doi: 10.1007/BF01589116. 2
- Ilya Loshchilov and Frank Hutter. Decoupled weight decay regularization. In *International Conference on Learning Representations*, 2019. 16, 43, 44
- Wei Ji Ma, Konrad Paul Kording, and Daniel Goldreich. *Bayesian models of perception and action: An introduction*. MIT press, 2023. 2, 21
- David JC MacKay. *Information theory, inference and learning algorithms*. Cambridge University Press, 2003. 17
- Wesley J Maddox, Samuel Stanton, and Andrew G Wilson. Conditioning sparse variational Gaussian processes for online decision-making. In *Advances in Neural Information Processing Systems*, volume 34, pages 6365–6379. Curran Associates, Inc., 2021. 11, 36
- Alexander G. de G. Matthews, Mark van der Wilk, Tom Nickson, Keisuke. Fujii, Alexis Boukouvalas, Pablo León-Villagrà, Zoubin Ghahramani, and James Hensman. GPflow: A Gaussian process library using TensorFlow. *Journal of Machine Learning Research*, 18(40):1–6, apr 2017. 34, 36
- Mitchell McIntire, Daniel Ratner, and Stefano Ermon. Sparse Gaussian Processes for Bayesian Optimization. In *UAI*, 2016. 25
- Andrew C Miller, Nicholas Foti, and Ryan P Adams. Variational boosting: Iteratively refining posterior approximations. *Proceedings of the 34th International Conference on Machine Learning*, 70:2420–2429, 2017. 4, 6
- Henry B. Moss, Sebastian W. Ober, and Victor Picheny. Inducing Point Allocation for Sparse Gaussian Processes in High-Throughput Bayesian Optimisation. In *Proceedings of The 26th International Conference on Artificial Intelligence and Statistics*, pages 5213–5230. PMLR, April 2023. ISSN: 2640-3498. 25
- Anirbit Mukherjee, Amitabh Basu, Raman Arora, and Poorya Mianjy. Understanding Deep Neural Networks with Rectified Linear Units. In *International Conference on Learning Representations*, 2018. 16

- Radford M Neal. Slice sampling. *Annals of Statistics*, 31(3):705–741, 2003. [62](#)
- Christopher Nemeth and Chris Sherlock. Merging MCMC subposteriors through Gaussian-process approximations. *Bayesian Analysis*, 13(2):507–530, 2018. [5](#), [23](#), [62](#)
- Elyse H Norton, Luigi Acerbi, Wei Ji Ma, and Michael S Landy. Human online adaptation to changes in prior probability. *PLoS Computational Biology*, 15(7):e1006681, 2019. [2](#)
- Anthony O’Hagan. Bayes–Hermite quadrature. *Journal of Statistical Planning and Inference*, 29(3):245–260, 1991. [2](#), [5](#)
- Michael Osborne, David K Duvenaud, Roman Garnett, Carl E Rasmussen, Stephen J Roberts, and Zoubin Ghahramani. Active learning of model evidence using Bayesian quadrature. *Advances in Neural Information Processing Systems*, 25:46–54, 2012. [5](#), [24](#)
- Adam Paszke, Sam Gross, Francisco Massa, Adam Lerer, James Bradbury, Gregory Chanan, Trevor Killeen, Zeming Lin, Natalia Gimelshein, Luca Antiga, Alban Desmaison, Andreas Köpf, Edward Yang, Zach DeVito, Martin Raison, Alykhan Tejani, Sasank Chilamkurthy, Benoit Steiner, Lu Fang, Junjie Bai, and Soumith Chintala. PyTorch: An Imperative Style, High-Performance Deep Learning Library, December 2019. [63](#)
- Payam Piray, Amir Dezfouli, Tom Heskes, Michael J Frank, and Nathaniel D Daw. Hierarchical Bayesian inference for concurrent model fitting and comparison for group studies. *PLoS Computational Biology*, 15(6):e1007043, 2019. [17](#)
- Alexandre Pouget, Jeffrey M Beck, Wei Ji Ma, and Peter E Latham. Probabilistic brains: Knowns and unknowns. *Nature Neuroscience*, 16(9):1170–1178, 2013. [21](#)
- Rajesh Ranganath, Sean Gerrish, and David Blei. Black box variational inference. In *Artificial Intelligence and Statistics*, pages 814–822. PMLR, 2014. [15](#), [42](#)
- C. Rasmussen and C. K. I. Williams. *Gaussian Processes for Machine Learning*. MIT Press, 2006. [2](#), [5](#), [7](#)
- Carl Edward Rasmussen. Gaussian processes to speed up hybrid Monte Carlo for expensive Bayesian integrals. *Bayesian Statistics*, 7:651–659, 2003. [5](#), [23](#), [62](#)
- Christian Robert and George Casella. *Monte Carlo Statistical Methods*. Springer Texts in Statistics. Springer-Verlag, New York, 2 edition, 2004. ISBN 978-0-387-21239-5. doi: 10.1007/978-1-4757-4145-2. [2](#)
- Christian P Robert et al. *The Bayesian choice: from decision-theoretic foundations to computational implementation*, volume 2. Springer, 2007. [1](#)
- Ladan Shams and Ulrik Beierholm. Bayesian causal inference: A unifying neuroscience theory. *Neuroscience & Biobehavioral Reviews*, 137:104619, 2022. [21](#)
- Gurjeet Sangra Singh and Luigi Acerbi. PyBADS: Fast and robust black-box optimization in Python. *Journal of Open Source Software*, 9(94):5694, 2024. doi: 10.21105/joss.05694. [2](#), [17](#)
- Edward Snelson and Zoubin Ghahramani. Sparse Gaussian Processes using Pseudo-inputs. In *Advances in Neural Information Processing Systems*, volume 18. MIT Press, 2005. [7](#)

- Michalis Titsias. Variational learning of inducing variables in sparse Gaussian processes. In *Artificial intelligence and statistics*, pages 567–574. PMLR, 2009. [2](#), [7](#), [11](#)
- Michalis Titsias and Miguel Lázaro-Gredilla. Doubly Stochastic Variational Bayes for non-Conjugate Inference. In *Proceedings of the 31st International Conference on Machine Learning*, pages 1971–1979. PMLR, June 2014. [24](#)
- Brandon Trabucco, Xinyang Geng, Aviral Kumar, and Sergey Levine. Design-Bench: Benchmarks for Data-Driven Offline Model-Based Optimization. In *Proceedings of the 39th International Conference on Machine Learning*, pages 21658–21676. PMLR, June 2022. [3](#)
- Alexandre B Tsybakov. *Introduction à l'estimation non paramétrique*, volume 41. Springer Science & Business Media, 2003. [38](#)
- Bas van Opheusden, Luigi Acerbi, and Wei Ji Ma. Unbiased and efficient log-likelihood estimation with inverse binomial sampling. *PLOS Computational Biology*, 16(12):e1008483, 2020. doi: 10.1371/journal.pcbi.1008483. [1](#), [5](#), [20](#)
- Aki Vehtari, Andrew Gelman, and Jonah Gabry. Pareto smoothed importance sampling. *arXiv preprint arXiv:1507.02646*, 2015. [25](#)
- Aki Vehtari, Andrew Gelman, Daniel Simpson, Bob Carpenter, and Paul-Christian Bürkner. Rank-Normalization, Folding, and Localization: An Improved \hat{R} for Assessing Convergence of MCMC (with Discussion). *Bayesian Analysis*, 16(2):667–718, June 2021. ISSN 1936-0975, 1931-6690. doi: 10.1214/20-BA1221. [24](#)
- Roman Vershynin. *High-Dimensional Probability: An Introduction with Applications in Data Science*. Number 47 in Cambridge Series in Statistical and Probabilistic Mathematics. Cambridge University Press, 2018. ISBN 978-1-108-41519-4. [24](#)
- Hongqiao Wang and Jinglai Li. Adaptive Gaussian process approximation for Bayesian inference with expensive likelihood functions. *Neural Computation*, pages 1–23, 2018. [5](#)
- Houston Warren and Fabio Ramos. Fast Fourier Bayesian Quadrature. In *Proceedings of The 27th International Conference on Artificial Intelligence and Statistics*, pages 4555–4563. PMLR, April 2024. [10](#)
- Robert C Wilson and Anne GE Collins. Ten simple rules for the computational modeling of behavioral data. *Elife*, 8:e49547, 2019. [2](#)
- Simon N Wood. Statistical inference for noisy nonlinear ecological dynamic systems. *Nature*, 466(7310):1102–1104, 2010. [1](#), [5](#), [20](#)
- Ming Xu, Matias Quiroz, Robert Kohn, and Scott A. Sisson. Variance reduction properties of the reparameterization trick. In *Proceedings of the Twenty-Second International Conference on Artificial Intelligence and Statistics*, pages 2711–2720. PMLR, April 2019. [15](#), [24](#)
- Yuling Yao, Aki Vehtari, Daniel Simpson, and Andrew Gelman. Yes, but did it work?: Evaluating variational inference. *Proceedings of the 35th International Conference on Machine Learning*, 80: 5581–5590, 2018. [24](#), [25](#)
- Yuling Yao, Aki Vehtari, and Andrew Gelman. Stacking for non-mixing Bayesian computations: The curse and blessing of multimodal posteriors. *Journal of Machine Learning Research*, 23(79): 1–45, 2022. [2](#)

- Aspen H Yoo, Luigi Acerbi, and Wei Ji Ma. Uncertainty is maintained and used in working memory. *Journal of Vision*, 21(8):13–13, 2021. [2](#)
- Guodong Zhang, Chaoqi Wang, Bowen Xu, and Roger Grosse. Three mechanisms of weight decay regularization. In *International Conference on Learning Representations*, 2019. [44](#)
- Lu Zhang, Bob Carpenter, Andrew Gelman, and Aki Vehtari. Pathfinder: Parallel quasi-Newton variational inference. *Journal of Machine Learning Research*, 23(306):1–49, 2022. [2](#), [24](#)
- Yanli Zhou, Luigi Acerbi, and Wei Ji Ma. The role of sensory uncertainty in simple contour integration. *PLoS Computational Biology*, 16(11):e1006308, 2020. [2](#)

Supplementary Material

A Analytical formulae

In this section, we provide analytical formulae and derivations omitted from the main paper. In addition to the notation used in the main text, we denote here with \mathbf{f} the vector $f(\mathbf{X})$, and $\mathbf{m}_{\mathbf{u}}$ and $\mathbf{R}_{\mathbf{uu}}$ are, respectively, the mean and covariance matrix of the optimal variational distribution at inducing points \mathbf{Z} , summarized by ψ . We use κ for the Gaussian process (GP) kernel, and the following notations for the matrices $\mathbf{K}_{\mathbf{X},\mathbf{X}} \equiv \kappa(\mathbf{X}, \mathbf{X})$ (and similarly for \mathbf{Z}). We write the matrix of observation noise at each point of \mathbf{X} as $\mathbf{S} = \text{diag}(\sigma_{\text{obs}}^2(\mathbf{X})) = \text{diag}(s_n^2)$, $n = 1, 2, \dots, N$, where N is the number of training points.

A.1 Optimal variational parameters, heteroskedastic case

Here we describe how to derive the optimal variational parameters $\mathbf{m}_{\mathbf{u}}$ and $\mathbf{R}_{\mathbf{uu}}$ for the heteroskedastic observation noise case. Our derivations mostly follow [Bui and Turner \[2014\]](#). The only difference is that we consider the heteroskedastic case instead of the homoskedastic case.

Zero-mean case. First, we compute the optimal parameters for a sparse GP with a zero-mean function. From [Bui and Turner \[2014\]](#), the quantities that need to be adapted for heteroskedastic noise are $\mathcal{M}(\mathbf{y}, \mathbf{u})$ and $H(\mathbf{y}, \mathbf{u}) \equiv \exp \mathcal{M}(\mathbf{y}, \mathbf{u})$.

$$\begin{aligned}
 \mathcal{M}(\mathbf{y}, \mathbf{u}) &= \int p(\mathbf{f} | \mathbf{u}) \log p(\mathbf{y} | \mathbf{f}) d\mathbf{f} \\
 &= \int \mathcal{N}(\mathbf{f}; \mathbf{K}_{\mathbf{X},\mathbf{Z}} \mathbf{K}_{\mathbf{Z},\mathbf{Z}}^{-1} \mathbf{u}, \mathbf{K}_{\mathbf{X},\mathbf{X}} - \mathbf{K}_{\mathbf{X},\mathbf{Z}} \mathbf{K}_{\mathbf{Z},\mathbf{Z}}^{-1} \mathbf{K}_{\mathbf{Z},\mathbf{X}}) \log [\mathcal{N}(\mathbf{y}; \mathbf{f}, \mathbf{S})] d\mathbf{f} \\
 &\text{(Define } \mathbf{A} = \mathbf{K}_{\mathbf{X},\mathbf{Z}} \mathbf{K}_{\mathbf{Z},\mathbf{Z}}^{-1} \mathbf{u} \text{ and } \mathbf{B} = \mathbf{K}_{\mathbf{X},\mathbf{X}} - \mathbf{K}_{\mathbf{X},\mathbf{Z}} \mathbf{K}_{\mathbf{Z},\mathbf{Z}}^{-1} \mathbf{K}_{\mathbf{Z},\mathbf{X}} \text{ for brevity.)} \\
 &= \int \mathcal{N}(\mathbf{f}; \mathbf{A}, \mathbf{B}) \left[-\frac{N}{2} \log(2\pi) - \frac{1}{2} \sum_{n=1}^N \log s_n^2 - \frac{1}{2} (\mathbf{y} - \mathbf{f})^\top \mathbf{S}^{-1} (\mathbf{y} - \mathbf{f}) \right] d\mathbf{f} \\
 &= \int \mathcal{N}(\mathbf{f}; \mathbf{A}, \mathbf{B}) \left[-\frac{N}{2} \log(2\pi) - \frac{1}{2} \sum_{n=1}^N \log s_n^2 - \frac{1}{2} \text{Tr} \left((\mathbf{y}\mathbf{y}^\top - 2\mathbf{y}\mathbf{f}^\top + \mathbf{f}\mathbf{f}^\top) \mathbf{S}^{-1} \right) \right] d\mathbf{f} \\
 &= -\frac{N}{2} \log(2\pi) - \frac{1}{2} \sum_{n=1}^N \log s_n^2 - \frac{1}{2} \text{Tr} \left((\mathbf{y}\mathbf{y}^\top - 2\mathbf{y}\mathbf{A}^\top + \mathbf{A}\mathbf{A}^\top + \mathbf{B}) \mathbf{S}^{-1} \right) \\
 &= -\frac{1}{2} \text{Tr}(\mathbf{B}\mathbf{S}^{-1}) + \log [\mathcal{N}(\mathbf{y}; \mathbf{A}, \mathbf{S})].
 \end{aligned}$$

According to [Bui and Turner \[2014\]](#), the optimal variational distribution at inducing points \mathbf{Z} is:

$$\begin{aligned}
 \tilde{p}(\mathbf{u}) &\propto p(\mathbf{u}) \exp(\mathcal{M}(\mathbf{y}, \mathbf{u})) \\
 &\propto \exp \left[-\frac{1}{2} \mathbf{u}^\top (\mathbf{K}_{\mathbf{Z},\mathbf{Z}}^{-1} \mathbf{K}_{\mathbf{Z},\mathbf{X}} \mathbf{S}^{-1} \mathbf{K}_{\mathbf{X},\mathbf{Z}} \mathbf{K}_{\mathbf{Z},\mathbf{Z}}^{-1} + \mathbf{K}_{\mathbf{Z},\mathbf{Z}}^{-1}) \mathbf{u} + \mathbf{u}^\top \mathbf{K}_{\mathbf{Z},\mathbf{Z}}^{-1} \mathbf{K}_{\mathbf{Z},\mathbf{X}} \mathbf{S}^{-1} \mathbf{y} \right] \\
 &= \mathcal{N}(\mathbf{K}_{\mathbf{Z},\mathbf{Z}} \boldsymbol{\Sigma} \mathbf{K}_{\mathbf{Z},\mathbf{X}} \mathbf{S}^{-1} \mathbf{y}, \mathbf{K}_{\mathbf{Z},\mathbf{Z}} \boldsymbol{\Sigma} \mathbf{K}_{\mathbf{Z},\mathbf{Z}}) \\
 &\triangleq \mathcal{N}(\mathbf{m}_{\mathbf{u}}, \mathbf{R}_{\mathbf{uu}}),
 \end{aligned}$$

where $\Sigma = (\mathbf{K}_{\mathbf{Z},\mathbf{X}}\mathbf{S}^{-1}\mathbf{K}_{\mathbf{X},\mathbf{Z}} + \mathbf{K}_{\mathbf{Z},\mathbf{Z}})^{-1}$. The evidence lower bound is GP-ELBO = $\log(\mathcal{Z})$, where:

$$\begin{aligned}\mathcal{Z} &= \int H(\mathbf{y}, \mathbf{u})p(\mathbf{u})d\mathbf{u} \\ &= \int \exp\left(-\frac{1}{2}\text{Tr}(\mathbf{B}\mathbf{S}^{-1})\right) \mathcal{N}(\mathbf{y}; \mathbf{A}, \mathbf{S}) \mathcal{N}(\mathbf{u}; \mathbf{0}, \mathbf{K}_{\mathbf{Z},\mathbf{Z}}) d\mathbf{u} \\ &= \mathcal{N}(\mathbf{y}; \mathbf{0}, \mathbf{S} + \mathbf{K}_{\mathbf{X},\mathbf{Z}}\mathbf{K}_{\mathbf{Z},\mathbf{Z}}^{-1}\mathbf{K}_{\mathbf{Z},\mathbf{X}}) \exp\left(-\frac{1}{2}\text{Tr}(\mathbf{B}\mathbf{S}^{-1})\right).\end{aligned}$$

Thus, the ELBO writes:

$$\begin{aligned}\text{GP-ELBO} &= \log \mathcal{Z} \\ &= \log \mathcal{N}(\mathbf{y}; \mathbf{0}, \mathbf{S} + \mathbf{K}_{\mathbf{X},\mathbf{Z}}\mathbf{K}_{\mathbf{Z},\mathbf{Z}}^{-1}\mathbf{K}_{\mathbf{Z},\mathbf{X}}) - \frac{1}{2}\text{Tr}(\mathbf{B}\mathbf{S}^{-1}).\end{aligned}$$

Non-zero mean case. In the case of a non-zero mean function, we have:

$$\mathbf{A} = m(\mathbf{X}) + \mathbf{K}_{\mathbf{X},\mathbf{Z}}\mathbf{K}_{\mathbf{Z},\mathbf{Z}}^{-1}(\mathbf{u} - m(\mathbf{Z})),$$

which leads to:

$$\begin{aligned}\tilde{p}(\mathbf{u}) &\propto p(\mathbf{u}) \exp(\mathcal{M}) \\ &\propto \exp\left[-\frac{1}{2}\mathbf{u}^\top (\mathbf{K}_{\mathbf{Z},\mathbf{Z}}^{-1}\mathbf{K}_{\mathbf{Z},\mathbf{X}}\mathbf{S}^{-1}\mathbf{K}_{\mathbf{X},\mathbf{Z}}\mathbf{K}_{\mathbf{Z},\mathbf{Z}}^{-1} + \mathbf{K}_{\mathbf{Z},\mathbf{Z}}^{-1})\mathbf{u}\right. \\ &\quad \left. + \mathbf{u}^\top [\mathbf{K}_{\mathbf{Z},\mathbf{Z}}^{-1}\mathbf{K}_{\mathbf{Z},\mathbf{X}}\mathbf{S}^{-1}(\mathbf{y} - m(\mathbf{X}) + \mathbf{K}_{\mathbf{X},\mathbf{Z}}\mathbf{K}_{\mathbf{Z},\mathbf{Z}}^{-1}m(\mathbf{Z})) + \mathbf{K}_{\mathbf{Z},\mathbf{Z}}^{-1}m(\mathbf{Z})]\right] \\ &= \mathcal{N}(\mathbf{K}_{\mathbf{Z},\mathbf{Z}}\Sigma[\mathbf{K}_{\mathbf{Z},\mathbf{X}}\mathbf{S}^{-1}(\mathbf{y} - m(\mathbf{X}) + \mathbf{K}_{\mathbf{X},\mathbf{Z}}\mathbf{K}_{\mathbf{Z},\mathbf{Z}}^{-1}m(\mathbf{Z})) + m(\mathbf{Z})], \mathbf{K}_{\mathbf{Z},\mathbf{Z}}\Sigma\mathbf{K}_{\mathbf{Z},\mathbf{Z}}),\end{aligned}$$

and

$$\text{GP-ELBO} = \log \mathcal{N}(\mathbf{y}; m(\mathbf{X}), \mathbf{S} + \mathbf{K}_{\mathbf{X},\mathbf{Z}}\mathbf{K}_{\mathbf{Z},\mathbf{Z}}^{-1}\mathbf{K}_{\mathbf{Z},\mathbf{X}}) - \frac{1}{2}\text{Tr}(\mathbf{B}\mathbf{S}^{-1}). \quad (\text{S1})$$

A.2 Numerical implementation of the GP-ELBO

In this section, we derive formulae for efficient and numerically stable computation of the GP-ELBO [Matthews et al., 2017] in the heteroskedastic case. We first define $\mathbf{Q}_{\mathbf{X},\mathbf{X}} \equiv \mathbf{K}_{\mathbf{X},\mathbf{Z}}\mathbf{K}_{\mathbf{Z},\mathbf{Z}}^{-1}\mathbf{K}_{\mathbf{Z},\mathbf{X}}$. Then, Eq. S1 can be written as:

$$\text{GP-ELBO} = \log \mathcal{N}(\mathbf{y}; m(\mathbf{X}), \mathbf{Q}_{\mathbf{X},\mathbf{X}} + \mathbf{S}) - \frac{1}{2}\text{Tr}((\mathbf{K}_{\mathbf{X},\mathbf{X}} - \mathbf{Q}_{\mathbf{X},\mathbf{X}})\mathbf{S}^{-1}).$$

To obtain an efficient and stable evaluation of the GP-ELBO, we apply the Woodbury identity to the effective covariance matrix:

$$[\mathbf{Q}_{\mathbf{X},\mathbf{X}} + \mathbf{S}]^{-1} = \mathbf{S}^{-1} - \mathbf{S}^{-1}\mathbf{K}_{\mathbf{X},\mathbf{Z}}[\mathbf{K}_{\mathbf{Z},\mathbf{Z}} + \mathbf{K}_{\mathbf{Z},\mathbf{X}}\mathbf{S}^{-1}\mathbf{K}_{\mathbf{X},\mathbf{Z}}]^{-1}\mathbf{K}_{\mathbf{Z},\mathbf{X}}\mathbf{S}^{-1}.$$

To obtain a better conditioned matrix for inversion, we introduce in the previous formula the matrix \mathbf{L} , the Cholesky decomposition of $\mathbf{K}_{\mathbf{Z},\mathbf{Z}}$, *i.e.*, $\mathbf{L}\mathbf{L}^\top = \mathbf{K}_{\mathbf{Z},\mathbf{Z}}$:

$$\begin{aligned}[\mathbf{Q}_{\mathbf{X},\mathbf{X}} + \mathbf{S}]^{-1} &= \mathbf{S}^{-1} - \mathbf{S}^{-1}\mathbf{K}_{\mathbf{X},\mathbf{Z}}\mathbf{L}^{-\top}\mathbf{L}^\top[\mathbf{K}_{\mathbf{Z},\mathbf{Z}} + \mathbf{K}_{\mathbf{Z},\mathbf{X}}\mathbf{S}^{-1}\mathbf{K}_{\mathbf{X},\mathbf{Z}}]^{-1}\mathbf{L}\mathbf{L}^{-1}\mathbf{K}_{\mathbf{Z},\mathbf{X}}\mathbf{S}^{-1} \\ &= \mathbf{S}^{-1} - \mathbf{S}^{-1}\mathbf{K}_{\mathbf{X},\mathbf{Z}}\mathbf{L}^{-\top}[\mathbf{L}^{-1}(\mathbf{K}_{\mathbf{Z},\mathbf{Z}} + \mathbf{K}_{\mathbf{Z},\mathbf{X}}\mathbf{S}^{-1}\mathbf{K}_{\mathbf{X},\mathbf{Z}})\mathbf{L}^{-\top}]^{-1}\mathbf{L}^{-1}\mathbf{K}_{\mathbf{Z},\mathbf{X}}\mathbf{S}^{-1} \\ &= \mathbf{S}^{-1} - \mathbf{S}^{-1}\mathbf{K}_{\mathbf{X},\mathbf{Z}}\mathbf{L}^{-\top}[(\mathbf{I} + \mathbf{L}^{-1}(\mathbf{K}_{\mathbf{Z},\mathbf{X}}\mathbf{S}^{-1}\mathbf{K}_{\mathbf{X},\mathbf{Z}})\mathbf{L}^{-\top})^{-1}\mathbf{L}^{-1}\mathbf{K}_{\mathbf{Z},\mathbf{X}}\mathbf{S}^{-1}].\end{aligned}$$

For notational convenience, we define $\mathbf{U} \equiv \mathbf{L}^{-1}\mathbf{K}_{\mathbf{Z},\mathbf{X}}\mathbf{S}^{-\frac{1}{2}}$, and $\mathbf{V} \equiv [\mathbf{I} + \mathbf{U}\mathbf{U}^\top]$:

$$[\mathbf{Q}_{\mathbf{X},\mathbf{X}} + \mathbf{S}]^{-1} = \mathbf{S}^{-1} - \mathbf{S}^{-\frac{1}{2}}\mathbf{U}^\top\mathbf{V}^{-1}\mathbf{U}\mathbf{S}^{-\frac{1}{2}}.$$

By the matrix determinant lemma, we have:

$$\begin{aligned} |\mathbf{Q}_{\mathbf{X},\mathbf{X}} + \mathbf{S}| &= |\mathbf{K}_{\mathbf{Z},\mathbf{Z}} + \mathbf{K}_{\mathbf{Z},\mathbf{X}}\mathbf{S}^{-1}\mathbf{K}_{\mathbf{X},\mathbf{Z}}| |\mathbf{K}_{\mathbf{Z},\mathbf{Z}}^{-1}| |\mathbf{S}| \\ &= |\mathbf{L}\mathbf{L}^\top + \mathbf{K}_{\mathbf{Z},\mathbf{X}}\mathbf{S}^{-1}\mathbf{K}_{\mathbf{X},\mathbf{Z}}| |\mathbf{L}^{-\top}| |\mathbf{L}^{-1}| |\mathbf{S}| \\ &= |\mathbf{I} + \mathbf{L}^{-1}\mathbf{K}_{\mathbf{Z},\mathbf{X}}\mathbf{S}^{-1}\mathbf{K}_{\mathbf{X},\mathbf{Z}}\mathbf{L}^{-\top}| |\mathbf{S}| \\ &= |\mathbf{V}| |\mathbf{S}|. \end{aligned}$$

With these two definitions, the GP-ELBO can be written as:

$$\begin{aligned} \mathcal{L} &= \log \mathcal{N}(\mathbf{y}; m(\mathbf{X}), \mathbf{Q}_{\mathbf{X},\mathbf{X}} + \mathbf{S}) - \frac{1}{2} \text{Tr}((\mathbf{K}_{\mathbf{X},\mathbf{X}} - \mathbf{Q}_{\mathbf{X},\mathbf{X}})\mathbf{S}^{-1}) \\ &= -\frac{N}{2} \log 2\pi - \frac{1}{2} \log |\mathbf{Q}_{\mathbf{X},\mathbf{X}} + \mathbf{S}| - \frac{1}{2} \bar{\mathbf{y}}^\top [\mathbf{Q}_{\mathbf{X},\mathbf{X}} + \mathbf{S}]^{-1} \bar{\mathbf{y}} \\ &\quad - \frac{1}{2} \text{Tr}((\mathbf{K}_{\mathbf{X},\mathbf{X}} - \mathbf{Q}_{\mathbf{X},\mathbf{X}})\mathbf{S}^{-1}) \\ &= -\frac{N}{2} \log 2\pi - \frac{1}{2} \log |\mathbf{V}| |\mathbf{S}| - \frac{1}{2} \bar{\mathbf{y}}^\top (\mathbf{S}^{-1} - \mathbf{S}^{-\frac{1}{2}}\mathbf{U}^\top\mathbf{V}^{-1}\mathbf{U}\mathbf{S}^{-\frac{1}{2}}) \bar{\mathbf{y}} \\ &\quad - \frac{1}{2} \text{Tr}((\mathbf{K}_{\mathbf{X},\mathbf{X}} - \mathbf{Q}_{\mathbf{X},\mathbf{X}})\mathbf{S}^{-1}) \\ &= -\frac{N}{2} \log 2\pi - \frac{1}{2} \log |\mathbf{V}| - \frac{1}{2} \log |\mathbf{S}| - \frac{1}{2} \bar{\mathbf{y}}^\top \mathbf{S}^{-1} \bar{\mathbf{y}} - \frac{1}{2} c^\top c \\ &\quad - \frac{1}{2} \text{Tr}(\mathbf{K}_{\mathbf{X},\mathbf{X}}\mathbf{S}^{-1}) + \frac{1}{2} \text{Tr}(\mathbf{U}\mathbf{U}^\top), \end{aligned}$$

where $\bar{\mathbf{y}} \equiv \mathbf{y} - m(\mathbf{X})$ and we have defined $c \equiv \mathbf{L}_\mathbf{V}^{-1}\mathbf{U}\mathbf{S}^{-\frac{1}{2}}\bar{\mathbf{y}}$, with the Cholesky decomposition $\mathbf{L}_\mathbf{V}\mathbf{L}_\mathbf{V}^\top = \mathbf{V}$.

A.3 Predictive distribution of SGPR

In this section, we derive the predictive latent distribution of SGPR and its numerically stable implementation, given the variational GP posterior ψ , *i.e.*, $p(\mathbf{f}^*|\psi)$, from a sparse GP with heteroskedastic observation noise. From Section A.1, the optimal variational distribution \tilde{p} on \mathbf{u} writes:

$$\tilde{p}(\mathbf{u}) = \mathcal{N}(\mathbf{u} \mid \mathbf{m}_\mathbf{u}, \mathbf{R}_{\mathbf{uu}}),$$

with:

$$\begin{aligned} \mathbf{R}_{\mathbf{uu}} &= \mathbf{K}_{\mathbf{Z},\mathbf{Z}}(\mathbf{K}_{\mathbf{Z},\mathbf{X}}\mathbf{S}^{-1}\mathbf{K}_{\mathbf{X},\mathbf{Z}} + \mathbf{K}_{\mathbf{Z},\mathbf{Z}})^{-1}\mathbf{K}_{\mathbf{Z},\mathbf{Z}} \\ \mathbf{R}_{\mathbf{uu}}^{-1} &= \mathbf{K}_{\mathbf{Z},\mathbf{Z}}^{-1} + \mathbf{K}_{\mathbf{Z},\mathbf{Z}}^{-1}\mathbf{K}_{\mathbf{Z},\mathbf{X}}\mathbf{S}^{-1}\mathbf{K}_{\mathbf{X},\mathbf{Z}}\mathbf{K}_{\mathbf{Z},\mathbf{Z}}^{-1} \\ \mathbf{m}_\mathbf{u} &= \mathbf{R}_{\mathbf{uu}}\mathbf{K}_{\mathbf{Z},\mathbf{Z}}^{-1}[\mathbf{K}_{\mathbf{Z},\mathbf{X}}\mathbf{S}^{-1}(\mathbf{y} - m(\mathbf{X})) + \mathbf{K}_{\mathbf{X},\mathbf{Z}}\mathbf{K}_{\mathbf{Z},\mathbf{Z}}^{-1}m(\mathbf{Z})] + m(\mathbf{Z}). \end{aligned}$$

The predictive distribution at \mathbf{x}^* is:

$$p(\mathbf{f}^*|\psi) = \int p(\mathbf{f}^* \mid \mathbf{u})\tilde{p}(\mathbf{u})d\mathbf{u},$$

with:

$$p(\mathbf{f}^* | \mathbf{u}) = \mathcal{N}(\mathbf{f}^* | m(\mathbf{x}^*) + \mathbf{K}_{*\mathbf{Z}}\mathbf{K}_{\mathbf{Z},\mathbf{Z}}^{-1}(\mathbf{u} - m(\mathbf{Z})), \mathbf{K}_{**} - \mathbf{K}_{*\mathbf{Z}}\mathbf{K}_{\mathbf{Z},\mathbf{Z}}^{-1}\mathbf{K}_{\mathbf{Z}*});$$

therefore:

$$p(\mathbf{f}^* | \psi) = \mathcal{N}(\mathbf{f}^* | m(\mathbf{x}^*) - \mathbf{K}_{*\mathbf{Z}}\mathbf{K}_{\mathbf{Z},\mathbf{Z}}^{-1}m(\mathbf{Z}) + \mathbf{K}_{*\mathbf{Z}}\mathbf{K}_{\mathbf{Z},\mathbf{Z}}^{-1}\mathbf{m}_{\mathbf{u}}, \\ \mathbf{K}_{**} - \mathbf{K}_{*\mathbf{Z}}\mathbf{K}_{\mathbf{Z},\mathbf{Z}}^{-1}\mathbf{K}_{\mathbf{Z}*} + \mathbf{K}_{*\mathbf{Z}}\mathbf{K}_{\mathbf{Z},\mathbf{Z}}^{-1}\mathbf{R}_{\mathbf{u}\mathbf{u}}\mathbf{K}_{\mathbf{Z},\mathbf{Z}}^{-1}\mathbf{K}_{\mathbf{Z}*}).$$

For the numerical implementation, we define the same notations as in Section A.2: $\mathbf{L}\mathbf{L}^\top = \mathbf{K}_{\mathbf{Z},\mathbf{Z}}$, $\mathbf{U} \equiv \mathbf{L}^{-1}\mathbf{K}_{\mathbf{Z},\mathbf{X}}\mathbf{S}^{-\frac{1}{2}}$, $\mathbf{V} \equiv [\mathbf{I} + \mathbf{U}\mathbf{U}^\top]$, and $\mathbf{c} \equiv \mathbf{L}_{\mathbf{V}}^{-1}\mathbf{U}\mathbf{S}^{-\frac{1}{2}}(\mathbf{y} - m(\mathbf{X}))$, with the Cholesky decomposition $\mathbf{L}_{\mathbf{V}}\mathbf{L}_{\mathbf{V}}^\top = \mathbf{V}$. This leads to:

$$\mathbf{K}_{\mathbf{Z},\mathbf{Z}}^{-1}\mathbf{R}_{\mathbf{u}\mathbf{u}}\mathbf{K}_{\mathbf{Z},\mathbf{Z}}^{-1} = \mathbf{L}^{-\top}\mathbf{V}^{-1}\mathbf{L}^{-1},$$

and further:

$$\mathbf{K}_{\mathbf{Z},\mathbf{Z}}^{-1}\mathbf{m}_{\mathbf{u}} = \mathbf{L}^{-\top}\mathbf{L}_{\mathbf{V}}^{-\top}\mathbf{c} + \mathbf{L}^{-\top}\mathbf{L}_{\mathbf{V}}^{-\top}\mathbf{L}_{\mathbf{V}}^{-1}\mathbf{U}\mathbf{U}^\top\mathbf{L}^{-1}m(\mathbf{Z}) + \mathbf{L}^{-\top}\mathbf{L}_{\mathbf{V}}^{-\top}\mathbf{L}_{\mathbf{V}}^{-1}\mathbf{L}^{-1}m(\mathbf{Z}).$$

Finally, we obtain:

$$p(\mathbf{f}^* | \psi) = \mathcal{N}(\mathbf{f}^* | m(\mathbf{x}^*) + \mathbf{K}_{*\mathbf{Z}}(\mathbf{L}^{-\top}\mathbf{L}_{\mathbf{V}}^{-\top}\mathbf{c} + \mathbf{L}^{-\top}\mathbf{L}_{\mathbf{V}}^{-\top}\mathbf{L}_{\mathbf{V}}^{-1}\mathbf{U}\mathbf{U}^\top\mathbf{L}^{-1}m(\mathbf{Z}) + \\ \mathbf{L}^{-\top}\mathbf{L}_{\mathbf{V}}^{-\top}\mathbf{L}_{\mathbf{V}}^{-1}\mathbf{L}^{-1}m(\mathbf{Z}) - \mathbf{L}^{-\top}\mathbf{L}^{-1}m(\mathbf{Z})), \\ \mathbf{K}_{**} - \mathbf{K}_{*\mathbf{Z}}\mathbf{L}^{-\top}(\mathbf{I} - \mathbf{V}^{-1})\mathbf{L}^{-1}\mathbf{K}_{\mathbf{Z}*}).$$

Sanity check with $\mathbf{Z} = \mathbf{X}$. If $\mathbf{Z} = \mathbf{X}$, *i.e.*, all training points are selected as inducing points, the SGPR posterior should be exactly the same as the exact GP posterior. In this case, by substituting $\mathbf{K}_{\mathbf{Z},\mathbf{Z}}$ with $\mathbf{K}_{\mathbf{X},\mathbf{X}}$, the mean and covariance matrix of $\tilde{p}(\mathbf{u})$ become:

$$\mathbf{m}_{\mathbf{u}} = \mathbf{R}_{\mathbf{u}\mathbf{u}}^{-1}(\mathbf{S}^{-1}\mathbf{y} + \mathbf{K}_{\mathbf{X},\mathbf{X}}^{-1}m(\mathbf{X})) = \mathbf{K}_{\mathbf{X},\mathbf{X}}(\mathbf{K}_{\mathbf{X},\mathbf{X}} + \mathbf{S})^{-1}(\mathbf{y} - m(\mathbf{X})) + m(\mathbf{X}) \\ \mathbf{R}_{\mathbf{u}\mathbf{u}} = (\mathbf{K}_{\mathbf{X},\mathbf{X}}^{-1} + \mathbf{S}^{-1})^{-1} = \mathbf{K}_{\mathbf{X},\mathbf{X}} - \mathbf{K}_{\mathbf{X},\mathbf{X}}(\mathbf{K}_{\mathbf{X},\mathbf{X}} + \mathbf{S})^{-1}\mathbf{K}_{\mathbf{X},\mathbf{X}},$$

which matches the predictive distribution of the exact GP at \mathbf{X} .

Derivations and numerical implementations for SGPR in the homoskedastic and heteroskedastic cases, as stated in Section A.2 and A.3, are also considered and discussed in some other work [Matthews et al., 2017, Maddox et al., 2021] but differ slightly in the details.

A.4 Sparse Bayesian quadrature

To compute the variational posterior of VSBQ, we need to compute integrals of Gaussian distributions against the SGPR posterior with heteroskedastic noise. We provide here analytical formulae for this purpose. The following formulae are written in the zero-mean case; the non-zero mean case can be straightforwardly derived from this one (*i.e.*, by considering $f - m$). We follow Ghahramani and Rasmussen [2002a]. Here, we denote with Σ_ℓ the diagonal matrix of the parameters in the covariance kernel and with σ_f the output scale, so that $\kappa(\mathbf{x}, \mathbf{x}') = \sigma_f^2\Lambda\mathcal{N}(\mathbf{x}; \mathbf{x}', \Sigma_\ell)$, with $\Lambda \equiv \sqrt{(2\pi)^D}|\Sigma_\ell|$.¹

¹This formulation of the squared exponential kernel is equivalent to the main paper, but makes it easier to apply Gaussian identities.

We are interested in Bayesian quadrature formulae for the sparse GP integrated over Gaussian distributions of the form $\mathcal{N}(\cdot; \boldsymbol{\mu}_j, \boldsymbol{\Sigma}_j)$, for $1 \leq j \leq K$. The integrals of interest are Gaussian random variables which depend on the sparse GP and take the form:

$$\mathcal{I}_j[\mathbf{u}] = \int \mathcal{N}(\tilde{\mathbf{x}}; \boldsymbol{\mu}_j, \boldsymbol{\Sigma}_j) f(\tilde{\mathbf{x}} | \mathbf{u}) d\tilde{\mathbf{x}}.$$

Denoting with $\psi(\mathbf{u})$ the optimal variational distribution of \mathbf{u} in SGPR, the posterior mean of each integral is:

$$\begin{aligned} \mathbb{E}[\mathcal{I}_j] &= \int \mathcal{N}(\tilde{\mathbf{x}}; \boldsymbol{\mu}_j, \boldsymbol{\Sigma}_j) f(\tilde{\mathbf{x}} | \mathbf{u}) \psi(\mathbf{u}) d\tilde{\mathbf{x}} d\mathbf{u} \\ &= \int \mathcal{N}(\tilde{\mathbf{x}}; \boldsymbol{\mu}_j, \boldsymbol{\Sigma}_j) \mu_\psi(\tilde{\mathbf{x}}) d\tilde{\mathbf{x}}, \\ &= \int \mathcal{N}(\tilde{\mathbf{x}}; \boldsymbol{\mu}_j, \boldsymbol{\Sigma}_j) \kappa(\tilde{\mathbf{x}}, \mathbf{Z}) \boldsymbol{\Sigma} \mathbf{K}_{\mathbf{Z}, \mathbf{X}} \mathbf{S}^{-1} \mathbf{y} d\tilde{\mathbf{x}} \\ &= \mathbf{w}_j^T [\boldsymbol{\Sigma} \mathbf{K}_{\mathbf{Z}, \mathbf{X}} \mathbf{S}^{-1}] \mathbf{y}, \end{aligned}$$

where $(\mathbf{w}_j)_p \equiv \sigma_f^2 \Lambda \mathcal{N}(\boldsymbol{\mu}_j; \mathbf{z}_p, \boldsymbol{\Sigma}_j + \boldsymbol{\Sigma}_\ell)$. We compute then the posterior covariance between integrals \mathcal{I}_j and \mathcal{I}_k ,

$$\begin{aligned} \text{Cov}(\mathcal{I}_j, \mathcal{I}_k) &= \int \int \mathcal{N}(\tilde{\mathbf{x}}; \boldsymbol{\mu}_j, \boldsymbol{\Sigma}_j) \mathcal{N}(\tilde{\mathbf{x}}'; \boldsymbol{\mu}_k, \boldsymbol{\Sigma}_k) \text{Cov}(f(\tilde{\mathbf{x}}), f(\tilde{\mathbf{x}}')) d\tilde{\mathbf{x}} d\tilde{\mathbf{x}}' \\ &= \int \int \mathcal{N}(\tilde{\mathbf{x}}; \boldsymbol{\mu}_j, \boldsymbol{\Sigma}_j) \mathcal{N}(\tilde{\mathbf{x}}'; \boldsymbol{\mu}_k, \boldsymbol{\Sigma}_k) \kappa_\psi(\tilde{\mathbf{x}}, \tilde{\mathbf{x}}') d\tilde{\mathbf{x}} d\tilde{\mathbf{x}}' \\ &= \int \int \sigma_f^2 \Lambda \mathcal{N}(\tilde{\mathbf{x}}; \tilde{\mathbf{x}}', \boldsymbol{\Sigma}_\ell) \mathcal{N}(\tilde{\mathbf{x}}'; \boldsymbol{\mu}_j, \boldsymbol{\Sigma}_j) \mathcal{N}(\tilde{\mathbf{x}}; \boldsymbol{\mu}_k, \boldsymbol{\Sigma}_k) d\tilde{\mathbf{x}} d\tilde{\mathbf{x}}' \\ &\quad - \int \int \mathcal{N}(\tilde{\mathbf{x}}'; \boldsymbol{\mu}_j, \boldsymbol{\Sigma}_j) \mathcal{N}(\tilde{\mathbf{x}}; \boldsymbol{\mu}_k, \boldsymbol{\Sigma}_k) \sigma_f^2 \Lambda \mathcal{N}(\tilde{\mathbf{x}}; \mathbf{Z}, \boldsymbol{\Sigma}_\ell) \\ &\quad \cdot [\mathbf{K}_{\mathbf{Z}, \mathbf{Z}}^{-1} - \boldsymbol{\Sigma}] \sigma_f^2 \Lambda \mathcal{N}(\tilde{\mathbf{x}}'; \mathbf{Z}, \boldsymbol{\Sigma}_\ell) d\tilde{\mathbf{x}} d\tilde{\mathbf{x}}' \\ &= \sigma_f^2 \Lambda \mathcal{N}(\boldsymbol{\mu}_j; \boldsymbol{\mu}_k, \boldsymbol{\Sigma}_\ell + \boldsymbol{\Sigma}_j + \boldsymbol{\Sigma}_k) - \mathbf{w}_j^T [\mathbf{K}_{\mathbf{Z}, \mathbf{Z}}^{-1} - \boldsymbol{\Sigma}] \mathbf{w}_k. \end{aligned}$$

B Proofs

In this section, we provide proofs for the lemmas in the main paper.

Lemma B.1 (Lemma 3.1). *Assume that $KL(p(\mathbf{f}, \mathbf{u} | \mathbf{y}) \| p(\mathbf{f}, \mathbf{u} | \boldsymbol{\psi})) \leq \gamma$. Then, for any $\ell > 0$ there exists K_ℓ such that, for any \mathbf{x}^* , $\|\mathbb{E}[f(\mathbf{x}^*)^\ell] - \mathbb{E}[f_e(\mathbf{x}^*)^\ell]\| < K_\ell \sqrt{\gamma/2}$. There also exists K_e such that, for any \mathbf{x}^* , $\|\mathbb{E}[\exp(f(\mathbf{x}^*))] - \mathbb{E}[\exp(f_e(\mathbf{x}^*))]\| < K_e \sqrt{\gamma/2}$.*

Proof of Lemma 3.1. For this lemma, we only need to study the predictive distribution at a single

point \mathbf{x}^* , with associated value $f^* \equiv f(\mathbf{x}^*)$.

$$\begin{aligned}
& \text{KL}(p(\mathbf{f}, \mathbf{u}, f^* | \mathbf{y}) \| p(\mathbf{f}, \mathbf{u}, f^* | \boldsymbol{\psi})) \\
&= \int p(\mathbf{f}, \mathbf{u}, f^* | \boldsymbol{\psi}) \log \left(\frac{p(\mathbf{f}, \mathbf{u}, f^* | \boldsymbol{\psi})}{p(\mathbf{f}, \mathbf{u}, f^* | \mathbf{y})} \right) d\mathbf{f} d\mathbf{u} df^* \\
&= \int p(f^*, \mathbf{f} | \mathbf{u}) \tilde{p}(\mathbf{u}) \log \left(\frac{p(\mathbf{f}, \mathbf{u}, f^* | \boldsymbol{\psi})}{p(\mathbf{f}, \mathbf{u}, f^* | \mathbf{y})} \right) d\mathbf{f} d\mathbf{u} df^* \\
&= \int p(f^*, \mathbf{f} | \mathbf{u}) \tilde{p}(\mathbf{u}) \log \left(\frac{p(\mathbf{y}) p(\mathbf{f}, f^* | \mathbf{u}) \tilde{p}(\mathbf{u})}{p(\mathbf{y} | \mathbf{f}) p(\mathbf{f}, f^* | \mathbf{u}) \tilde{p}(\mathbf{u})} \right) d\mathbf{f} d\mathbf{u} df^* \\
&= \int p(\mathbf{f} | \mathbf{u}) \tilde{p}(\mathbf{u}) \log \left(\frac{p(\mathbf{y}) p(\mathbf{f} | \mathbf{u}) \tilde{p}(\mathbf{u})}{p(\mathbf{y} | \mathbf{f}) p(\mathbf{f} | \mathbf{u}) \tilde{p}(\mathbf{u})} \right) d\mathbf{f} d\mathbf{u} \\
&= \text{KL}(p(\mathbf{f}, \mathbf{u} | \mathbf{y}) \| p(\mathbf{f}, \mathbf{u} | \boldsymbol{\psi})).
\end{aligned}$$

By Pinsker inequality [Tsybakov, 2003], we know that:

$$\|p(\mathbf{f}, \mathbf{u}, f^* | \mathbf{y}) - p(\mathbf{f}, \mathbf{u}, f^* | \boldsymbol{\psi})\|_{TV} \leq \sqrt{\text{KL}(p(\mathbf{f}, \mathbf{u}, f^* | \mathbf{y}) \| p(\mathbf{f}, \mathbf{u}, f^* | \boldsymbol{\psi})) / 2} < \sqrt{\gamma/2},$$

using one of the assumptions of the Lemma. We further have that

$$\|p(f^* | \mathbf{y}) - p(f^* | \boldsymbol{\psi})\|_{TV} \leq \|p(\mathbf{f}, \mathbf{u}, f^* | \mathbf{y}) - p(\mathbf{f}, \mathbf{u}, f^* | \boldsymbol{\psi})\|_{TV},$$

as a coupling of the joint distribution is a coupling of the marginal distributions, and by definition, the total variation distance is $\|\pi_a - \pi_b\|_{TV} = \inf_{\omega \in \Omega(\pi_a, \pi_b)} P_\omega(X \neq Y)$, where $(X, Y) \sim \omega$ and $\Omega(\pi_a, \pi_b)$ is the set of all the couplings between π_a and π_b .

To find the inequalities of the Lemma, we will first show that:

$$\left\| \int f^{*\ell} (p(f^* | \mathbf{y}) - p(f^* | \boldsymbol{\psi})) df^* \right\| \leq K_\ell \sqrt{\gamma/2}. \quad (\text{S2})$$

As both $p(\cdot | \boldsymbol{\psi})$ and $p(\cdot | \mathbf{y})$ are normal, there exists $A \subset \mathbb{R}$ compact such that $\int_{\mathbb{R} \setminus A} f^\ell (p(f^* | \mathbf{y}) - p(f^* | \boldsymbol{\psi})) df^* \leq K_\ell'' \sqrt{\gamma/2}$ for $K_\ell'' > 0$ small enough. We can then study on A the integral, using the fact that the total variation distance is the L_1 norm and the fact that $x \mapsto x^\ell$ is continuous, and thus bounded by some K_ℓ' on A :

$$\begin{aligned}
\left\| \int f^{*\ell} (p(f^* | \mathbf{y}) - p(f^* | \boldsymbol{\psi})) df^* \right\| &\leq \left\| \int_{\mathbb{R} \setminus A} f^{*\ell} (p(f^* | \mathbf{y}) - p(f^* | \boldsymbol{\psi})) df^* \right\| \\
&\quad + \left\| \int_A f^{*\ell} (p(f^* | \mathbf{y}) - p(f^* | \boldsymbol{\psi})) df^* \right\| \\
&\leq K_\ell'' \sqrt{\gamma/2} + K_\ell' \int_A \|p(f^* | \mathbf{y}) - p(f^* | \boldsymbol{\psi})\| df^* \\
&\leq K_\ell'' \sqrt{\gamma/2} + K_\ell' \int_{\mathbb{R}} \|p(f^* | \mathbf{y}) - p(f^* | \boldsymbol{\psi})\| df^* \\
&\leq K_\ell'' \sqrt{\gamma/2} + K_\ell' \|p(f^* | \mathbf{y}) - p(f^* | \boldsymbol{\psi})\|_{TV} \\
&\leq K_\ell \sqrt{\gamma/2}
\end{aligned}$$

for $K_\ell = K_\ell'' + K_\ell'$, proving the first inequality of the Lemma.

The second inequality of the Lemma follows from an identical proof as above, except that in Eq. S2 we would use an exponential instead of the power function.² \square

Lemma B.2 (Lemma 3.2). *Let a and b be two functions associated with two distributions defined on \mathcal{X} , $\pi_a \propto \exp(a(\cdot))$ and $\pi_b \propto \exp(b(\cdot))$. If $\forall x$, $|a(x) - b(x)| < K$, then:*

$$\|\pi_a - \pi_b\|_{TV} \leq 1 - \exp(-K).$$

Proof of Lemma 3.2. By definition, $\|\pi_a - \pi_b\|_{TV} = \inf_{\omega \in \Omega(\pi_a, \pi_b)} P_\omega(X \neq Y)$, where $(X, Y) \sim \omega$ and $\Omega(\pi_a, \pi_b)$ is the set of all the couplings between π_a and π_b .

To find an upper bound on the TV distance it is sufficient to find a particular coupling ω such that $P_\omega(X \neq Y)$ is small enough. Here, we propose the following coupling for joint sampling of X and Y , derived from the rejection sampling algorithm. Note that $a \vee b$ is the maximum of a and b and $a \wedge b$ is the minimum:

- Sample $Z \in \mathbb{R}^{d+1}$ under the curve $\exp(a \vee b)$, i.e., $Z[1 : d] \sim \exp(a(\cdot) \vee b(\cdot))$ and $Z[d+1] \sim \mathcal{U}(0, \exp(a(Z[1 : d]) \vee b(Z[1 : d])))$;
- If $Z[d+1] < \exp(a)$ then $X = Z[1 : d]$, and if $Z[d+1] < \exp(b)$ then $Y = Z[1 : d]$.
- Otherwise, we have either $Z[d+1] > \exp(a)$ and $Z[d+1] < \exp(b)$ or the opposite, i.e., $Z[d+1] > \exp(b)$ and $Z[d+1] < \exp(a)$. If $Z[d+1] > \exp(a)$ (resp. b), then resample Z' under the curve $\exp(a \vee b)$ until $Z'[d+1] < \exp(a)$ (resp. b), then $X = Z'[1 : d]$ (resp. $Y = Z'[1 : d]$).
- Return (X, Y) .

Under this coupling $P_\gamma(X \neq Y) \leq P(Z[d+1] > \exp(b \wedge a))$. Which leads to the following bound, using that $a(x) \vee b(x) - a(x) \wedge b(x) \leq K$:

$$\begin{aligned} \|\pi_a - \pi_b\|_{TV} &\leq \frac{\int \exp(a(x) \vee b(x)) - \exp(a(x) \wedge b(x)) dx}{\int \exp(a(x) \vee b(x)) dx} \\ &= \frac{\int \exp(a(x) \vee b(x)) (1 - \exp(a(x) \wedge b(x) - a(x) \vee b(x))) dx}{\int \exp(a(x) \vee b(x)) dx} \\ &\leq \frac{\int \exp(a(x) \vee b(x)) (1 - \exp(-K)) dx}{\int \exp(a(x) \vee b(x)) dx} \\ &= 1 - \exp(-K), \end{aligned}$$

where we used that $a(x) \vee b(x) - a(x) \wedge b(x) = |a(x) - b(x)|$. \square

C Experiment details and additional results

C.1 Implementation details

In this section, we describe the implementation details of variational sparse Bayesian quadrature (VSBQ), including noise shaping, choice of hyperparameters, and variational inference details.

²An alternative derivation for these results would use uniform integrability and conclude that the distance between the parameters of the two normal distributions is controlled. We preferred to provide here a longer but more explicit proof.

Design principles for the noise shaping formula. We recall that noise shaping increases the total likelihood variance for observation $(\mathbf{x}_n, y_n, \sigma_{\text{obs}}(\mathbf{x}_n))$,

$$\sigma_{\text{tot}}^2(\mathbf{x}_n, y_n) = \sigma_{\text{obs}}^2(\mathbf{x}_n) + \sigma_{\text{shape}}^2(\Delta y_n),$$

where $\sigma_{\text{obs}}^2(\mathbf{x}_n)$ is the estimated measurement variance at \mathbf{x}_n , and $\Delta y_n \equiv y_{\text{max}} - y_n$, with y_{max} the maximum observed log-density. We design $\sigma_{\text{shape}}^2(\Delta y)$ according to the following principles:

- a. Noise shaping should be a monotonically increasing function of Δy (larger shaping noise for lower-density points);
- b. Below a threshold θ_σ , noise shaping should be ‘small’, up to a quantity σ_{med} (noise shaping should be small in high-density regions);
- c. Asymptotically, the noise shaping standard deviation should increase *linearly* in Δy , as any other functional form would make the noise shape contribution disappear (for sublinear functions) or dominate (superlinear) for extremely low values of the log-density.

Following these principles, we propose the form used in the main text (Eq. 21),

$$\sigma_{\text{shape}}(\Delta y) = \exp((1 - \rho) \log \sigma_{\text{min}} + \rho \log \sigma_{\text{med}}) + \mathbf{1}_{\Delta y \geq \theta_\sigma} \lambda_\sigma (\Delta y - \theta_\sigma),$$

where $\rho = \min(1, \Delta y / \theta_\sigma)$; θ_σ is a threshold for ‘very low density’ points, at which we start the linear increase; λ_σ is the slope of the increase; and σ_{min}^2 and σ_{med}^2 are two shape parameters. σ_{med} is the added noise at the low density threshold θ_σ .

Trimming and noise shaping hyperparameters. Both the trimming stage and noise shaping involve the selection of hyperparameters for what is considered a ‘low-density threshold’. The trimming stage consists of removing from the initial set points with log posterior density lower than the threshold η_{trim} , relative to the maximum observed value. Noise shaping begins to linearly increase the added shaping noise starting from the low-density threshold θ_σ .

As discussed by [Gammal et al. \[2022\]](#), we can set a reasonable threshold in D dimensions by considering a multivariate normal distribution in dimension D . The log density of a multivariate normal distribution is proportional to the sum of D independent standard 1D Gaussian random variables. By defining $\Delta_y = 2 [\max(\log p) - \log p]$, we have $\Delta_y \sim \chi_D^2$. Further, the threshold for a “ n - σ contour” [[Gammal et al., 2022](#)] is,

$$[\Delta_y](n) = F_D^{-1} \left[\text{erf}(n/\sqrt{2}) \right], \tag{S3}$$

where F_D is the χ^2 cumulative distribution function for D degrees of freedom. In other words, we choose as a ‘low-density’ threshold the density of a multivariate normal at n standard deviations from the center, for $n \gg 1$. In the experiments, we use $\eta_{\text{trim}} = [\Delta_y](20)$ and $\theta_\sigma = [\Delta_y](10)$. The values of η_{trim} and θ_σ are plotted in [Figure S1](#).

As for the confidence interval parameter β , we used 1.96 (the 97.5th percentile point of a normal distribution). For the other noise shaping hyperparameters, we used $\sigma_{\text{med}} = 1$, $\lambda_\sigma = 0.05$ throughout the experiments.

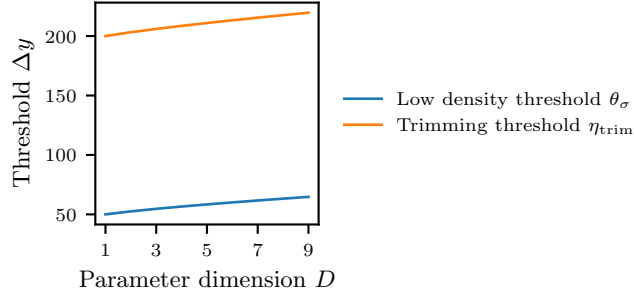


Figure S1: Log density threshold value versus the parameter dimension D .

Stochastic variational inference. The number of variational components K in VSBQ is 50, which is also the default maximum number of components in VBMC [Acerbi, 2018]. For initialization, we first perform K-means clustering on a subset of training points and initialize each component location $\boldsymbol{\mu}_k^{(i)}$ around the cluster centers, adding Gaussian noise with a standard deviation 10^{-6} , for $1 \leq k \leq K$. The initial scale of the component $\sigma_k \boldsymbol{\lambda}^{(i)}$ is set to 10^{-3} , for each dimension i , where $1 \leq i \leq D$. For the two moons bimodal problem, we set the number of clusters to 50, using the top 80% high-density points for K-means clustering. For all other problems, the number of clusters is set to 1, with K-means applied to the top 1% of high-density points – effectively computing the mean of the selected points.

As described in the main text, after fitting the sparse GP surrogate, variational inference is conducted by optimizing the surrogate ELBO with Bayesian quadrature. In addition, we impose a soft penalty loss during the ELBO optimization for bounding the variational parameters (means and scales of the mixture components), as done in Acerbi [2020], to help constrain the variational distribution in the local trust region of the surrogate. The lower and upper bounds are computed based on the training points \mathbf{X} . For each dimension i , let $\mathbf{X}_{\min}^{(i)}$ and $\mathbf{X}_{\max}^{(i)}$ denote the minimum and maximum value of this dimension. The lower bounds and upper bounds for the k^{th} component’s mean $\boldsymbol{\mu}_k^{(i)}$ and log scale $\log \sigma_k \boldsymbol{\lambda}^{(i)}$ are provided in Table S1.

Parameter	Description	Lower bound	Upper bound
$\boldsymbol{\mu}_k^{(i)}$	mixture component mean	$\mathbf{X}_{\min}^{(i)}$	$\mathbf{X}_{\max}^{(i)}$
$\log \sigma_k \boldsymbol{\lambda}^{(i)}$	mixture component scale	$\log \left[10^{-6} \left(\mathbf{X}_{\max}^{(i)} - \mathbf{X}_{\min}^{(i)} \right) \right]$	$\log \left(\mathbf{X}_{\max}^{(i)} - \mathbf{X}_{\min}^{(i)} \right)$

Table S1: The soft bounds for variation posterior parameters.

For both the mean and scale, the soft penalty loss can be written as,

$$\mathbf{1}_{\theta_k^{(i)} \leq \text{LB}(\theta_k^{(i)}) \text{ or } \theta_k^{(i)} \geq \text{UB}(\theta_k^{(i)})} \cdot \frac{1}{2} \left[\frac{\max \left(\theta_k^{(i)} - \text{LB}(\theta_k^{(i)}), \text{UB}(\theta_k^{(i)}) - \theta_k^{(i)} \right)}{\tau \left(\text{UB}(\theta_k^{(i)}) - \text{LB}(\theta_k^{(i)}) \right)} \right]^2, \quad (\text{S4})$$

where $\theta_k^{(i)}$ represents either the mean $\boldsymbol{\mu}_k^{(i)}$ or the log scale $\log \sigma_k \boldsymbol{\lambda}^{(i)}$, and $\tau = 0.01$. $\text{LB}(\theta_k^{(i)})$ and $\text{UB}(\theta_k^{(i)})$ denote the lower and upper bounds, respectively.

C.2 Further details of procedure and metrics

MAP estimation. To find the global mode, we launch multiple MAP optimization runs in parallel and independently, using different random seeds and initial starting points. Each MAP optimization run produces a trace of evaluated points. To meet the total evaluation budget of $3000D$ for the benchmark experiments, we sequentially add the optimization traces until the total number of evaluations exceeds the budget. The last trace is then truncated to ensure that the total number of evaluations precisely equals the budget. The entire MAP estimation procedure was repeated ten times for each problem, with different seeds, to yield ten different training datasets over which we computed statistics (see below).

Computing the metrics. For Δ LML, the true marginal likelihood is computed analytically, via numerical quadrature methods, or estimated from extensive MCMC sampling via Geyer’s reverse logistic regression [Geyer, 1994], depending on the structure of each specific problem. The estimated log marginal likelihood of VSBQ and NNR are taken as the ELBO computed in variational inference. For the Laplace method, the log normalization constant of the approximation can be computed analytically given the (numerically estimated) Hessian at the mode. We computed the posterior metrics (MMTV and GsKL) based on samples from the variational posteriors of VSBQ and NNR, samples from the Laplace approximation. The ground-truth posterior is represented by samples from well-tuned and extensive MCMC sampling.

Statistical analyses. We ran the VSBQ and NNR algorithm with ten different random seeds, also corresponding to ten different training datasets, and computed the triplet of metrics (Δ LML, MMTV, GsKL) for each run. We report the median and 95% confidence interval of the median obtained via bootstrap ($n_{\text{bootstrap}} = 10^4$). For the Laplace method, we report the estimate obtained by running numerical differentiation of the Hessian from the MAP estimate (the mode). The output of the Laplace approximation is deterministic given the global mode, so there is a single estimate per problem.

C.3 Black-box variational inference

For black-box variational inference, the score function estimator for the ELBO gradient can be written as:

$$\begin{aligned} \nabla_{\phi} \mathbb{E}_{\phi} \left[\log \frac{p(\mathcal{D}|\mathbf{x})p(\mathbf{x})}{q_{\phi}(\mathbf{x})} \right] &= \mathbb{E}_{\phi} [\nabla_{\phi} \log q_{\phi}(\mathbf{x}) (\log p(\mathcal{D}|\mathbf{x})p(\mathbf{x}) - \log q_{\phi}(\mathbf{x}))] \\ &= \mathbb{E}_{\phi} [\nabla_{\phi} \log q_{\phi}(\mathbf{x}) h_{\phi}(\mathbf{x})], \end{aligned} \tag{S5}$$

where $h_{\phi}(\mathbf{x}) = \log p(\mathcal{D}|\mathbf{x})p(\mathbf{x}) - \log q_{\phi}(\mathbf{x})$. As shown by Ranganath et al. [2014], there are two possible ways to reduce the variance of the score function estimator: the Rao-Blackwellization technique and control variates. The Rao-Blackwellization technique cannot be used since we only have access to the target density while the dependency structure of the black-box target model is assumed unknown. Conversely, we can use control variates. In particular, noting that for any constant b , $\mathbb{E}_{\phi}[b\nabla_{\phi} \log q_{\phi}] = 0$, $b\nabla_{\phi} \log q_{\phi}$ can be used as the control variate for reducing the stochastic gradient variance, i.e.,

$$\mathbb{E}_{\phi} [\nabla_{\phi} \log q_{\phi}(\mathbf{x}) h_{\phi}(\mathbf{x})] = \mathbb{E}_{\phi} [\nabla_{\phi} \log q_{\phi}(\mathbf{x}) (h_{\phi}(\mathbf{x}) - b)]. \tag{S6}$$

An optimal choice of b would require estimating the covariance between $\nabla_{\phi} \log q_{\phi}(\mathbf{x}) h_{\phi}(\mathbf{x})$ and $\nabla_{\phi} \log q_{\phi}$, and the variance of $\nabla_{\phi} \log q_{\phi}$, which would require extra evaluations on the target density

function. To simplify the implementation and comparison to other methods, we instead take an exponential moving average of $h_\phi(\mathbf{x})$ as the value of b , as suggested in the probabilistic programming framework Pyro [Bingham et al., 2018]. The smoothing factor for the exponential moving average is 0.9.

As stated in the main text, we allocate $10 \times 3000D$ target density evaluation budget for BBVI. Denoting the number of Monte Carlo samples for gradient estimation with $M_g \in \{1, 10, 100\}$, the total number of optimization iterations is then set to $\frac{10 \times 3000D}{M_g}$. For all variational distribution families—a Gaussian with *diagonal* covariance matrix, a Gaussian with *full-rank* covariance matrix, and a mixture of Gaussians with $K = 5$ and $K = 50$ components—the Gaussian distribution mean is initialized near the origin, by adding Gaussian noise with a standard deviation 10^{-6} and the scales are set to 10^{-3} .

C.4 Neural network regression

For neural network regression, we followed as closely as possible the same procedure as in VSBQ, while substituting the sparse GP surrogate with a deep neural network. This means that we used techniques such as a global mean function, noise shaping, and trimming (removal of very low-density points), exactly as done in VSBQ. Empirically, we found that noise shaping helps stabilize the training of the neural network by avoiding exploding gradients.

We report below the neural network setup as described in the main text, with additional implementation and training details.

Neural network details. For the neural network, we use a multilayer perceptron (MLP) with an input layer of dimension D , four hidden layers of 1024 units, an output layer for scalar prediction, and ReLU activation functions. The dataset is randomly split into training and validation sets, with a ratio of 4 : 1. In addition, we add a negative quadratic mean function to the neural network output to ensure integrability, the same as the (sparse) GP. Thus, the surrogate function g is:

$$g(\mathbf{x}; \mathbf{w}) = m_0 - \frac{1}{2} \sum_{i=1}^D \frac{(x_i - \mu_i)^2}{\omega_i^2} + \text{MLP}(\mathbf{x}),$$

where \mathbf{w} denotes the free parameters to optimize, including the parameters in the negative quadratic mean function and MLP parameters.

Loss. The loss is the average log-likelihood under the heteroskedastic noise model, which is equivalent to the mean squared error (MSE) weighted by the noise variance,

$$\mathcal{L}(\mathbf{w}) = \frac{1}{N} \sum_{n=1}^N \frac{(g(\mathbf{x}_n) - y_n)^2}{\sigma_{\text{tot}}^2(\mathbf{x}_n, y_n)},$$

where $\sigma_n^2 = \sigma_{\text{obs}}^2(\mathbf{x}_n) + \sigma_{\text{shape}}^2(\Delta y_n)$.

Optimization. We use AdamW [Loshchilov and Hutter, 2019] to optimize the parameters, with a learning rate of 0.001 and batch size of 32. The optimization is stopped when the loss on the validation set does not decrease for 20 epochs.

Weight decay. We optimize the neural network by trying three different values of weight decay hyperparameter $\alpha \in \{0, 0.01, 0.1\}$. The neural network with the lowest validation loss is used. Note that for adaptive gradient algorithms like AdamW, weight decay is different from L_2 regularization. Using weight decay for regularization is standard practice in modern neural network training [Loshchilov and Hutter, 2019, Zhang et al., 2019]. As per standard practice, we apply weight decay only to the MLP weights, excluding the biases and the trainable quadratic mean parameters.

Stochastic variational inference. After neural network fitting, we run stochastic variational inference via automatic differentiation (ADVI; Kucukelbir et al., 2017) to compute a tractable posterior approximation from the neural network surrogate. The variational distribution is the same as that used for VSBQ, *i.e.*, a mixture of $K = 50$ multivariate normal distributions. Unlike VSBQ where we can compute the expected log joint in the ELBO analytically, with a neural network surrogate, we have to estimate the value and gradient of the expected log joint. We use reparametrization tricks [Kingma and Welling, 2013] to get an unbiased estimate for the gradient of the expected log joint value. Apart from the difference in computing the expected log joint, all the other steps (optimization iterations, variational distribution initialization, etc.) stay the same as the variational inference part in VSBQ.

C.5 MAP estimates via Bayesian Adaptive Direct Search (BADS)

A popular choice for black-box optimization is Bayesian optimization (BO; Garnett, 2023). BO can also deal with noisy observations like CMA-ES and is known for its efficiency in finding the optimum. We therefore applied VSBQ to optimization traces obtained from a (hybrid) BO optimization method named Bayesian Adaptive Direct Search (BADS; Acerbi and Ma, 2017), a state-of-the-art BO optimization algorithm with wide application in computational neuroscience and other fields.

We provide the results for VSBQ with CMA-ES and BADS in Table S2, S3 and Figure S2, S3. From the tables and figures, we can see that the performance of VSBQ with BADS and CMA-ES is almost identical for three out of four benchmark problems (Two Moons, multivariate Rosenbrock-Gaussian, and Bayesian timing model). Instead, we found that VSBQ performs less effectively with traces from BADS in the multisensory causal inference model, compared to CMA-ES. Still, VSBQ (BADS) is comparable to the noiseless Laplace approximation (LAPLACE) even in the presence of large amounts of log-density evaluation noise.

We hypothesize that BADS can be a worse choice than CMA-ES for our purpose of post-process inference exactly for the reasons that make BADS a better optimization algorithm on these problems [Acerbi and Ma, 2017]. Specifically, an optimization algorithm that converges to the global optimum quickly and efficiently is not ideal for post-process inference, in that a more exploratory population-based algorithm, such as CMA-ES, provides better coverage and more information about the shape of the posterior landscape. For this reason, we recommend CMA-ES over BADS for the purpose of post-process inference. Future work could focus on developing an optimization algorithm that is good at both tasks, that is MAP estimation and subsequent posterior approximation.

Table S2: **Two Moons posterior** ($D = 2$). The method performance is measured using the metrics ΔLML , MMTV, and GsKL. For all metrics, lower values indicate better performance. We bold the best results based on the 95% confidence interval (CI) of the median. If there are overlaps between CIs, we bold all overlapping values.

	ΔLML (\downarrow)	MMTV (\downarrow)	GsKL (\downarrow)
VSQ (CMA-ES)	0.0017 [0.00057,0.0026]	0.020 [0.018,0.021]	8.5e-05 [4.4e-05,0.00019]
VSQ (BADS)	0.0010 [0.00041,0.0017]	0.020 [0.019,0.022]	0.00018 [0.00013,0.00020]

Table S3: **Multivariate Rosenbrock-Gaussian** ($D = 6$). See Table S2 for a detailed description of metrics and bolding criteria.

	ΔLML (\downarrow)	MMTV (\downarrow)	GsKL (\downarrow)
VSQ (CMA-ES)	0.20 [0.20,0.20]	0.037 [0.035,0.038]	0.018 [0.017,0.018]
VSQ (BADS)	0.19 [0.19,0.20]	0.038 [0.037,0.039]	0.018 [0.017,0.018]

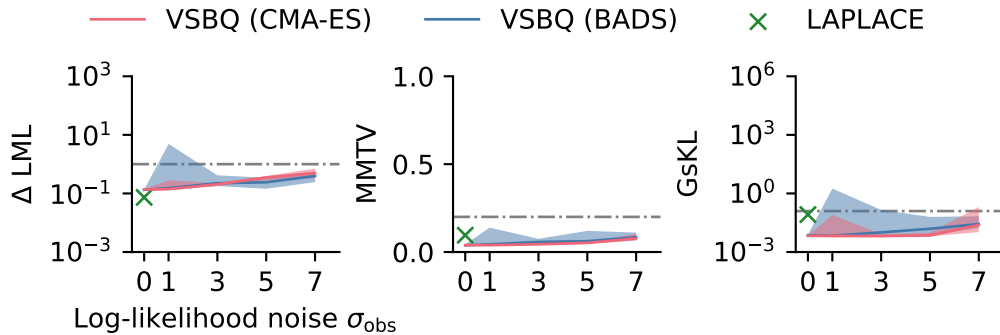


Figure S2: **Performance on Bayesian timing model with traces from different optimization algorithms.** Median ΔLML loss (left), MMTV (middle), and GsKL (right) as a function of the log-likelihood noise σ_{obs} for the Bayesian Timing model. Shaded areas are 95% CI of the median and grey dash-dotted horizontal lines are the rule-of-thumb thresholds for good performance ($\Delta\text{LML}=1$, $\text{MMTV}=0.2$, $\text{GsKL}=1/8$). The performance of VSBQ is virtually identical, regardless of the source of evaluations, whether CMA-ES or BADS.

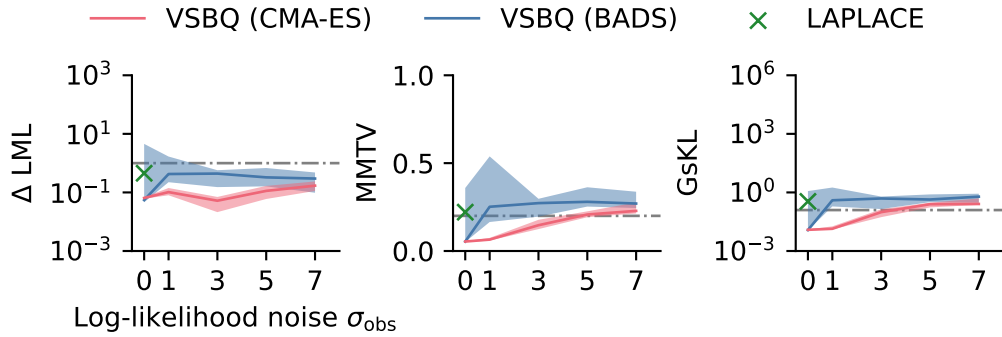
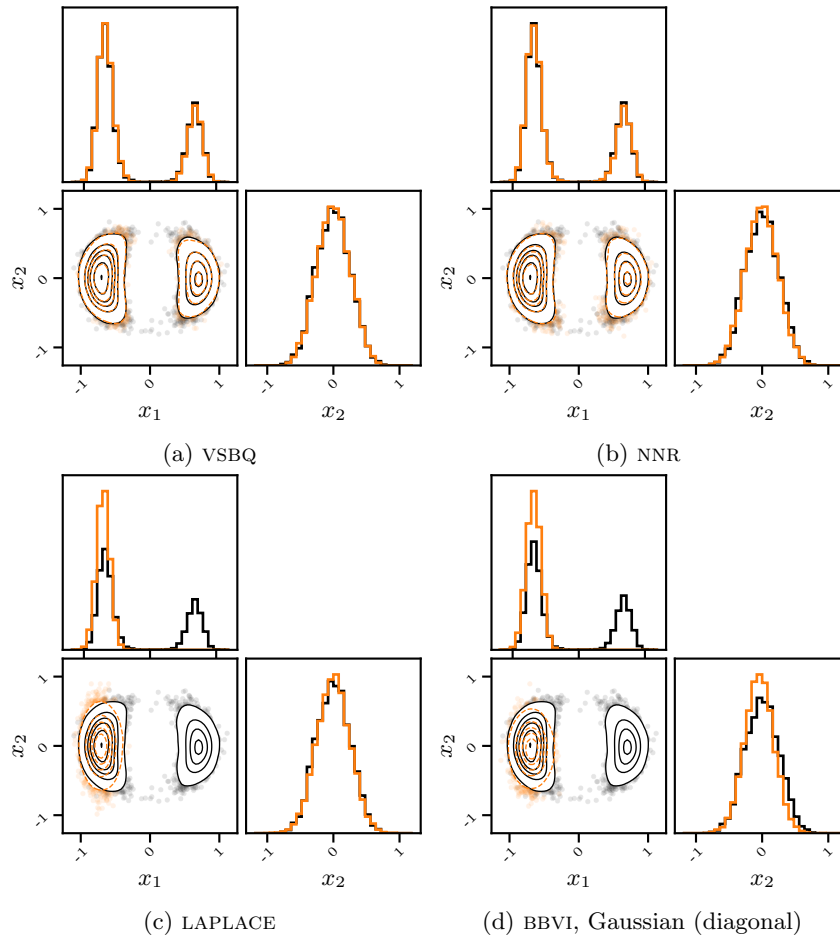


Figure S3: **Performance on multisensory causal inference model with traces from different optimization algorithms.** Median ΔLML loss (left), MMTV (middle), and GsKL (right) as a function of the log-likelihood noise σ_{obs} for the Bayesian Timing model. Shaded areas are 95% CI of the median and grey dash-dotted horizontal lines are the rule-of-thumb thresholds for good performance ($\Delta\text{LML}=1$, $\text{MMTV}=0.2$, $\text{GsKL}=1/8$). VSBQ with traces from BADs performs worse than VSBQ with CMA-ES, but still comparable to the (noiseless) LAPLACE.

C.6 Visualization of posteriors

We visualize posterior distributions as ‘corner plots’, *i.e.*, a plot with 1D and all pairwise 2D marginals. For visualization of individual posteriors obtained by the algorithms, for all problems, we report example solutions obtained from a run with the same random seed (see Figure S5, S6, S7, and S8).



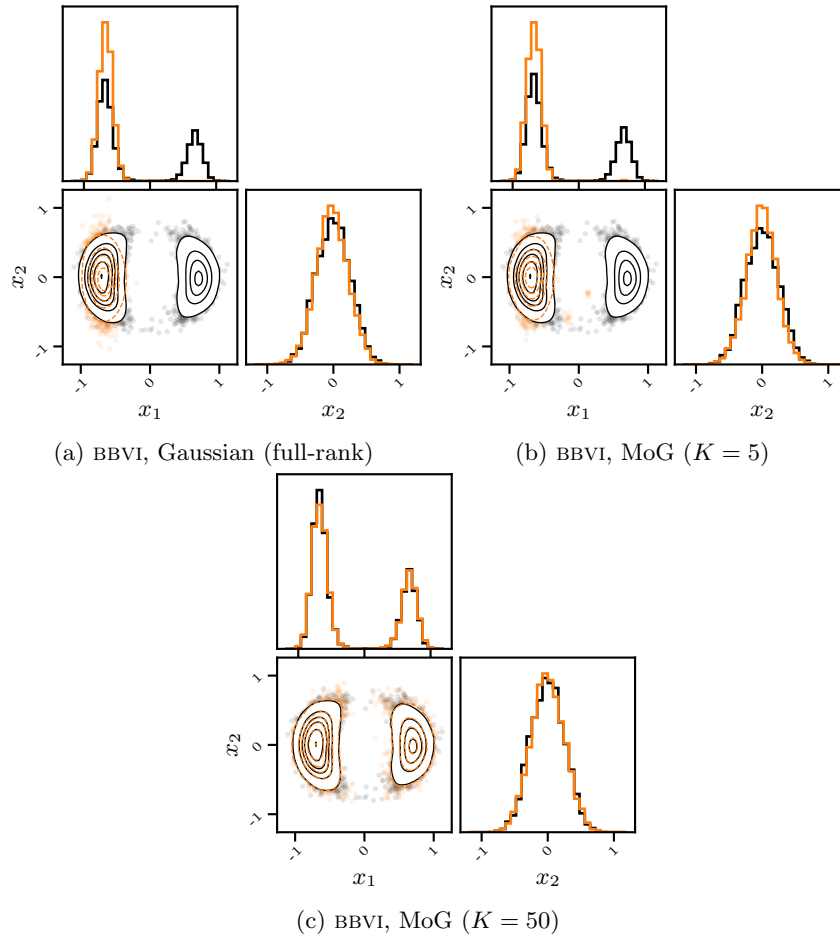
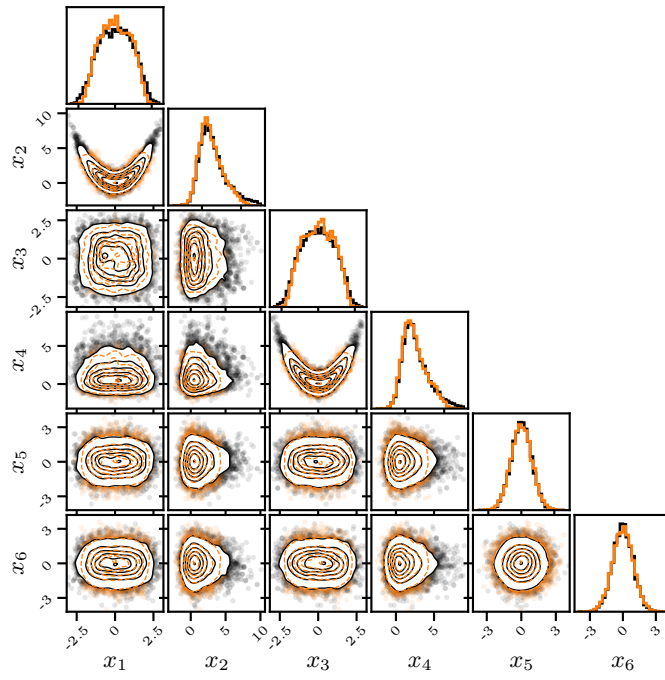
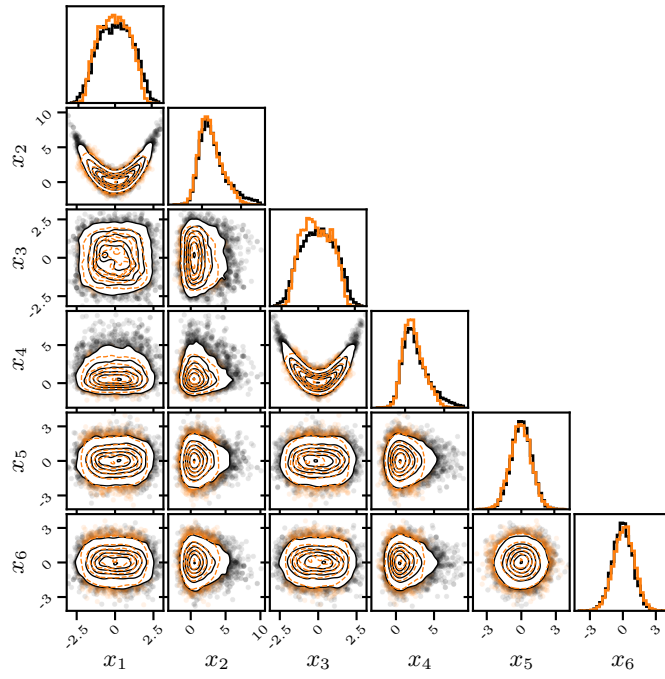


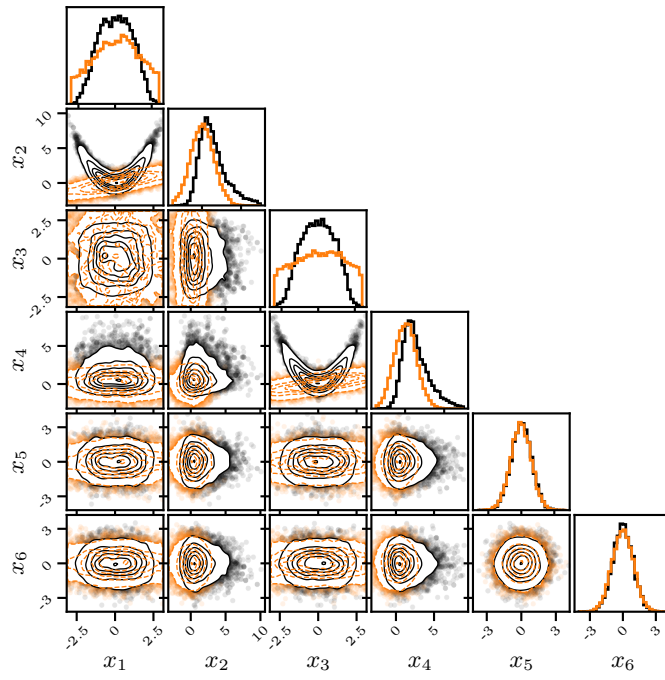
Figure S5: **Two Moons bimodal posterior visualization.** The orange density contours and points in the sub-figures represent the posterior samples from VSBQ, NNR, and LAPLACE, while the black contours and points denote ground truth samples. VSBQ and NNR perfectly capture the ground-truth bimodal posterior, while LAPLACE is limited to one mode. Among the BBVI methods, the MoG ($K=50$) configuration performs best.



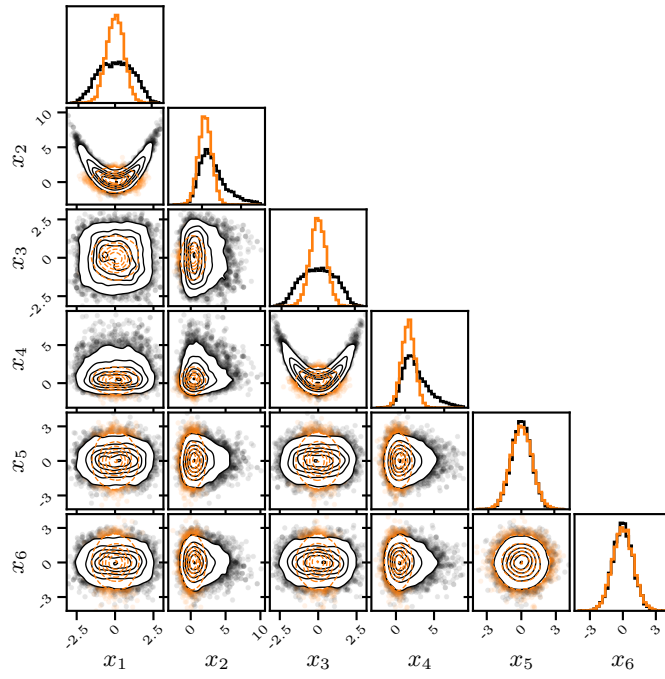
(a) VSBQ



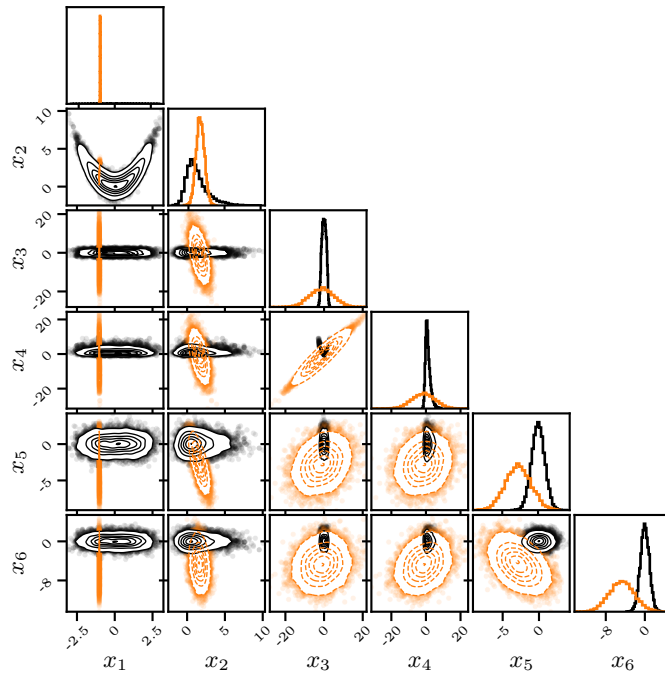
(b) NNR



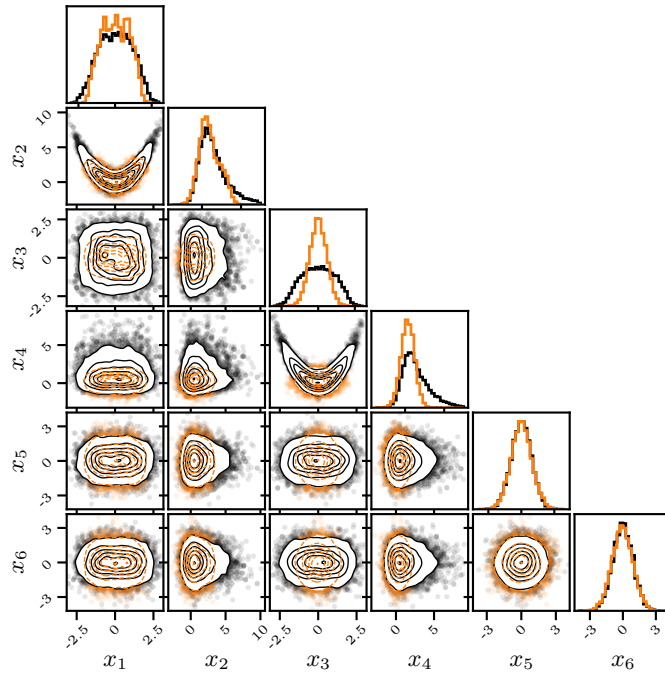
(c) LAPLACE



(d) BBVI, Gaussian (diagonal)



(e) BBVI, Gaussian (full-rank)



(f) BBVI, MoG ($K = 5$)

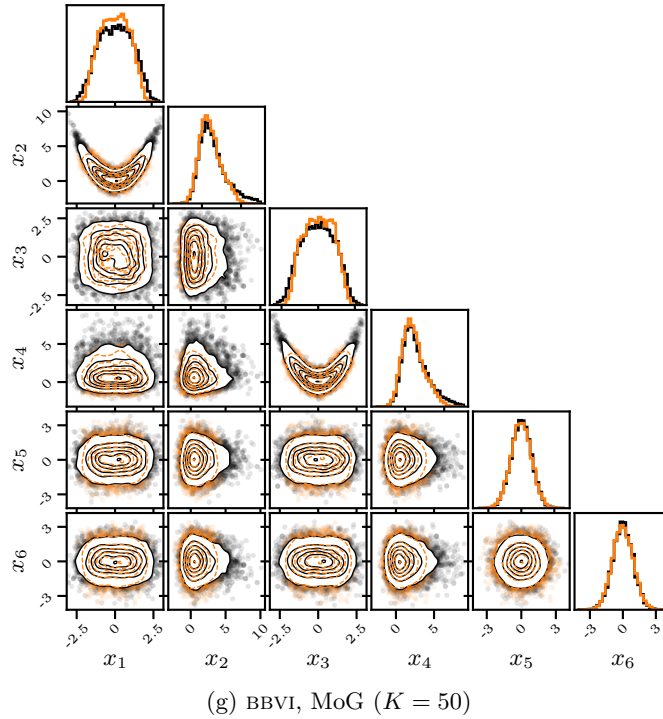
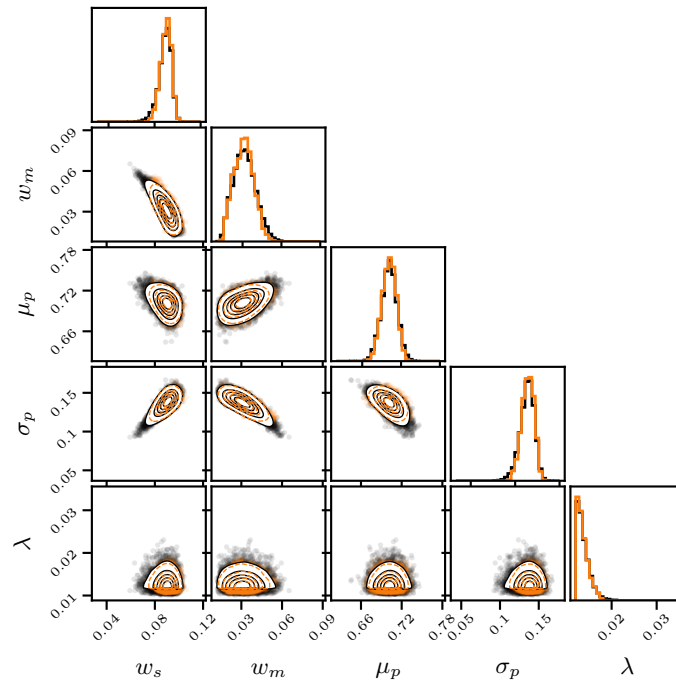
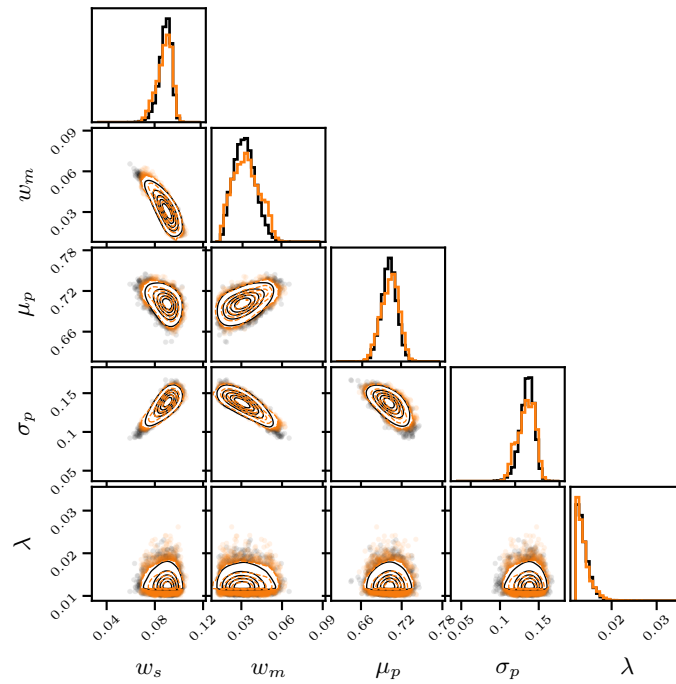


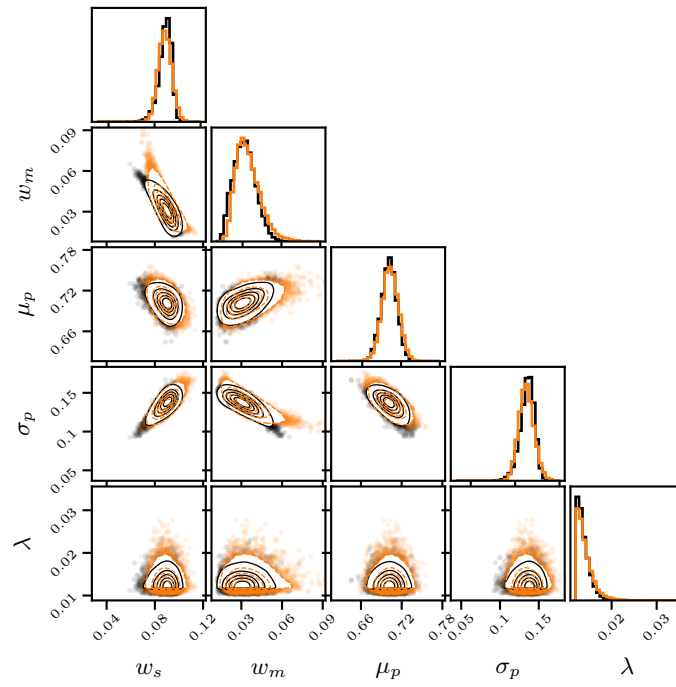
Figure S6: **Multivariate Rosenbrock-Gaussian posterior visualization.** The orange density contours and points in the sub-figures represent the posterior samples from VSBQ, NNR, and LAPLACE, while the black contours and points denote ground truth samples. Both VSBQ and NNR capture very well the complex shape of the distribution, while in this example LAPLACE fails. Among the BBVI methods, the MoG ($K=50$) configuration performs best.



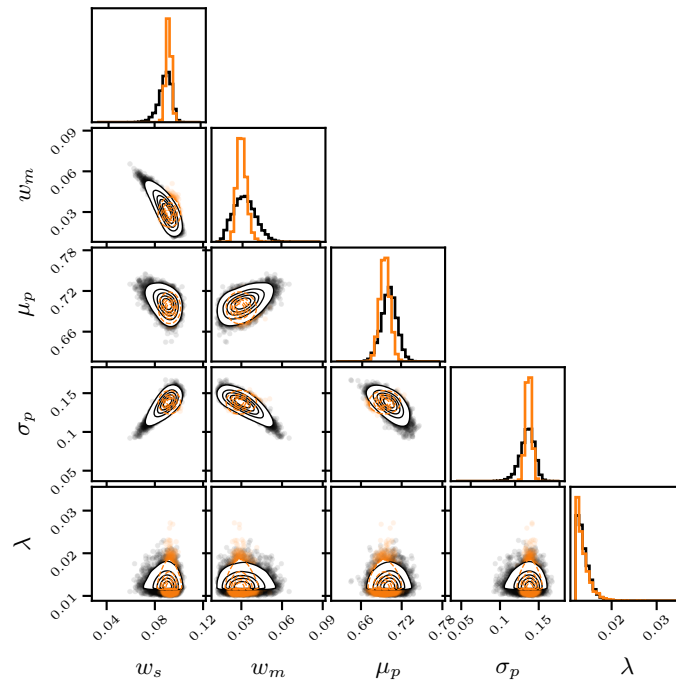
(a) VSBQ



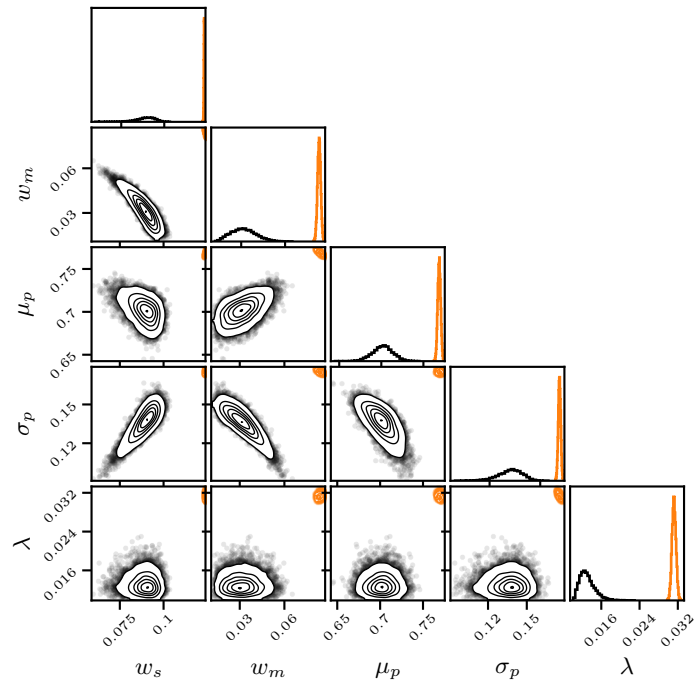
(b) NNR



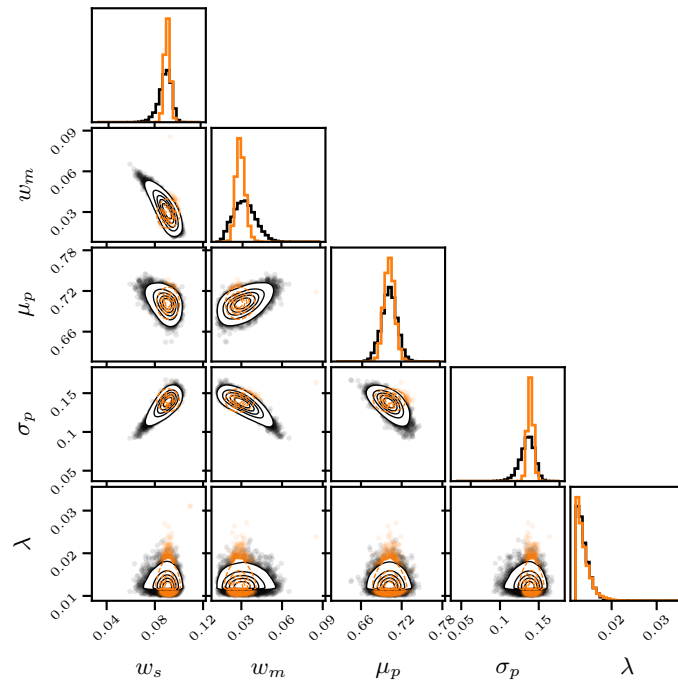
(c) LAPLACE



(d) BBVI, Gaussian (diagonal)



(e) BBVI, Gaussian (full-rank)



(f) BBVI, MoG ($K = 5$)

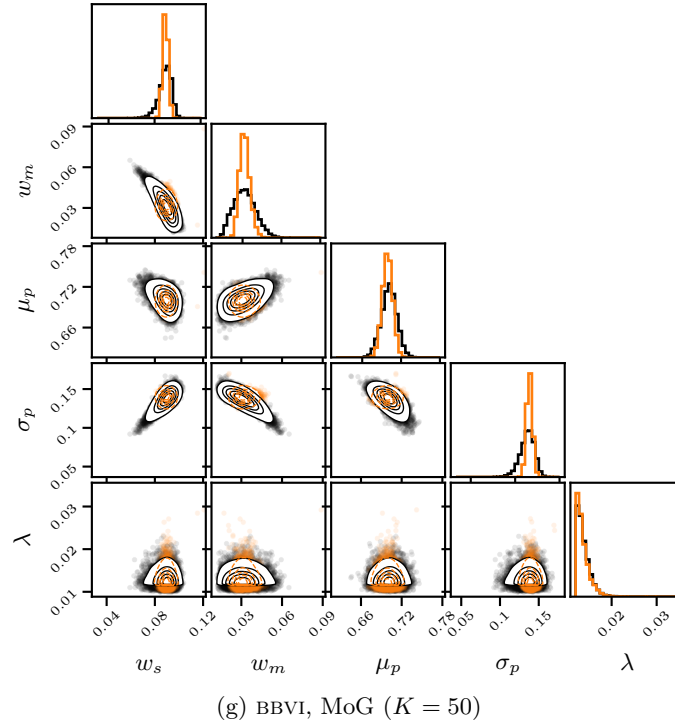
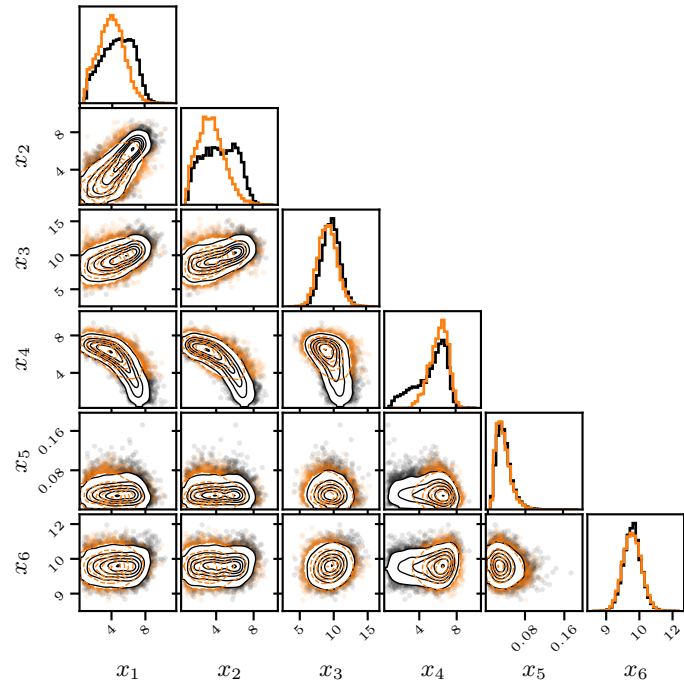
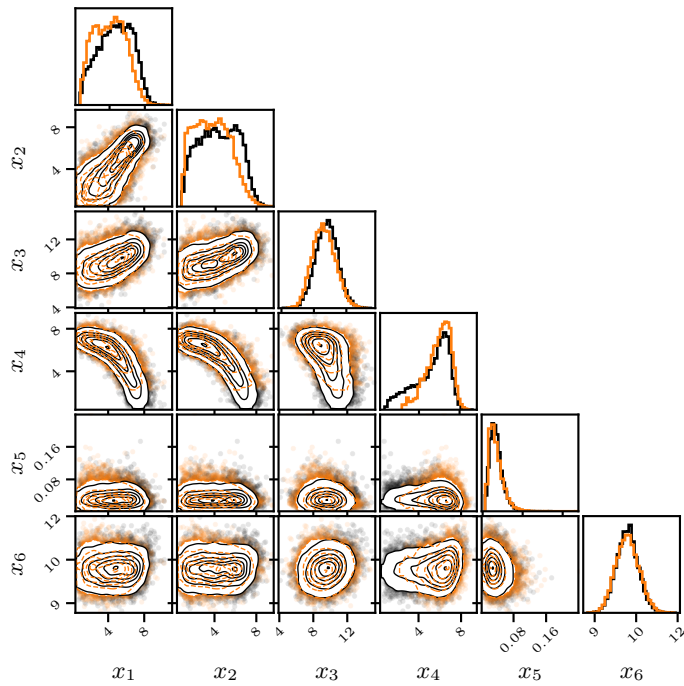


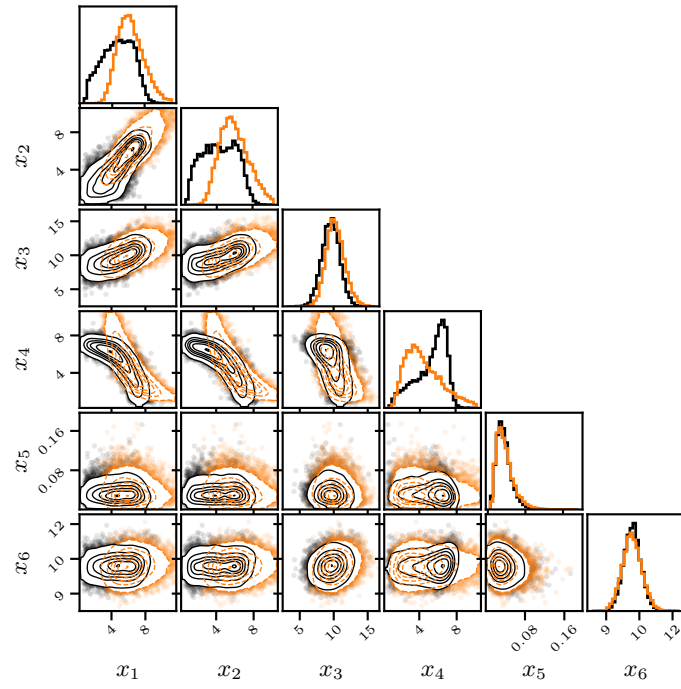
Figure S7: **Bayesian timing model posterior visualization.** $\sigma_{\text{obs}} = 3$ for VSBQ and NNR, $\sigma_{\text{obs}} = 0$ for LAPLACE. The orange density contours and points in the sub-figures represent the posterior samples from VSBQ, NNR, and LAPLACE, while the black contours and points denote ground truth samples. Both VSBQ and NNR capture the shape of the posterior in the presence of observation noise. LAPLACE obtains a reasonable approximation, for the noiseless case. Among the BBVI methods, the Gaussian (diagonal), MoG ($K=5$), and MoG ($K=50$) configurations produce visually similar results and underperform compared to VSBQ and NNR.



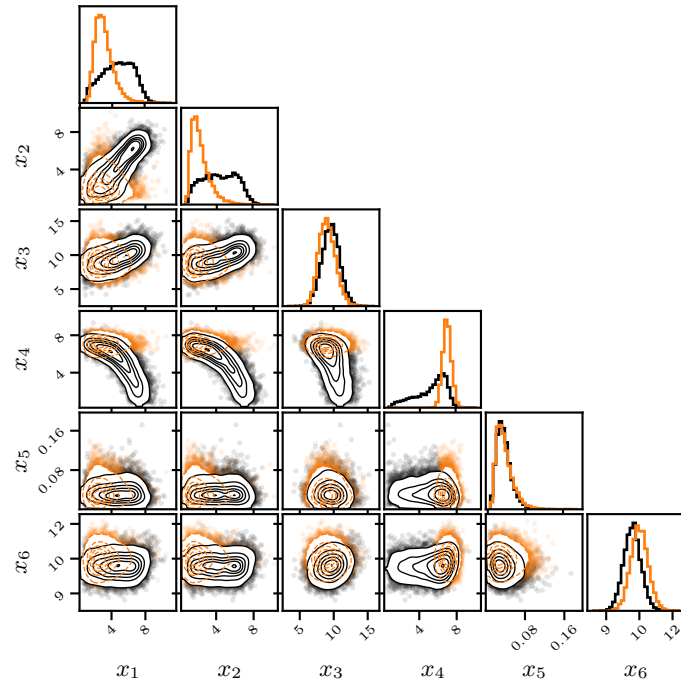
(a) VSBQ



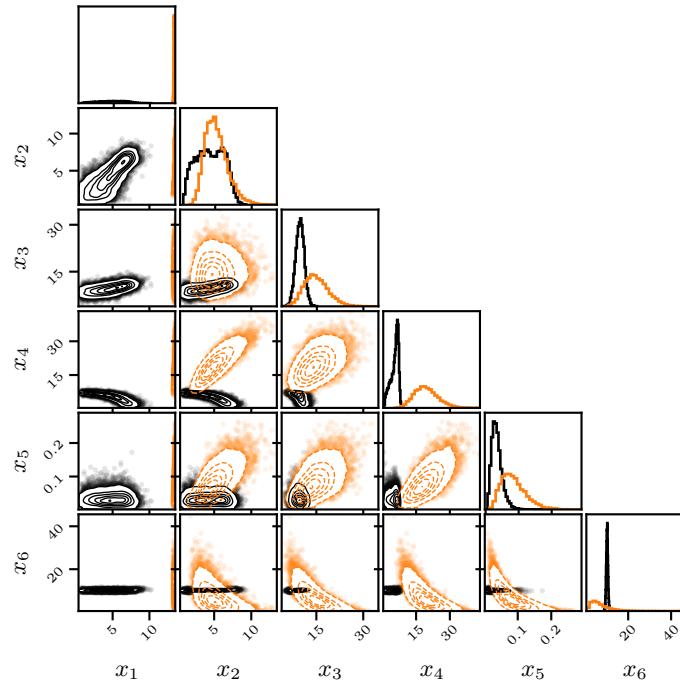
(b) NNR



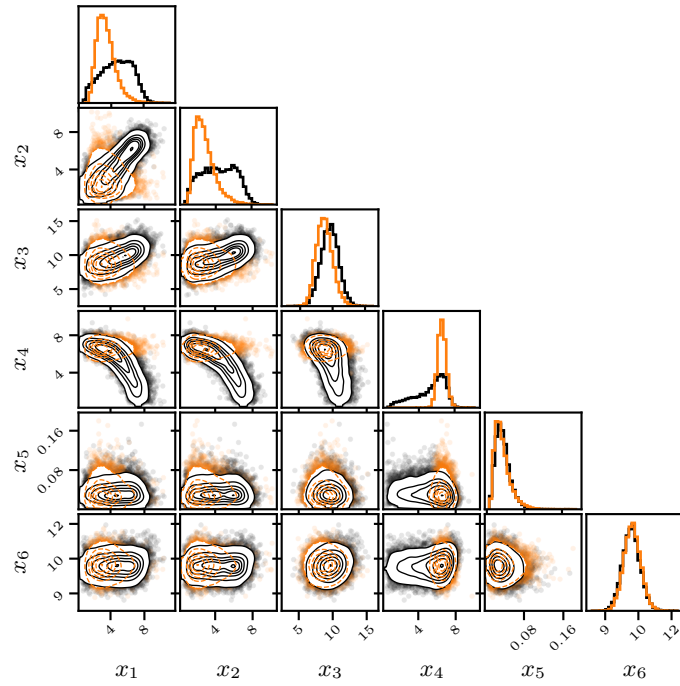
(c) LAPLACE



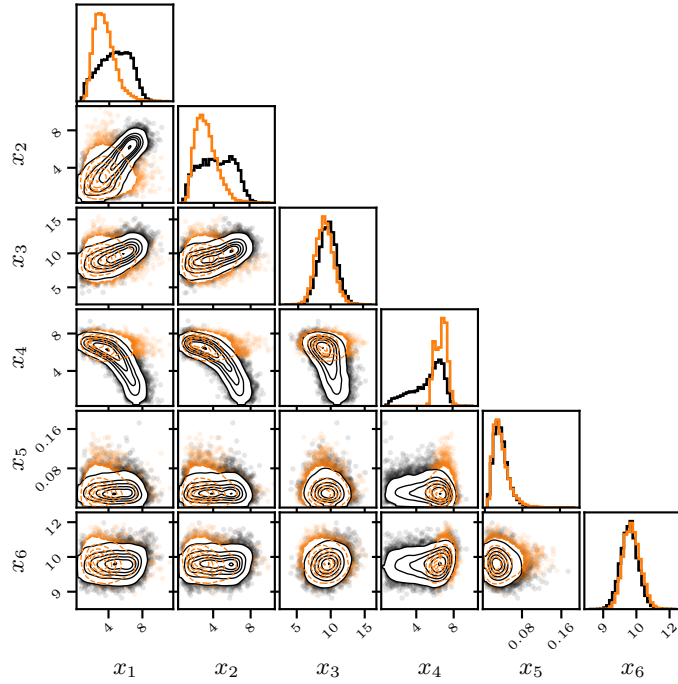
(d) BBVI, Gaussian (diagonal)



(e) BBVI, Gaussian (full-rank)



(f) BBVI, MoG ($K = 5$)



(g) BBVI, MoG ($K = 50$)

Figure S8: **Multisensory causal inference model posterior visualization.** $\sigma_{\text{obs}} = 3$ for VSBQ and NNR, $\sigma_{\text{obs}} = 0$ for LAPLACE. The orange density contours and points in the sub-figures represent the posterior samples from VSBQ, NNR, and LAPLACE, while the black contours and points denote ground truth samples. $(x_1, x_2, x_3, x_4, x_5, x_6) = (\sigma_{\text{vis}}(c_{\text{low}}), \sigma_{\text{vis}}(c_{\text{med}}), \sigma_{\text{vis}}(c_{\text{high}}), \sigma_{\text{vest}}, \lambda, \kappa)$. Both VSBQ and NNR obtain a reasonable approximation of the complex posterior under noisy evaluations, with NNR yielding a more faithful approximation for this random seed. LAPLACE fails to capture the posterior well, despite it being noiseless. Among the BBVI methods, the Gaussian (diagonal), MoG ($K=5$), and MoG ($K=50$) configurations produce visually similar results and underperform compared to VSBQ and NNR.

C.7 Runtime analysis

In this section, we present an analysis of the runtime for our method and baselines. Such an analysis is important for a post-process inference method, which ideally should only take a relatively short time (*e.g.*, a few minutes).³ For VSBQ and NNR, we report the wall-clock runtime based on 5 independent runs with different training data sets (*i.e.*, traces from the MAP optimizations). For LAPLACE, the runtime is based on 5 runs for numerically estimating the Hessian matrix. We measure the runtime on both CPU and GPU platforms.⁴ Specifically, we utilize an AMD EPYC 7452 32-core Processor for CPU computations and an NVIDIA A100 for GPU computations.

The dominating algorithm overhead for VSBQ is the sparse GP fitting, whose efficiency depends on the number of data points and inducing points. In general, we recommend utilizing as many inducing points as resources permit to achieve improved approximation accuracy. The variational inference part of VSBQ is fast due to the (sparse) Bayesian quadrature. For NNR, the runtime heavily depends on the size of the network and the effort spent on hyperparameter search (*e.g.*, the weight decay). A larger network increases the representation flexibility but also introduces more computational overhead and potentially a higher risk of overfitting. Extensive hyperparameter search generally enhances regression performance but increases computational demand. The runtime for LAPLACE depends on the computational cost associated with evaluating the log-likelihood function when computing the Hessian matrix.

Table S4: **Algorithm runtime.** The wall-clock runtime for VSBQ and NNR is measured on both the CPU and GPU, whereas for LAPLACE, only the CPU runtime for numerically computing the Hessian matrix is reported.

Benchmark Task	Algorithm	CPU Runtime (s)	GPU Runtime (s)
Two moons	VSBQ	164 ± 6	110 ± 5
	NNR	1935 ± 148	168 ± 19
	LAPLACE	< 1	N/A
Multivariate Rosenbrock-Gaussian	VSBQ	1863 ± 499	254 ± 4
	NNR	18155 ± 1740	638 ± 161
	LAPLACE	< 1	N/A
Bayesian timing model	VSBQ	538 ± 66	198 ± 4
	NNR	12287 ± 2471	451 ± 147
	LAPLACE	38 ± 0	N/A
Multisensory causal inference	VSBQ	1167 ± 178	260 ± 3
	NNR	13745 ± 2103	547 ± 88
	LAPLACE	2 ± 0	N/A

As shown in Table S4, VSBQ takes several minutes on a CPU and benefits strongly from GPU acceleration, bringing post-process inference times down to 1-5 minutes. NNR is slower compared

³BBVI methods are not considered post-processing inference techniques and serve only as a reference baseline for posterior approximation accuracy. Their runtime primarily depends on the total number of target function evaluations and the grid search for tuning learning rates.

⁴It is worth noting that, in the case of GPU runtime measurement, only the sparse GP and neural network fitting were carried out with a GPU. Due to our current implementation, the stochastic variational inference optimization part for VSBQ and NNR was always conducted using the CPU. Future efforts to port the stochastic variational inference procedure completely to GPU could further enhance the computational performance of both methods.

to VSBQ in the benchmark problems and also greatly benefits from GPU computation. In scenarios where the log-likelihood function is cheap to evaluate, LAPLACE proves to be efficient and straightforward. Its additional requirement is that the target MAP point during optimization runs lies within the unbounded parameter space. Moreover, we recall that the Laplace approximation is not easily obtainable if only noisy likelihood evaluations are available.

Overall, VSBQ remains efficient across the benchmark problems. The wall-clock runtime efficiency makes it well-suited as a fast post-processing algorithm to compute the approximate posterior directly from the existing target posterior evaluations.

C.8 Posterior estimation: MCMC or variational inference?

After having fitted a surrogate regression model (a sparse GP or a neural network) to the log-density function, the key issue is how to obtain an estimate of the posterior density (see Figure 1 in the main text). In the paper, we demonstrated how (stochastic) variational inference (SVI) on the surrogate can successfully recover the posterior, based on prior work [Acerbi, 2018].⁵ However, why not directly run MCMC on the log-density surrogate to obtain approximate posterior samples, as done by other works [Rasmussen, 2003, Nemeth and Sherlock, 2018, Järvenpää et al., 2021]?

The answer is that we attempted to use MCMC (slice sampling; Neal, 2003) and empirically found that, for both sparse GPs and neural networks, MCMC often gives inferior results compared to SVI. For example, Table S5 shows the performance metrics for SGPR with SVI (*i.e.*, VSBQ), SGPR with MCMC, NNR with SVI, and NNR with MCMC, on the Bayesian timing model benchmark problem. MCMC is substantially less robust and yields worse results than SVI.

Table S5: **Comparison between MCMC and SVI (Bayesian timing model, $\sigma_{\text{obs}} = 3$).** For both VSBQ and NNR, MCMC performs poorly while SVI performs well in terms of metrics. For MCMC, the marginal likelihood estimate is not directly available.

	ΔLML (\downarrow)	MMTV (\downarrow)	GsKL (\downarrow)
SGPR (SVI)	0.21 [0.18,0.22]	0.044 [0.039,0.049]	0.0065 [0.0059,0.0084]
SGPR (MCMC)	N/A	0.69 [0.057,0.92]	5.2e+03 [0.088,5.8e+11]
NNR (SVI)	0.30 [0.039,0.44]	0.086 [0.049,0.12]	0.017 [0.013,0.076]
NNR (MCMC)	N/A	0.81 [0.75,0.89]	2.4e+11 [2.1e+03,1.2e+14]

We hypothesize that the reason why both the sparse GP and neural network surrogates can perform poorly with MCMC is that, given the limited set of log-density observations, the surrogate model only approximates the log-density function well in a local region. Outside of this local “trust region”, the surrogate may end up hallucinating [De Souza et al., 2022]. Therefore, it is important to be careful not to leave the regions that contain actual observations. Without additional constraints, an MCMC sampler can escape into the hallucinated regions and return meaningless samples. In support of our hypothesis, Figure S9 shows a representative failure case where the samples from MCMC are far from the log-density observations.

Instead, for variational inference, initializing the variational distribution components around the high-density observation points and imposing an additional penalty loss in the ELBO optimization for bounding the variational parameters (means and scales of the mixture components), help constrain the variational distribution in the local trust region, see Section C.1 for details. As a further

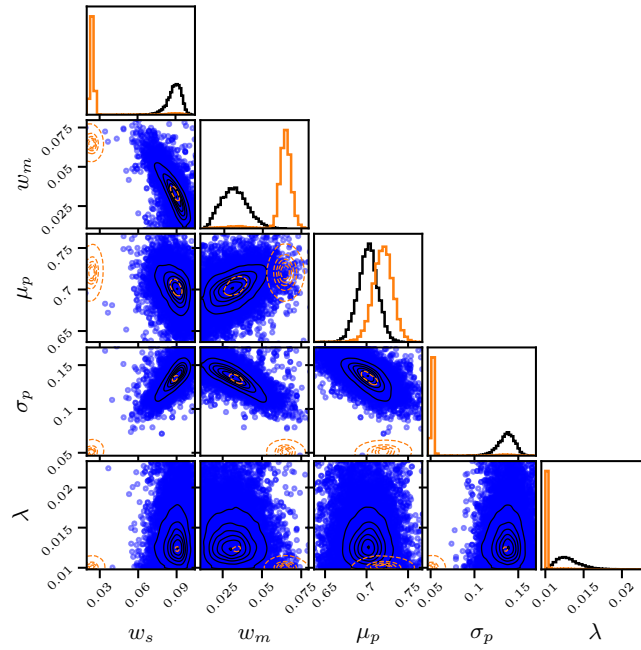
⁵In this paper, SVI refers to stochastic variational inference with the reparameterization trick, including ADVI.

advantage, for a sparse GP, variational inference with Bayesian quadrature is efficient and affords computation of the ELBO and its standard deviation, ELBO_{sd} , for assessing its uncertainty.

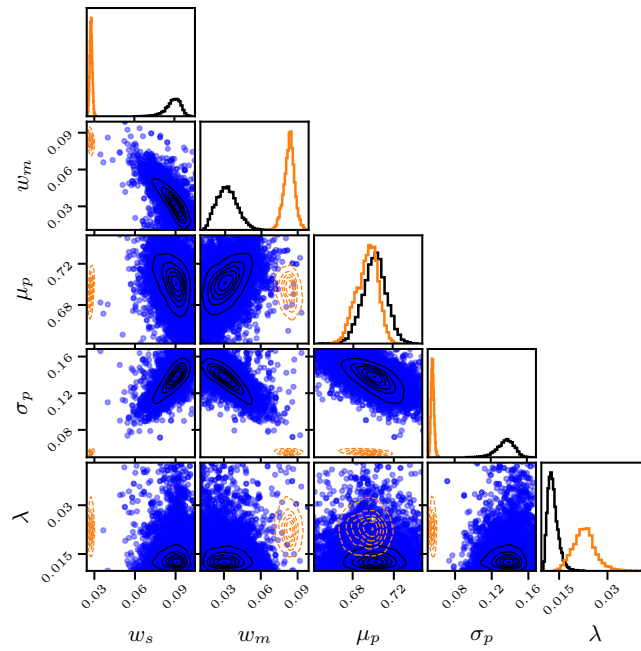
C.9 Note on package versions

We implemented vSBQ in Python, using JAX 0.4.20 [Bradbury et al., 2018] and NNR using PyTorch 2.1.1 [Paszke et al., 2019]. We used the following package versions for all experiments in this paper:

- pycma 3.3.0 (<https://github.com/CMA-ES/pycma/releases/tag/r3.3.0>) for the CMA-ES optimization algorithm;
- PyBADs 1.0.3 (<https://github.com/acerbilab/pybads/releases/tag/v1.0.3>) for the BADs optimization algorithm;
- emcee 3.1.4 (<https://github.com/dfm/emcee/releases/tag/v3.1.4>) for generating the ground-truth posterior samples.



(a) SGPR (MCMC)



(b) NNR (MCMC)

Figure S9: **A typical failure with MCMC.** The benchmark problem is the Bayesian timing model ($\sigma_{\text{obs}} = 3$). The orange density contours in the sub-figures represent the posterior samples from SGPR (MCMC) and NNR (MCMC), while the black contours and points denote ground truth samples. The blue points are (the projection of) training points collected from the MAP optimization runs. In both shown cases, the MCMC samples ‘escaped’ to a region far from the training points, where the surrogate cannot be trusted.